Analysis of thin-film photonic crystal microstructures

Pottage, John Mark

Award date:
2003

Awarding institution:
University of Bath

ANALYSIS OF THIN-FILM PHOTONIC CRYSTAL MICROSTRUCTURES

Submitted by John Mark Pottage
for the degree of
Doctor of Philosophy
of the University of Bath
2003

ProQuest LLC
789 East Eisenhower Parkway
P.O. Box 1346
Ann Arbor, MI 48106-1346

Abstract

Optical-scale microstructures containing thin-film photonic crystals (TFPCs) are modelled by transfer/scattering matrix methods, based on Fourier-series expansion of the optical Bloch eigenmodes. The majority of the TFPCs considered consist of 2D arrays of holes arranged in a triangular lattice, etched into high-index $Al_xGa_{1-x}As$ and placed on a low-index oxidised substrate. These TFPCs can be easily fabricated by standard electron-beam lithography techniques. Unlike most photonic crystal devices that have been proposed, our 'intra-pass-band' TFPCs would work by exploiting the somewhat surprising properties of propagating optical Bloch waves rather than directly relying on photonic bandgaps. By numerical modelling, it is demonstrated that 2D-patterned TFPCs can support highly dispersive high-Q quasi-guided and truly-guided resonant modes, and the unusual properties of these modes are explained in terms of their Bloch-wave compositions. Modal dispersion diagrams of TFPCs, showing the loci of the resonant modes in in-plane wavevector space at fixed frequency, are calculated. These so-called 'resonance diagrams', and variants thereof, are shown to be a useful design tool for TFPC-based integrated optical components. It is suggested that TFPCs may be a viable alternative to distributed Bragg reflectors in semiconductor vertical cavity surface-emitting lasers, possessing potential advantages in terms of compactness and ease of fabrication. The high angular and spectral dispersion of the resonant modes implies that TFPCs could form the basis of a new family of compact devices for performing such functions as wavelength-division multiplexing/demultiplexing, beam-steering and frequency-selective filtering. Enhancement of nonlinear effects could also be achieved in TFPC resonators, because in them a high cavity Q-factor and a low in-plane group-velocity can be attained simultaneously.

Acknowledgements

The assistance of the following people in the undertaking of the work presented in this thesis is gratefully acknowledged:

P.St.J. Russell, my supervisor, for guidance, constant support and encouragement, and for the 'two-wave resonator' model in Chapter 3.

E. Silvestre (Valencia) for the approximation enabling the Fourier integrals appearing in Chapter 2 to be transformed from 2D to 1D, and for calculating Figure 5.1.

D.S. Mogilevtsev (Belarus Academy of Sciences) and *P. John Roberts* (Blaze Photonics, ex DERA Malvern) for useful discussions about transfer/scattering matrices.

R.M. de Ridder and R. Stoffer (MESA Research Institute, The Netherlands) for Figure 6.3(a), and for an interesting and enjoyable fortnight in the Lightwave Devices Group.

T. Krauss, R. de la Rue, C. Smith (Glasgow), *M. Charlton, G. Parker* (Southampton), and *S.R. Andrews* (Bath) for advice on practical TFPC parameters, and also *L. Frohly* (Glasgow) for suggestions concerning quantum dot embedding.

V.V. Ravi Kanth Kumar, for invaluable advice prior to thesis-submission.

Last but by no means least I acknowledge the help of my parents Frederick and Elaine, my grandmother Lily, my brother James, and Drs. Bruning and Moss throughout my long illness. Besides these, I would like to thank the 'coffee gang' and all other members of the Optoelectronics Group, together with Federica Causa, Jitendra Kumar Kar, and Cornelia Wiebels, for companionship during the seemingly endless process of 'writing-up'. I also thank my previous landlord, Medhat Omran, for providing a welcoming house to which to return during the critical stages, and Stuart Brand of the Condensed Matter Theory Group in Durham, for introducing me to photonic crystals.

Notes

Units

The system of units used throughout is such that $c = 1,\ \mu_o = 1,\ \epsilon_o = 1$.

Acronyms

Some of the acronyms used in this thesis are summarised below:

- TFPC: thin-film photonic crystal
- PCF: photonic crystal fibre
- VCSEL: vertical-cavity surface-emitting laser
- MLP-TFPC: merely locally-periodic thin-film photonic crystal
- DBR: distributed Bragg reflector
- WDM: wavelength division multiplexing
- VFFD: vector-field Fourier-decomposition

Publications in Peer-Reviewed Journals

See [1, 2, 3].

Contributions to Conference Proceedings

See [4, 5, 6, 7, 8].

Contents

Chapter 1

Introduction

It is a well-known fact that photonic crystals [9] are capable of suppressing the propagation of light within certain frequency intervals or 'band-gaps'. Photonic band-gap crystals have been investigated by many researchers because they are intrinsically interesting in terms of fundamental physics and have numerous potential applications. In addition to this, a substantial number of groups are now beginning to realise that the properties of propagating modes near the edge of a bandgap (i.e. within a passband) can be as useful as modal suppression within a bandgap. In this thesis, we analyse intra-passband resonant light propagation at near-infrared frequencies in thin-film photonic crystals and we encounter and investigate several noteworthy effects. We have chosen this type of photonic crystal because it can be fabricated easily on micrometric length-scales, unlike its 3D-microstructured counterpart. The work presented here is based entirely on numerical simulation, with constant regard to the practical limits of fabrication technology, guided by collaboration with several experimental groups (which are listed in the Acknowledgements).

1.1 A review of Bloch wave optics

References [10] and [11] together provide a good introduction to Bloch wave optics. In this section, we cover only the essentials necessary for understanding the subsequent chapters. An optical Bloch wave is an electromagnetic mode of a microstructured dielectric material in which the refractive index is a wavelength-scale periodic function of position. Such microstructured materials are known as photonic crystals. Photonic crystals occur in nature: certain fish scales [12], butterfly wings [13, 14], and sea mouse spines [15] are coated with natural thin-film photonic crystals, to which their properties

of iridescence and highly angle-selective reflectance are attributable. They can also be made artificially by processes such as reactive ion etching. The unusual optical properties of photonic crystals can be described in terms of photonic dispersion surfaces as follows.

1.1.1 Photonic dispersion surfaces

A photonic dispersion surface $\omega(\underline{k})$ is, strictly speaking, the locus of all allowed modes in the four-dimensional space $(\omega, \underline{k})$, where ω is the optical angular frequency and $\underline{k}$ is the wavevector. The photonic dispersion surface of an 'ordinary' dielectric material of refractive index n is a hypercone described by the equation $n^2\omega^2 = c^2(k_x^2 + k_y^2 + k_z^2)$. A three-dimensional 'cross-sectional slice' through this hypercone at constant angular frequency ω is a sphere in wavevector space. A photonic crystal can have a photonic dispersion surface that is very different to the familiar hypercone. In fact, there will generally be more than one dispersion surface, necessitating the subscript j to distinguish them, and these dispersion surfaces $\omega_j(\underline{k})$ can be split, buckled, stretched, punctured, and squashed by altering the physical microstructure of the photonic crystal. Because photonic crystals can manipulate photonic dispersion to such an extreme extent, they are capable of controlling almost all aspects of light propagation.

Every point on the dispersion surfaces $\omega_j(\underline{k})$ must correspond to a 'photonic Bloch wave,' because that is the only type of electromagnetic wave that can survive inside a photonic crystal, in the 'steady state'. A photonic Bloch wave can be defined to be such that its vector wave-field has the same periodicity as the lattice of the crystal in which it exists, after division by the phase factor $\exp(i\underline{k} \cdot \underline{r})$, where $\underline{k}$ is the fundamental wavevector. Actually, even a transient wave can be constructed from Bloch modes, provided that we use a linear combination having a continuous distribution of optical frequencies, because the set of all Bloch modes is a so-called 'complete set,' and can therefore be used to expand any field function.

Photonic Bloch waves are named after their electronic analogue in solid-state physics, from which the field of photonic crystals borrows most of its terminology. However, the analogy between photonic crystals and semiconductor crystals cannot be stretched very far: the wavefunction of light is a vector rather than a scalar, as in the case of a non-relativistic electron. Also, photons in photonic crystals made from linear materials do not interact, whilst electrons in semiconductors do.

1.1.2 The infinitesimal coupling model

Consider a dielectric material that is translationally invariant along axes y and z and has a periodic variation in its electric permittivity ϵ along the x-axis with period Λ. In this case, ϵ can be expanded as a Fourier series as follows:

$$\epsilon = \sum_{m=-\infty}^{+\infty} \epsilon_m \exp(iG_m x) \tag{1.1}$$

where $G_m = 2\pi m/\Lambda$, which is the magnitude of the so-called 'grating vector.' The well-known Bloch theorem states, in this case, that fields inside the periodic material must be expandable as a linear superposition of electromagnetic plane waves that have wavevector components along the x-axis of the form $k_x + G_m$. Let $\underline{K}$ be the 3D wavevector of these constituent plane waves in general, then $(K_x, K_y, K_z) = (k_x + G_m, k_y, k_z)$. Since the variation in ϵ is only along the x-axis, the grating vector has no components along the y and z axes. Let us focus on the limiting case in which the modulation depth of ϵ is infinitesimally small compared with the background value ϵ_v. An ordinary plane wave solution of the form $f = f_m \exp(i(k_x x + k_y y + k_z z - \omega t))$, where f is any particular nonzero field vector component, must still be valid in this case, since ϵ is almost unmodulated. This plane wave has the familiar dispersion equation $\epsilon\omega^2 = k_x^2 + k_y^2 + k_z^2$, when working in units in which $c = 1, \epsilon_o = 1$, and $\mu_o = 1$. However, the Bloch theorem must also be valid because ϵ is nevertheless periodically modulated. Therefore, the dispersion equation of the material must be $\epsilon_v\omega^2 = K_x^2 + K_y^2 + K_z^2$, where $\underline{K}$ was defined above. This dispersion equation describes a series of spheres populating the entire K_x axis (because the index m in the grating vector can be any integer), with the centres of any pair of adjacent spheres separated by a distance G_1. Although the dispersion surfaces are spherical (each with radius $\omega\sqrt{\epsilon}$), they can be represented on paper by plotting $K_r = \sqrt{K_y^2 + K_z^2}$ (which is the radial coordinate in a plane perpendicular to the K_x axis) against K_x at constant frequency ω. The dispersion surfaces are shown in this way in Figure 1.1. The scalar wave equation for a wave associated with any one of these dispersion surfaces can be written as $\epsilon_v\omega^2 h_m = \left(K_x^2 + K_y^2 + K_z^2\right) h_m$ where h_m is any Fourier coefficient of the magnetic field of the scalar wave. Let us take, as an example, waves associated with a pair of immediately adjacent dispersion spheres. We will choose, arbitrarily, the sphere centred on the origin of wavevector space and also the sphere centred on $K_x = -G_1$. The scalar wave equations for waves associated with these dispersion surfaces will be

$$\epsilon_v\omega^2 h_0 = (k_x^2 + k_y^2 + k_z^2)h_0 \tag{1.2}$$

$$\epsilon_v\omega^2 h_1 = ((k_x + G_1)^2 + k_y^2 + k_z^2)h_1 \tag{1.3}$$

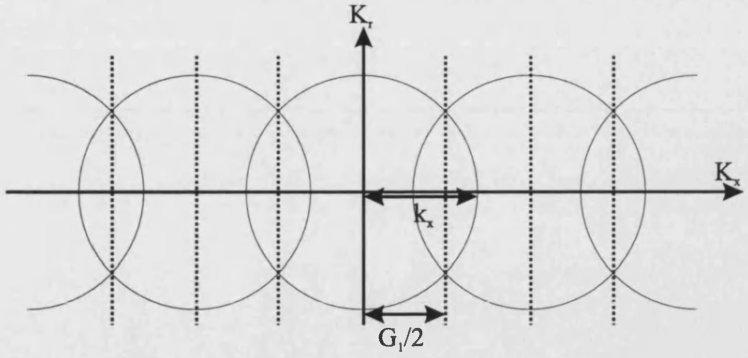

Figure 1.1: The dispersion surfaces of a 1D crystal in the case of infinitesimally small modulation depth.

These two equations can be written as a single matrix equation as follows:

$$\begin{bmatrix} \epsilon\omega^2 - k_x^2 - k_y^2 & 0 \\ 0 & \epsilon\omega^2 - (k_x + G_1)^2 - k_y^2 \end{bmatrix} \begin{bmatrix} h_0 \\ h_1 \end{bmatrix} = k_x^2 \begin{bmatrix} h_0 \\ h_1 \end{bmatrix} \tag{1.4}$$

This alternative form may seem rather pointless, since the two waves are clearly decoupled from each other, because the off-diagonal elements of the matrix are zero-valued. However, as we shall see in the next section, these off-diagonal elements become nonzero when the modulation depth of ϵ is increased sufficiently so that it is small but not infinitesimally small.

1.1.3 The weak coupling model

Let ϵ be cosinusoidally modulated as follows:

$$\epsilon = \left(\frac{\epsilon_b + \epsilon_a}{2}\right) + \left(\frac{\epsilon_b - \epsilon_a}{2}\right)\cos(G_1 x) \tag{1.5}$$

where the modulation depth of ϵ, which is equal to $\epsilon_b - \epsilon_a$, is small compared to its average value $\epsilon_v = (\epsilon_b + \epsilon_a)/2$, but not infinitesimally so. The solution of Maxwell's equations in this case, using the techniques described in chapter 2, reveals that, to a first order approximation, the off-diagonal elements in equation 1.4 become equal to $(\epsilon_b - \epsilon_a)\omega^2/4$. The equation to be solved in this case is therefore

$$\begin{bmatrix} \epsilon_v\omega^2 - k_x^2 - k_y^2 & \left(\frac{(\epsilon_b - \epsilon_a)}{4}\right)\omega^2 \\ \left(\frac{(\epsilon_b - \epsilon_a)}{4}\right)\omega^2 & \epsilon_v\omega^2 - (k_x + G_1)^2 - k_y^2 \end{bmatrix} \begin{bmatrix} h_0 \\ h_1 \end{bmatrix} = k_x^2 \begin{bmatrix} h_0 \\ h_1 \end{bmatrix} \tag{1.6}$$

The solutions to this matrix eigensystem are Bloch modes. The off-diagonal terms in the matrix couple together the two plane-waves on the neighbouring dispersion surfaces,

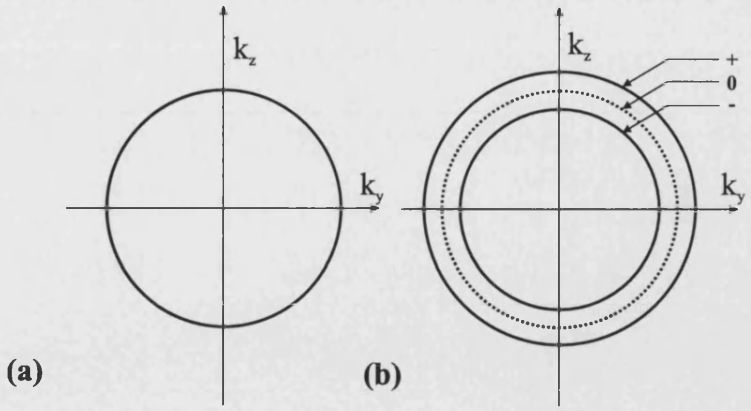

Figure 1.2: The circle of intersection in the case of infinitesimally small modulation depth is shown in (a). When the modulation depth is increased, the degeneracy is broken to give two distinct solutions that correspond to the two circles in (b), in which the splitting effect has been exaggerated. The dotted circle in (b) is a copy of diagram (a).

so that they can no longer propagate independently but must instead co-operate to form a Bloch wave. This is the simplest possible model for the simplest possible photonic crystal, yet it captures the essence of the physics behind optical Bloch waves. For example, let us set the frequency ω so that the two neighbouring spheres intersect and then examine the solution of equation 1.6 in the plane of intersection of the spheres, which will be the plane $K_x = -G_1/2$. Solving the eigensystem (equation 1.6) via its corresponding determinantal equation, and setting $K_x = -G_1/2$ gives the following solutions:

$$\omega^2(\epsilon_v \pm \epsilon_d) - \left(\frac{1}{2}G_1\right)^2 = k_y^2 + k_z^2 \tag{1.7}$$

where $\epsilon_v = (\epsilon_b + \epsilon_a)/2$ and $\epsilon_d = (\epsilon_b - \epsilon_a)/4$. These two solutions describe two circles of different radii in the plane of intersection, and they show that the weak periodic modulation of ϵ breaks the degeneracy between the two dispersion surfaces and splits them apart. This effect, of course, only occurs when the frequency (which controls the radii of the dispersion spheres) is sufficiently high for neighbouring surfaces to intersect, i.e. when $\omega\sqrt{\epsilon_v} \geq (G_1/2)$. Figure 1.2 illustrates this, which is an example of the mutual repulsion of dispersion surfaces at a Brillouin zone boundary- a frequently occurring phenomenon in photonic crystals. Typical dispersion surfaces in the weak-coupling case, plotted in the same way as in Figure 1.1, are shown in Figure 1.3, where the band-splitting effect at the Brillouin zone boundaries has been exaggerated for clarity. The dispersion surfaces in Figure 1.3 consist of an infinite number of lenticuloids centred on the K_x axis, enclosed within a hollow tube of periodically modulated radius. Planes such as $K_x = -G_1/2$ are known as 'Brillouin zone boundaries' (see Chapter 2), and the dispersion surface splitting effect is most pronounced in the immediate vicinity of these planes. This figure is perhaps the simplest non-trivial example of a 'wavevector

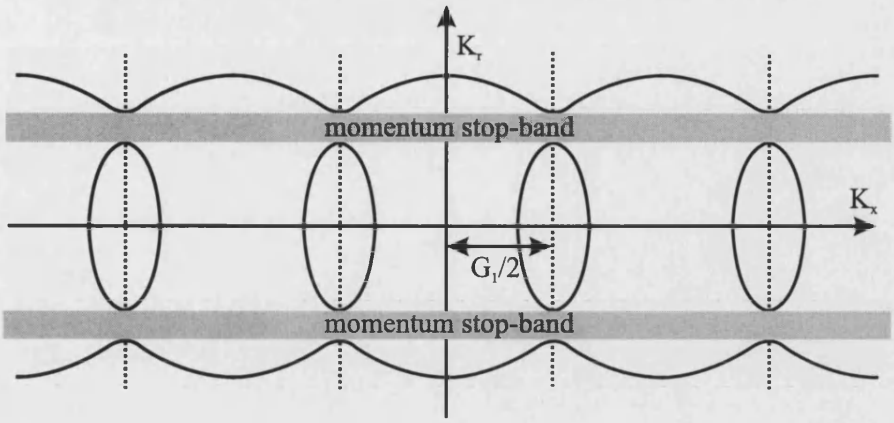

Figure 1.3: A typical set of dispersion surfaces for a 1D crystal having a refractive index profile that is weakly cosinusoidally modulated along the x axis (band-splitting effect exaggerated, as in Figure 1.2).

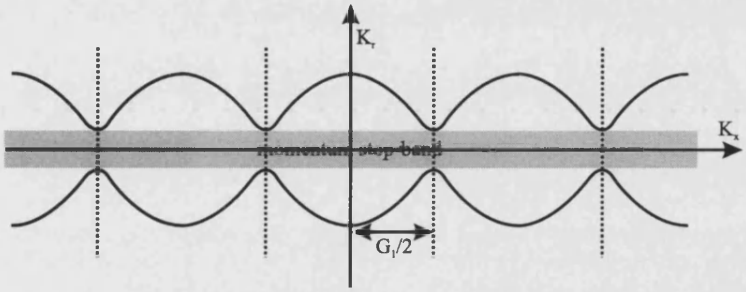

Figure 1.4: The lenticuloids can be made to vanish by adjusting the frequency, creating a stop-band for light directed parallel to the grating axis (x).

diagram' of a photonic crystal.

Whilst Figure 1.3 exhibits stop-bands in wavevector space (which are the shaded regions), stop-bands are also formed in (ω, K_x) space. As an example, consider the case in which the frequency is critically adjusted such that the neighbouring spheroids only just interact, making the lenticuloids vanish, as in Figure 1.4. In this case, a stop-band is opened-up around $K_r = 0$. However, detuning the frequency either positively or negatively by more than a certain amount will make the lenticuloids re-appear. Therefore, this periodic material has a frequency stop-band for $K_r = 0$, as shown schematically in Figure 1.5. Frequency stop-bands can also be found for all other values of K_r between its upper and lower limits of $\pm\omega\sqrt{\epsilon_b + \epsilon_a}$, but the $K_r = 0$ case provides the clearest illustration.

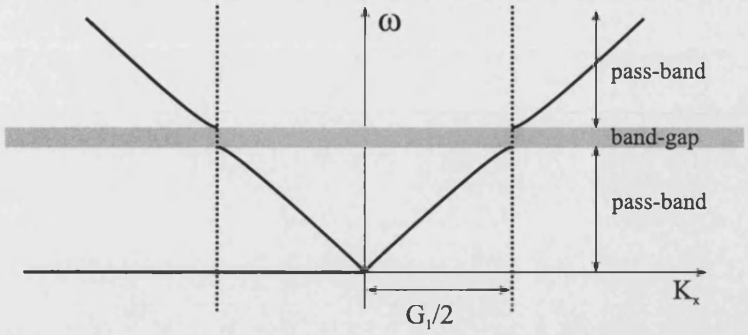

Figure 1.5: A frequency stop-band in the case of a weakly modulated grating, which exists when K_r is fixed at zero. At frequencies above and below the upper and lower edges of the stop-band (respectively), the lenticuloids re-appear, giving pass-bands.

1.1.4 Wavevector diagrams

Wavevector diagrams plotted at fixed optical frequency (such as Figure 1.3) can be used to obtain an intuitive undertanding of the operation of photonic crystal devices in general. As an introductory example, we will take a weakly cosinusoidally modulated crystal of refractive index $n_2(x)$ and suppose that it is in contact with an unpatterned medium of refractive index n_1, such that the interface between the two media is perpendicular to the x axis, as shown in Figure 1.6(a). Both media will be assumed to be semi-infinite, and we will set $K_y = 0$ so that $K_r = K_z$, for simplicity. A possible wavevector diagram for the unpatterned medium (at a particular fixed operational optical frequency ω) is given in Figure 1.6(b). This is simply a sphere of radius $n_1\omega$. A typical wavevector diagram for the crystal is shown in Figure 1.6(c), which is a copy of Figure 1.3. Conservation of photon momentum $\underline{p} = \hbar\underline{k}$ will apply to the components parallel to the interface, so in this case K_z will be conserved by light passing through the interface. Therefore, the only parts of the dispersion surfaces that may be excited by light incident from the unpatterned medium are those that intersect, for example, the dashed construction line running between Figures 1.6(b) and 1.6(c), along which K_z is constant. In Figure 1.6, the double-headed arrows indicate the group velocity directions of the excited rays, which are locally normal to the curves on the wavevector diagrams, and which point in the direction of increasing frequency, since the group velocity $\underline{v_g} = \partial\omega/\partial\underline{k}$ is the gradient in wavevector space of the frequency whilst being constrained to follow a dispersion surface. Note that a maximum of two waves may be excited at fixed K_z in the unpatterned medium, whilst many waves can be excited in the patterned medium (which are, however, the components of only two Bloch modes), unless K_z is within a momentum stop-band, in which case no propagating waves can be excited in the photonic crystal, so all of the light incident from the unpatterned medium will be reflected.

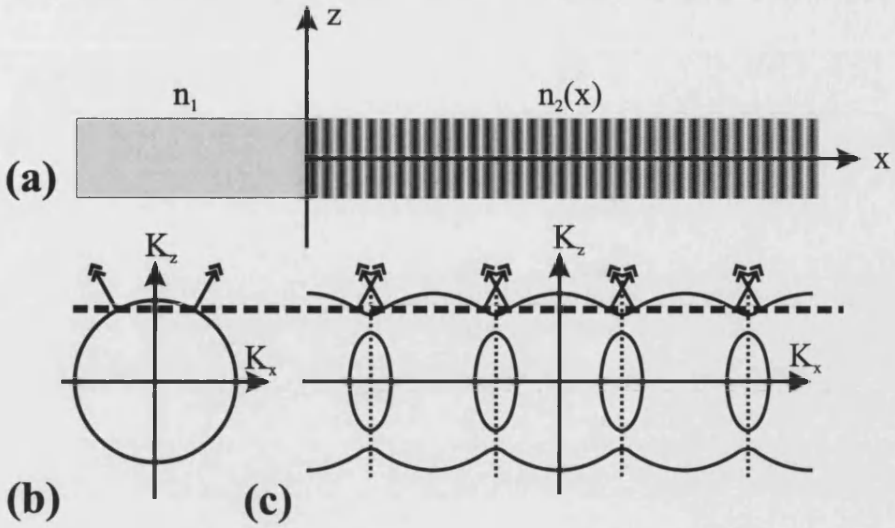

Figure 1.6: Illumination of a semi-infinite weakly-modulated photonic crystal from an unpatterned medium, where the interface between the two media is perpendicular to the grating axis. A diagram of the situation is shown in (a), whilst (b) and (c) are example wavevector diagrams for the unpatterned medium and the crystal respectively. Note that the origins of plots (b) and (c) coincide.

If the interface is now chosen to be parallel to the x axis, as shown in Figure 1.7(a), the wavevector diagrams of the two media must be aligned vertically rather than horizontally (see Figures 1.7(b),(c)), the horizontal construction line in the previous case being replaced by a set of vertical construction lines of constant $K_x = k_x + G_m$ where m is any integer. In the particular case of Figure 1.7, the values of K_x along the construction lines coincide exactly with the boundaries of the tiled first Brillouin zones. From the directions of the group velocity vector arrows in Figure 1.7(c), one can see that the group velocities of the Bloch modes (of which there are four, because all of the waves in this diagram are the components of four Bloch modes) excited within the crystal are all perpendicular to the x axis, so their group velocity components parallel to the interface are zero. In other words, the four Bloch modes are stationary in the plane of the interface. Figure 1.7(b) shows that in this case, the action of the grating upon incident light can produce backwards-propagating reflected rays in addition to the incident rays in the unpatterned medium. Reducing the distances between the Brillouin zone boundaries by increasing the pitch of the crystal will result in more construction lines intersecting the dispersion circle of the unpatterned medium, giving a spectrum of backwards-reflected and forwards-reflected rays.

In the case of a weakly modulated 'two-dimensionally patterned' crystal, the dispersion spheres will populate a plane rather than a line, because there will be a 2D lattice of grating vectors. If the frequency is high enough, neighbouring dispersion spheres will intersect and mutually repel at the Brillouin zone boundaries in a similar way to that

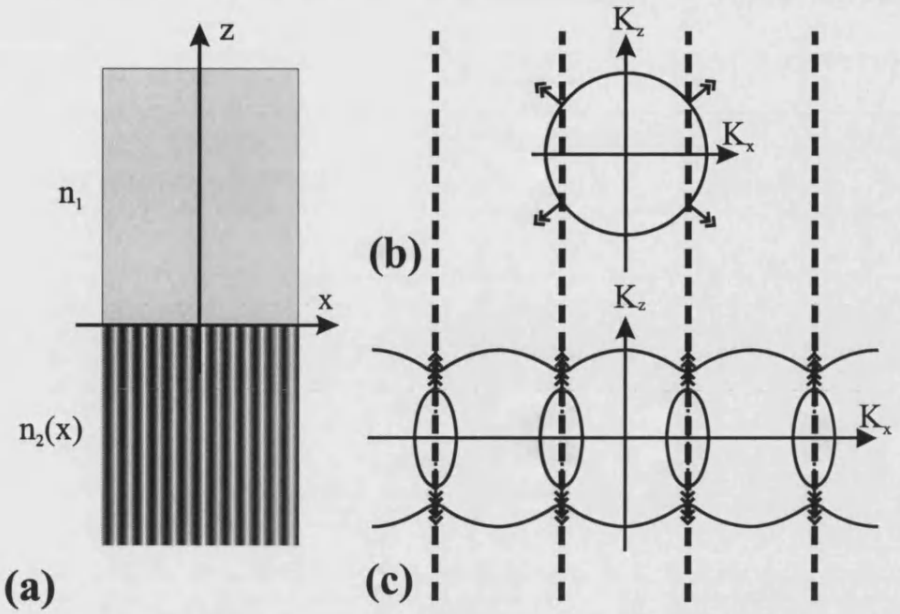

Figure 1.7: Illumination of a semi-infinite weakly-modulated photonic crystal from an unpatterned medium, where the interface between the two media is parallel to the grating axis. A diagram of the situation is shown in (a), whilst (b) and (c) are example wavevector diagrams for the unpatterned medium and the crystal respectively. Note that the origins of plots (b) and (c) coincide.

described above for the 1D case. Increasing the modulation depth and/or frequency can produce more complicated non-nearest-neighbour interactions between the dispersion surfaces, which is the reason why the two-wave weak-modulation model is not valid for high-index-contrast crystals or at high frequencies. However, the same basic principles are still applicable. Chapter 2 deals with the question of how to calculate the photonic bandstructure of a high-contrast crystal that has a 2D lattice of grating vectors.

1.1.5 Total reflection at normal incidence

Consider the situation shown in Figure 1.7. If we imagine that only one upwards-travelling Bloch mode in Figure 1.7(c) is somehow excited without incident light from above, and that the wavevector diagram for the unpatterned medium has a smaller radius than that shown in Figure 1.7(b), then the relevant wavevector diagrams may be as shown in Figure 1.8. The radiation cutoff circle (i.e. the locus of points at which $K_y = 0$, which gives a circle of the largest possible radius at fixed frequency along which the modes are non-evanescent) of the unpatterned medium, which is the dotted circle in Figure 1.8(a), is entirely accommodated within the boundaries of the first Brillouin zone. This implies that none of the plane-wave components of the single

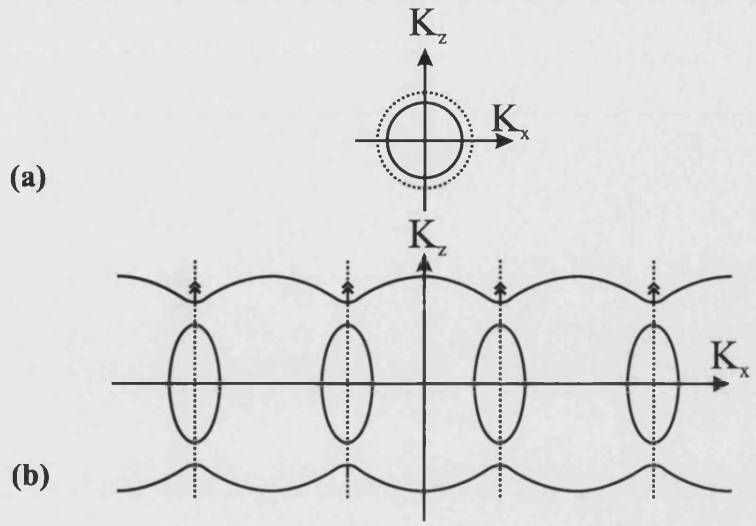

Figure 1.8: An illustration of the total internal reflection of a Bloch wave at normal incidence to an interface. Note that the origins of plots (a) and (b) coincide.

excited Bloch mode in Figure 1.8(b) are able to radiate into the unpatterned medium, giving total reflection of the Bloch wave at the interface. The upwards-travelling Bloch wave would therefore be totally internally reflected at normal incidence, which is one of the unusual things that an optical Bloch wave can do, and one that is of course impossible in conventional dielectric optics. Note that since K_y has been set to zero for convenience (as stated earlier), the wavevector diagrams for the unpatterned media exactly coincide with the cutoff loci, though they have been deliberately offset in Figure 1.8(a) to make it clear that they are not necessarily coincident. For nonzero values of K_y, however, any particular wavevector diagram would have a smaller radius than that of the corresponding cutoff locus, and they would therefore not coincide. A similar property of optical Bloch waves to that of total reflection at normal incidence to an interface can be exploited to produce, for example, a thin-film high Q-factor resonator. Chapter 3 deals with this in detail.

1.1.6 Bandgaps

The band-splitting effect described earlier can, if the refractive index contrast between the background material and the crystal basis (e.g. cylindrical holes, spherical holes, rectangular grooves) is sufficiently high, and if the dimensions of the crystal basis are sufficiently large compared with the lattice pitch, be increased to the extent that a wide band-gap [16] is formed. A band-gap is a frequency interval in which there is a total absence of propagating modes of a certain polarisation inside a photonic crystal, irrespective of wavevector magnitude, for all wavevectors parallel to at least

one direction. A 'full' 3D band-gap is an extreme case in which the modal suppression applies to all wavevector directions and all polarisation states. If the band-splitting effect is not sufficient in extent to create a bandgap of any sort at our operational optical frequency, then we will remain in the 'intra-passband state' regime.

1.1.7 Dispersion surface curvature and the effective mass tensor

The effective mass tensor m^{ij} for a general dispersion surface is defined to be

$$m^{ij} = \hbar\left[\partial^2\omega/\partial k_i \partial k_j\right]^{-1}, \tag{1.8}$$

in which $\omega(\underline{k})$ is the equation of the relevant surface. Since the dispersion surface curvature can be low at a passband edge, this equation implies that high effective photon masses are attainable in their locality. This fact leads to the concept of 'heavy light' [17].

Because the group velocity $\underline{v}_g$ is equal to $\partial\omega/\partial\underline{k}$, i.e. the $\underline{k}$- space gradient of the dispersion surface, the group velocity components resolved along a particular direction can be zero at a local dispersion minimum or maximum, implying that photons will form standing waves in space at these points. Low group-velocity optical Bloch waves can interact strongly with the materials constituting the photonic crystal (because the interaction strength typically depends on the reciprocal of the magnitude of the group velocity), thus enhancing nonlinear effects. This can be either very useful or a nuisance, depending on the situation. For example, in high-power data transmission and signal-processing applications, nonlinear effects can severely attenuate and distort the waveform or even result in overheating of the apparatus. Equally, a nonlinear effect may be the essential operational principle of a device that would be inconceivable in linear optics.

Another effect that can occur near a band-edge is that the density of photonic states may be sharply concentrated there, whilst the state density is reduced to zero in the midst of a bandgap. This allows photonic crystals to control spontaneous emission, either enhancing it at a band-edge or suppressing it entirely in a band-gap.

1.2 Practical photonic crystal microstructures

In practice, a photonic crystal can be classified in terms of its 'internal' and 'external' structure. The 'internal structure', in this context, refers to the three-dimensional

spatial refractive-index distribution of the crystal itself on an optical length-scale. A real, physical photonic crystal must be truncated so that it has a finite extent in space, and the way in which it is truncated determines what we will call its 'external structure'.

The internal structure has three distinct aspects: lattice, basis, and defects. The 'host crystal' microstructure is derived by convolving an abstract regular periodic lattice of delta-functions with a suitable crystal basis, and any intentional deviations from this otherwise regular host crystal, known as 'defects,' may be accounted for by deleting host-lattice points or by employing a different basis for some of them.

The internal structure may have a number of orthogonal axes of translational invariance, and if it does then taking account of them can considerably simplify calculations. In fact, not only does the presence of such translational invariance axes (TIAs) simplify calculations, but also it considerably simplifies fabrication. Indeed, the fabrication of photonic crystals having no TIAs that are intended to be employed at visible or near-infrared frequencies pushes technology to or beyond its limits (especially when wide bandgaps are desired), whilst those having one or two TIAs are much more manageable and yet are still very useful. Note that crystals having 0, 1, and 2 TIAs are normally respectively referred to as '3D', '2D', and '1D', but careless use of this conventional nomenclature can lead to ambiguity as to whether one is referring to the dimensionality of the space spanned by the set of grating vectors (and therefore to the 'internal' structure), or whether the 'external' structure is being described (as 'bulk', 'plane', or 'rod' respectively).

1.3 General aim of this thesis

Photonic crystals in the intra-passband regime make full use of the dispersion manipulating powers of photonic crystals, and they are the subject of this thesis. High-index-contrast thin-film photonic crystals (TFPCs), in which the refractive index is a 'strong' globally periodic 2D or 1D function of in-plane position, and where the film is optically thin, are worth investigating because the narrow separation between the upper and lower interfaces imposes a very strict field resonance condition that selects only certain linear combinations of Bloch modes for lossless (guided) or low-loss (quasi-guided) propagation within the film. This resonance condition, together with the strong angular and spectral dispersion properties of the underlying Bloch modes ensures that the guided and quasi-guided modes of a TFPC may be both highly dispersive and highly controllable, by virtue of the sensitivity of the Bloch modes to the internal structural parameters and by the dependence of the resonance condition on both the Bloch modes themselves and the thickness of the film.

We therefore want to investigate light propagation in 2D-patterned thin-film photonic crystals, and we must decide how this is to be done. Since we do not have any facilities for the fabrication of TFPC microstructures, we are at present restricted to modelling. Furthermore, since there is no analytical solution for the photonic bandstructure of a high-index-contrast 2D TFPC, numerical methods must be used. We want the modelling to be rigorous, so we must avoid some of the tenuous assumptions that are often found in the literature. This excludes, for example, the 'scalar field' approximation and any simplification involving the phrase 'average index'. There are essentially two routes along which we may proceed. These two routes may be called 'modal' and 'non-modal', and they differ fundamentally in the sense that one begins by calculating the Bloch eigenmodes, whilst the other does not. Non-modal methods are sufficient to obtain, for example, a transmittance spectrum of a particular TFPC having a given set of structural and electromagnetic parameters, thus treating the TFPC as a 'black box' that gives a certain 'output function' whenever it is presented with a certain 'input function'. Popular non-modal methods for photonic crystal simulation include FDTD [18] and beam-propagation [19]. If, however, it is necessary to be able to discover what is 'going on' inside the TFPC in terms of its eigenmodes in order to develop an intuitive understanding of its behaviour, then modal methods are required. We have therefore chosen a 'modal' method. A brief synopsis of previous research in the field of photonic crystals will now be given, together with an account of the motivations for the work described in each chapter.

1.4 Overview of previous work and how it relates to this thesis

Until quite recently, it was possible to give a comprehensive survey of photonic crystal research in a few pages. Now, however, the field has grown at such a rate that even a summary of a particular sub-topic is liable to be too long. It is therefore necessary to refer the interested reader to the various review articles [20, 21] that have been published, and also to a book entitled 'Photonic Crystals' [9]. There is also a review paper [22] that introduces the remarkable photonic crystal fibre (PCF). These fibres have periodically-microstructured cross-sections, and possess a wide variety of potential applications. A bibliography database of publications relating to photonic bandgaps is to be found on the WWW [23]. In this section, we must concentrate on our own particular corner of the field of photonic crystals: 2D-periodic thin-film photonic crystals.

1.4.1 Globally-periodic thin-film photonic crystals

Photonic crystal films, either thick or thin, may be fabricated by etching (e.g. electron-beam lithography or chemical etching) or deposition. Very good fully-etched uniformly periodic 2D-TFPC structures for use at near-infrared and visible wavelengths have already been successfully fabricated in *AlGaAs* [24, 25, 26] and their guided modes have been investigated [27] by the FDTD method (see later). Small group velocity [28], high effective mass [29], and strongly frequency-dependent angular dispersion [30] have been observed in them. Negative refraction effects [31], compact prisms [32] and miniature lenses [33] in infinitely thick 2D-patterned photonic crystals have also been modelled by FDTD.

Isolated point-defects can be introduced in 2D-TFPCs possessing bandgaps, creating very small-volume resonant microcavities with low photonic state densities (and therefore high differential quantum efficiencies). The microcavity modes in such structures have been modelled [34, 35, 36], and strong spontaneous-emission control in 2D-TFPCs has been predicted [37] and observed [38], suggesting that the efficiencies of LEDs and semiconductor lasers may be improved by using 2D-TFPCs.

Intra-bandgap line-defect waveguides, which can give controllable frequency-selective waveguidance, have been modelled [39] and fabricated [40, 41]. Line-defect waveguides act as 'photonic wiring', directing light along arbitrarily-shaped defect paths. Variations on this theme include Y-shaped (modelled in [42]) and cross-shaped (modelled in [43]) waveguides, which can perform frequency-selective beam-splitting.

The computation of the optical Bloch eigenmodes of a uniformly periodic high-index-contrast TFPC is covered in Chapter 2, whilst in Chapter 3 we deal with the calculation of the quasi-guided eigenmode spectrum of a TFPC and examine the properties of these modes in detail. The truly guided modes are investigated in Chapter 5. Initial work in this particular area was published by Atkin *et* al in 1985 [44, 45], who concentrated on the guided modes of a one-dimensionally patterned TFPC. Chapters 3 and 5 are an extension of this work to the quasi-guided and guided modes of a two-dimensionally patterned TFPC.

The guided and quasi-guided resonant modes of a TFPC have (exactly or approximately) cavity round-trip-invariant field distributions, whose Bloch wave composition (given by the vector of amplitudes $\underline{a}$) is such that $[C]\underline{a} = \eta\underline{a}$, where $[C]$ is the 'round-trip transformation operator' (see Chapter 5) and η is the 'out-of-plane loss coefficient'. The value of η is equal to unity for a guided mode and is typically slightly less (e.g. 0.999) for a quasi-guided mode. It is important to realise that these resonant modes are

not the only modes that the TFPC can support: non-resonant (or very low-Q-factor) combinations of Bloch modes can always be excited by illumination from above, so a TFPC will in general be transparent, unless we happen to be near an angle of incidence at which a quasi-guided mode (otherwise known as a high-Q radiative resonant mode) is excited.

The out-of-plane loss coefficient η of a resonant TFPC mode is directly related to its Q-factor. This can be shown in the following way. At resonance, the Q-factor of an ordinary Fabry-Perot cavity mode is given in terms of its amplitude reflection coefficients (r_1 and r_2) at the cavity boundaries by $Q = \pi/(\ln(1/r_1 r_2))$, as mentioned in Chapter 4 (but for intensity reflection coefficients instead). Reasoning by analogy and using the definition of the round-trip transformation operator in Chapter 5 gives the Q-factor of a TFPC resonance as $Q = \pi/(\ln(1/\eta))$, which implies that the out-of-plane loss coefficient is derivable from the Q-factor by the relation $\eta = \exp(-\pi/Q)$. The small but nonzero out-of-plane loss coefficients of the quasi-guided modes of a TFPC make them much easier to access than the guided modes: light can be efficiently coupled to or from them by the use of conventional optical fibres positioned above the film. The attainable coupling efficiency is high because the entire patterned surface area of the TFPC is involved, which results in much less diffraction than in end-fire coupling to a relatively narrow cleaved edge. This is a substantial advantage, because coupling has historically been a severe problem with TFPC waveguides: in many instances, a very good-quality structure is fabricated but is rendered almost useless by lack of provision for getting light in and out.

It is a remarkable fact that a 2D TFPC may still have guided and high-Q quasi-guided modes even if the thickness of the film is a very small fraction of the vacuum wavelength (e.g. 1%). At such thicknesses, an ordinary unpatterned thin-film would not have any resonances at all. This property of TFPCs allows devices based on them to be extremely compact. The resonant modes of a TFPC may be classified as 'air modes' or 'dielectric modes', according to the overlap of the field intensities with the low or high index regions (respectively) of the periodic patterning. The existence of distinct resonant air modes and dielectric modes enables the possibility of selective enhancement of linear or non-linear interactions of light with either a gas in the holes (in the case of a fully-etched 2D TFPC) or with the solid parts of the film. The in-plane group velocities of these resonances can be zero or very low, which can further increase the strengths of the light/matter interactions. Nonlinear effects such as second-harmonic generation [46, 47] in 2D-TFPCs have already been modelled, and the possibility of performing optical switching in nonlinear 1D-patterned photonic crystals has been predicted [48].

1.4.2 Merely locally periodic (MLP) thin-film photonic crystals

Reference [49] predicts that if we remove the restriction that the internal structure of the TFPC must be globally periodic and instead let it be merely locally periodic, then it is possible to engineer 'photonic force fields' of arbitrary shape. In this case, it is also possible to control the out-of-plane leakage to the extent that it is a 'designable' function of in-plane position.

A merely locally periodic (MLP) TFPC is such that one or more of its internal structural parameters are slowly-varying functions of in-plane position. The requirement of 'slow variation' is necessary to ensure that the power transfer between adjacent resonant local modes is as adiabatic as possible, thus avoiding large scattering losses due to optical impedance mismatch. These resonant local modes may be either quasi-guided or guided.

The situation in an MLP-TFPC is to some extent analogous to that in general relativity problems where the space is locally flat but globally curved, with the gravitational force being apparent only as a global property of a locally inertial spacetime: in an MLP-TFPC the resonant modes are locally those of a globally periodic TFPC but the large-scale photon trajectories are determined not by the local resonance dispersion surfaces $\omega_j(\underline{k}_p, \underline{r}_p)$ (where $\underline{r}_p$ is the in-plane position and $\underline{k}_p$ is the in-plane wavevector) but by a complicated function involving the integration of these surfaces over $\underline{r}_p$ and $\underline{k}_p$. A suitable formalism for calculating photon trajectories in MLP structures is to be found in Reference [49], in which Hamiltonian functions are employed. Reference [50] provides a good introduction to Hamiltonian optics.

The photon trajectories in an MLP-TFPC may be either closed or open. Closed trajectories could be employed in, for instance, a 'ring-resonator' laser in which light at the required lasing frequency is trapped in a bound orbit of constant radius around a fixed point inside the TFPC. In this variety of laser, the generated light may be allowed to tunnel tangentially out of the photonic potential well in which it is confined to activate neighbouring photonic circuitry, by simply placing it in close proximity.

MLP-TFPCs having open trajectories, on the other hand, may find applications as de-multiplexers in Wavelength Division Multiplexing systems (or, in reverse, as multiplexers) in the following way: the multiplexed signal is introduced by direct coupling from a fibre above the TFPC to quasi-guided resonant modes, which slowly transform into guided modes during propagation, each wavelength channel following a different route along the TFPC (without out-of-plane leakage for a large segment of each trajectory) to separate output ports, at which the internal structure is designed to be

such that each channel becomes quasi-guided, allowing light to couple into an array of output fibres. The original multiplexed signal is thus demultiplexed into its constituent channels, with low loss, by a compact device that can be made merely by patterning a thin-film.

In Chapter 6, a general method of modelling MLP-TFPCs is presented and illustrated with a simple example. Although this method is probably more computationally intensive than the Hamiltonian approach mentioned earlier, it is capable of handling more abrupt local-mode transitions. This might be necessary because there is a limit to the patterned area that an electron-beam lithography system can cope with without introducing 'stitching faults' in the locally periodic lattice. It is therefore possible that we will be restricted to make the modulation of the internal structural parameters rapid enough so that the patterned area can be accommodated within its practical limits.

1.4.3 Vertically-stacked multiple thin-film photonic crystals

Vertical-cavity surface-emitting lasers (VCSELs [51]) are important because they can be easily coupled to fibres for the same reason that the quasi-guided resonant modes of a TFPC can be easily coupled to fibres. In VCSELs, it is necessary to have both optical feedback and carrier confinement. Carrier confinement is achieved with 'barrier layers' having wider electronic bandgaps than the active medium in order to form a potential well for both electrons and holes. Optical feedback in a VCSEL is normally done by stacks of unpatterned layers of alternating refractive index (i.e. distributed Bragg reflectors, DBRs) placed above and below the barrier layers, which are very bulky and have high electrical resistance. TFPCs could perform the same function as DBRs in this application, but much more satisfactorily. TFPC reflectors may be very thin and may therefore have low electrical resistance, leading to a considerable reduction in the heating rate and a possible consequent increase in the maximum attainable light output power. TFPC-based VCSELs consisting of two TFPCs with a patterned or unpatterned defect layer sandwiched between them are modelled in Chapter 4, with the intention of finding a configuration in which the cavity mode eigenspectrum is easy to control whilst at the same time providing sufficient optical confinement. An attempt is then made to verify the practical viability of TFPC-VCSELs.

Chapter 2

Optical Bloch modes of a TFPC

2.1 Introduction

A basic pre-requisite of all of the calculations presented in this thesis is a generally applicable method of calculating the optical Bloch modes of a high-index-contrast two-dimensionally patterned TFPC, allowing for the possibility of out-of-plane free and evanescent propagation. A suitable scheme, successfully used before (although with a different representation of the refractive index function $n(x, y)$) for the computation of photonic crystal fibre modes [52, 53] and the photonic bandstructures of 2D TFPCs [44], will be described in this section. There is no analytic solution in the general case, so this method is numerical. The optical Bloch modes of a TFPC depend purely on its 'internal' structure as defined in the previous chapter, so a TFPC of any finite thickness has the same optical Bloch modes as one of infinite thickness. The calculation of the optical Bloch modes can therefore be greatly simplified by supposing that the TFPC is translationally invariant (continuously rather than discretely) parallel to its surface-normal.

2.2 Calculation method

Let us begin by stating Maxwell's equations [54]:

$$\underline{\nabla} \cdot \underline{B} = 0 \tag{2.1}$$

$$\underline{\nabla} \cdot \underline{D} = \rho \tag{2.2}$$

$$\underline{\nabla} \wedge \underline{E} = -\partial_t \underline{B} \tag{2.3}$$

$$\underline{\nabla} \wedge \underline{H} \;=\; +\partial_t \underline{D} + \underline{J} \tag{2.4}$$

We will assume that the magnetic permeability μ is a constant equal to that of the vacuum, μ_o, and that the electric permittivity ε is a real-valued positive-definite function of position. Another assumption that will be made is that of the absence of electric charge, which implies that $\rho = 0$ and $\underline{J} = \underline{0}$ at all points in space.

In units where $c = 1$ and $\varepsilon_o = 1$ (and hence $\mu_o = 1$), Maxwell's equations at fixed temporal angular frequency $k_o c$, under the assumptions described so-far, are as follows:

$$\partial_s H_s \;=\; 0 \tag{2.5}$$
$$\partial_n(\varepsilon E_n) \;=\; 0 \tag{2.6}$$
$$\epsilon_{pqr}\partial_q E_r \;=\; +ik_o H_p \tag{2.7}$$
$$\epsilon_{tuv}\partial_u H_v \;=\; -ik_o E_t \varepsilon \tag{2.8}$$

using the Levi-Civita pseudotensor notation with implicit summation over repeated indices.

Substituting 2.8 into 2.7 and remembering to assign unique letters to the indices over which implicit summation is to be suppressed:

$$H_p \;=\; \left(\frac{1}{ik_o}\right)\epsilon_{pqr}\partial_q E_r \;=\; \left(\frac{-i}{k_o}\right)\epsilon_{pqr}\partial_q\left(\frac{\epsilon_{rlm}}{-ik_o\varepsilon}\partial_l H_m\right) \tag{2.9}$$

Cyclically permuting the indices on the first Levi-Civita symbol, applying the chain rule for partial derivatives, and then decomposing the product of the two pseudotensors by the identity $\epsilon_{rpq}\epsilon_{rlm} = \delta_{pl}\delta_{qm} - \delta_{pm}\delta_{ql}$ gives:

$$H_p \;=\; \frac{-i}{-ik_o^2}\left(\delta_{pl}\delta_{qm} - \delta_{pm}\delta_{ql}\right)\left(\frac{1}{\varepsilon}\partial_q\left(\partial_l H_m\right) \;+\; \left(\partial_l H_m\right)\partial_q\left(\frac{1}{\varepsilon}\right)\right) \tag{2.10}$$

Using the fact that $\varepsilon\partial_q\left(\frac{1}{\varepsilon}\right) = -\frac{1}{\varepsilon}\partial_q\varepsilon$, this is equivalent to:

$$\varepsilon k_o^2 H_p \;=\; \left[\partial_m\left(\partial_p H_m\right) - \frac{1}{\varepsilon}\left(\partial_m\varepsilon\right)\left(\partial_p H_m\right)\right] - \left[\partial_l\left(\partial_l H_p\right) - \frac{1}{\varepsilon}\left(\partial_l\varepsilon\right)\left(\partial_l H_p\right)\right] \tag{2.11}$$

Partial derivatives of continuous functions commute, so, assuming spatial continuity of the components of the magnetic field vector, $\partial_m\left(\partial_p H_m\right) = \partial_p\left(\partial_m H_m\right)$. But we know from equation 2.5 that $\partial_m H_m = 0$, so $\partial_m\left(\partial_p H_m\right) = 0$. Hence:

$$\varepsilon k_o^2 H_p \;=\; \left[-\frac{1}{\varepsilon}\left(\partial_m\varepsilon\right)\left(\partial_p H_m\right)\right] - \left[\partial_l\left(\partial_l H_p\right) - \frac{1}{\varepsilon}\left(\partial_l\varepsilon\right)\left(\partial_l H_p\right)\right] \tag{2.12}$$

Re-ordering the terms and realising that $\partial_l\partial_l H_p \;\equiv\; \partial_m\partial_m H_p$ and $\left(\partial_l\varepsilon\right)\left(\partial_l H_p\right) \;\equiv$

$(\partial_m \varepsilon)(\partial_m H_p)$ gives the general equation

$$\varepsilon k_o^2 H_p = \frac{1}{\varepsilon}(\partial_m \varepsilon)[\partial_m H_p - \partial_p H_m] - \partial_m \partial_m H_p \tag{2.13}$$

Note that the implicit summation is over the three axes x, y, z.

We can simplify this equation by exploiting the fact that when calculating the Bloch modes the photonic crystal can be assumed to be translationally invariant along the z-axis. Let us use Greek letters to denote the 'in-plane' (ie parallel to the plane of periodicity) axes x and y. Then, after enforcing the translational invariance requirement $\partial_z \varepsilon = 0$, we obtain, finally:

$$-\partial_z^2 H_\nu = \left[\varepsilon k_o^2 + \partial_\mu \partial_\mu\right] H_\nu + C_\mu [\partial_\nu H_\mu - \partial_\mu H_\nu] \tag{2.14}$$

where we have defined the vector function C_μ such that $C_\mu \equiv \frac{1}{\varepsilon}\partial_\mu \varepsilon$. Note that equation 2.14 involves only the in-plane components of the magnetic field.

The translational invariance of the crystal along the z-axis has further implications. Since photons moving within the structure will not encounter a refractive index variation along the z axis, they will not experience any forces directed along the z axis, and so the z-component of the momentum of any photon will be constant. The three-momentum associated with a Fourier component of a photon wavefunction having wavevector $\underline{k}$ will be simply $\hbar \underline{k}$. Hence k_z will be a constant for any particular Fourier component. Let us call this constant β. A Bloch mode of the crystal is a linear combination, of all plane waves having β and $\underline{k}$ in common, which satisfies equation 2.14. Note that the words 'wavevector' and 'momentum' will be used synonymously from now on, because they are merely related by the constant scaling factor $\hbar$.

The periodicity of ε implies that $\varepsilon(\underline{r} + \underline{R}) = \varepsilon(\underline{r})$ where $\underline{R}$ is any lattice vector. The vector function C_μ also has this property since it is derived purely from ε. This places a restriction on the wavevectors $\underline{G}$ that can appear in the Fourier expansions of ε and C_μ: they must satisfy the condition $\underline{G} \cdot \underline{R} = 2\pi N$ where N is any integer. A vector satisfying this condition is said to belong to the 'reciprocal lattice' [55], and we shall assign a *single unique index* to each member of the infinite set of reciprocal lattice vectors. The set of wavevectors involved in the Fourier expansion of H_μ cannot be assumed to be the same as for the previous functions, so we will refer to this set as $\{\underline{K}\}$ rather than $\{\underline{G}\}$.

The following Fourier expansions, expressed in Dirac notation [56], will be used in

conjunction with equation 2.14:

$$\varepsilon = |\underline{G}^i\rangle\langle\underline{G}^i|\varepsilon\rangle \tag{2.15}$$

$$C_\mu = |\underline{G}^i\rangle\langle\underline{G}^i|C_\mu\rangle \tag{2.16}$$

$$H_\alpha = |\underline{K}^i\rangle\langle\underline{K}^i|H_\alpha\rangle \tag{2.17}$$

where summation over repeated indices is implicit, as before, and where '$\langle\ \rangle$' indicates normalised 2D integration over the unit cell (i.e. normalised in the sense that it is divided by the area of the unit cell).

Our abbreviations for the various projections onto the elements of the Fourier basis set are given below:

$$\varepsilon^i \equiv \langle\underline{G}^i|\varepsilon\rangle \tag{2.18}$$

$$C^i_\mu \equiv \langle\underline{G}^i|C_\mu\rangle \tag{2.19}$$

$$H^i_\alpha \equiv \langle\underline{K}^i|H_\alpha\rangle \tag{2.20}$$

Let us substitute these expansions into equation 2.14:

$$\beta^2|\underline{K}^i\rangle H^i_\nu = \left[\varepsilon^i|\underline{G}^i\rangle k_o^2 - K^i_\mu K^i_\mu\right]|\underline{K}^i\rangle H^i_\nu + C^i_\mu|\underline{G}^i\rangle\left[iK^i_\nu H^i_\mu - iK^i_\mu H^i_\nu\right]|\underline{K}^i\rangle \tag{2.21}$$

Now if we project both sides of this equation onto a fixed basis vector $|\underline{K}^j\rangle$ we can determine the relation between the members of the sets $\{\underline{K}\}$ and $\{\underline{G}\}$:

$$\begin{aligned}\beta^2\langle\underline{K}^j|\underline{K}^i\rangle H^i_\nu = &\left[\varepsilon^i\langle\underline{K}^j|\underline{G}^i+\underline{K}^i\rangle k_o^2 H^i_\nu - K^i_\mu K^i_\mu\langle\underline{K}^j|\underline{K}^i\rangle H^i_\nu\right] \\ &+ iC^i_\mu\langle\underline{K}^j|\underline{G}^i+\underline{K}^i\rangle\left[K^i_\nu H^i_\mu - K^i_\mu H^i_\nu\right]\end{aligned} \tag{2.22}$$

The Fourier projection $\langle\underline{K}^j|\underline{G}^i+\underline{K}^i\rangle$ is equivalent to $\delta_{(\underline{K}^j),(\underline{G}^i+\underline{K}^i)}$, so nontrivial solutions of the above equation will exist only when $\underline{K}^j - \underline{K}^i = \underline{G}^i$. In other words, any two members of the set $\{\underline{K}\}$ must differ by a reciprocal lattice vector. Hence the lattice of allowed $\underline{K}$ vectors must simply be a translated copy of the reciprocal lattice. Let the required translation vector be $\underline{k}$. Then $\underline{K}^i = \underline{G}^i + \underline{k}\ \forall i$, where the components of $\underline{k}$, k_x and k_y, are parameters.

Equation 2.14 can be expressed in matrix form by substituting the expansion for H_α into it and then projecting both sides of the resulting equation onto a fixed basis vector $|\underline{K}^j\rangle$, as before:

$$\beta^2\delta^{ij}H^i_\nu = \langle\underline{K}^j|\varepsilon|\underline{K}^i\rangle k_o^2 H^i_\nu - K^i_\mu K^i_\mu H^i_\nu\delta^{ij}$$

$$+ i\left\langle \underline{K}^j \mid C_\mu \mid \underline{K}^i \right\rangle \left[K^i_\nu H^i_\mu - K^i_\mu H^i_\nu\right] \tag{2.23}$$

Let us define the following matrix elements:

$$\varepsilon^{ji} = \left\langle \underline{K}^j \mid \varepsilon \mid \underline{K}^i \right\rangle \tag{2.24}$$

$$C^{ji}_\mu = \left\langle \underline{K}^j \mid C_\mu \mid \underline{K}^i \right\rangle \tag{2.25}$$

Then our equation in matrix form is simply:

$$\beta^2 \delta^{ji} H^i_\nu = \left(\varepsilon^{ji} k_o^2 - K^i_\mu K^i_\mu \delta^{ji}\right) H^i_\nu + i C^{ji}_\mu \left[K^i_\nu H^i_\mu - K^i_\mu H^i_\nu\right] \tag{2.26}$$

The advantage of this matrix form is that there is no dependence on the position vector $\underline{r}$. Now, if $\nu = x$ then $C^{ji}_x \left[K^i_\nu H^i_x - K^i_x H^i_\nu\right] = 0$ and if $\nu = y$ then $C^{ji}_y \left[K^i_\nu H^i_y - K^i_y H^i_\nu\right] = 0$. So if we make the following definitions (in which summation is not to be assumed):

$$P^{ji}_{\nu\mu} = -i \begin{pmatrix} +C^{ji}_y K^i_y & -C^{ji}_y K^i_x \\ -C^{ji}_x K^i_y & +C^{ji}_x K^i_x \end{pmatrix} \tag{2.27}$$

$$S^{ji} = k_o^2 \varepsilon^{ji} - ({K^i_x}^2 + {K^i_y}^2)\delta^{ji} \tag{2.28}$$

$$M^{ji}_{\nu\mu} = \left(S^{ji}\delta_{\nu\mu} + P^{ji}_{\nu\mu}\right) \tag{2.29}$$

and use the identity $H^i_\nu \equiv \delta_{\nu\mu} H^i_\mu$ then equation 2.26 reduces to:

$$M^{ji}_{\nu\mu} H^i_\mu = \beta^2 H^j_\nu \tag{2.30}$$

Matrix M (which we will call the 'bandstructure matrix') has two parts: a part that *does not* couple the polarisations, S^{ji}, and a part that *does* couple the polarisations, $P^{ji}_{\nu\mu}$. The practical form of matrix M consists of four submatrices, each submatrix being a quadrant of M. The pair of indices ν and μ specify the quadrant, whilst j and i specify the row and column (respectively) within each quadrant.

The factor $\exp(i(\beta z - k_o ct))$ is common to both sides of equation 2.30, so it can be cancelled-out to give the 'bandstructure equation' (where $H^l_\zeta = h^l_\zeta \exp(i(\beta z - k_o ct))$):

$$M^{ji}_{\nu\mu} h^i_\mu = \beta^2 h^j_\nu \tag{2.31}$$

which is the matrix eigensystem that must be solved in order to obtain the Bloch modes of the TFPC. Of course, the matrix M, as it stands, has dimensions $\infty \times \infty$. In practice it must be truncated so that it contains a finite number of elements. One must retain a sufficiently large number of the most significant elements such that if one significantly increases the number of elements retained then the eigensolutions are not significantly altered.

Equation 2.31 states that the elements of an eigenvector of the matrix M are the Fourier coefficients from which an allowed field distribution (a 'Bloch mode') can be constructed, and that the eigenvalue corresponding to this particular eigenvector is the value of β^2 associated with all of the plane waves constituting this field distribution.

2.3 Calculation of the matrix elements ε^{ji}, $\overline{\varepsilon}^{ji}$, and C_{μ}^{ji}

All of the functions C_{μ}, ε, and ε^{-1} are derived entirely from the in-plane refractive index distribution of the photonic crystal film, and when calculating the matrix elements ε^{ji}, $\overline{\varepsilon}^{ji}$, and C_{μ}^{ji} it is necessary to decide on the best way of representing this refractive index distribution. The choice is important and nontrivial, since if one is not careful then the calculated eigenvectors of the matrix M may be very slow to converge to the true Bloch modes with respect to the number of reciprocal lattice vectors used in the Fourier expansions.

When modelling a triangular lattice of cylindrical holes, for example, we have two choices for the functional form of ε: continuous or discontinuous. The discontinuous form of $\varepsilon(x,y)$ will be a radial step-function convolved with a 2D triangular lattice of delta functions, whilst a simple continuous form of $\varepsilon(x,y)$ might be a function involving the exponential term $\exp(-(r/w)^{2n})$, where r is the radial position, n is a positive integer, and w is the hole 'waist'. The latter function, which is known as a 'super-Gaussian' has the advantage that its Fourier transform is uniformly convergent, so it avoids the Gibbs phenomenon, in which the ε distribution reconstructed from its truncated Fourier expansion is found to overshoot or undershoot at the discontinuities. The Gibbs phenomenon is a problem when one adopts the discontinuous form of $\varepsilon(x,y)$ if the use of a very high number of plane waves (of the order of thousands) is impractical, such as in our case. We shall use the continuous form mentioned above in our calculations, by default, together with the approximation that the 2D integrals involved decay with sufficient rapidity as one approaches the periphery of the largest circle that can be accommodated within the boundaries of the unit cell such that they can be neglected beyond that circle, thus allowing the 2D integrals to be accurately approximated by 1D integrals. These 1D integrals can be easily evaluated numerically, and this approximation is due to Dr E. Silvestre (see Acknowledgements).

2.4 Choice of internal structure

In this thesis, we will concentrate on TFPCs having internal structures consisting of triangular lattices of cylindrical holes etched into high-index dielectric materials. The direct and reciprocal lattices in this case case are shown schematically in Figures 2.1(a) and 2.1(b) respectively. The reason for choosing the triangular lattice rather than the simple square lattice is that its Brillouin zones are more circular than those of a square lattice, which makes the existence of full 3D 'resonance gaps' (i.e. frequency bands inside which there are no resonant modes, irrespective of wavevector direction and magnitude) more likely, if they are required in a particular application. Resonance gaps are distinct from band-gaps and they will be discussed later. Holes were chosen instead of solid pillars because quasi-guided and guided modes are more likely to be found if the TFPC is mostly solid material rather than mostly air, from simple refractive index considerations, and cylindrical holes have the advantage that they are relatively easy to produce for use at near-infra-red wavelengths [57, 24].

Since we are interested only in the intra-pass-band regime, parameter ranges in which band-gaps exist will be deliberately avoided. Basically, this implies that we will work with holes that are relatively small and fairly widely separated. A $\beta(\underline{k})$ bandstructure diagram, at fixed optical frequency, of a typical TFPC in the intra-pass-band regime is shown in Figure 2.2. In this case, the frequency corresponds to a vacuum wavelength of 980nm, the lattice pitch Λ is 500nm, the cylindrical holes have diameters of 112nm, and the background refractive index n_b of the TFPC is 3.46. Note that this bandstructure diagram shows only the members of the β^2 eigenspectrum of the bandstructure matrix M that have real-valued square-roots (i.e. real-valued out-of-plane propagation constants), and that the horizontal axis is the in-plane wavevector along a closed triangular circuit going between the vertices of the irreducible portion of the first Brillouin zone, from Γ to J to X, and finally back to Γ. Note also that on this diagram, one can find at least one propagating Bloch mode having any given value of $\beta\Lambda$ between the upper and lower limits $+n_b k_o \Lambda$ and $-n_b k_o \Lambda$ (i.e. between approximately 11.09 and -11.09).

A sixth-order super-Gaussian function will henceforth be used to model the refractive index in the neighbourhood of a hole. There is unpublished evidence (according to the authors of Reference [24]) to suggest that, in practical TFPCs, a certain amount of oxidation occurs at the boundaries of each hole, which tends to lower the index around the holes. The lattice of super-Gaussian functions may therefore be a more accurate model for the refractive index profile of a real TFPC than a lattice of radial step-functions, in addition to being more numerically viable.

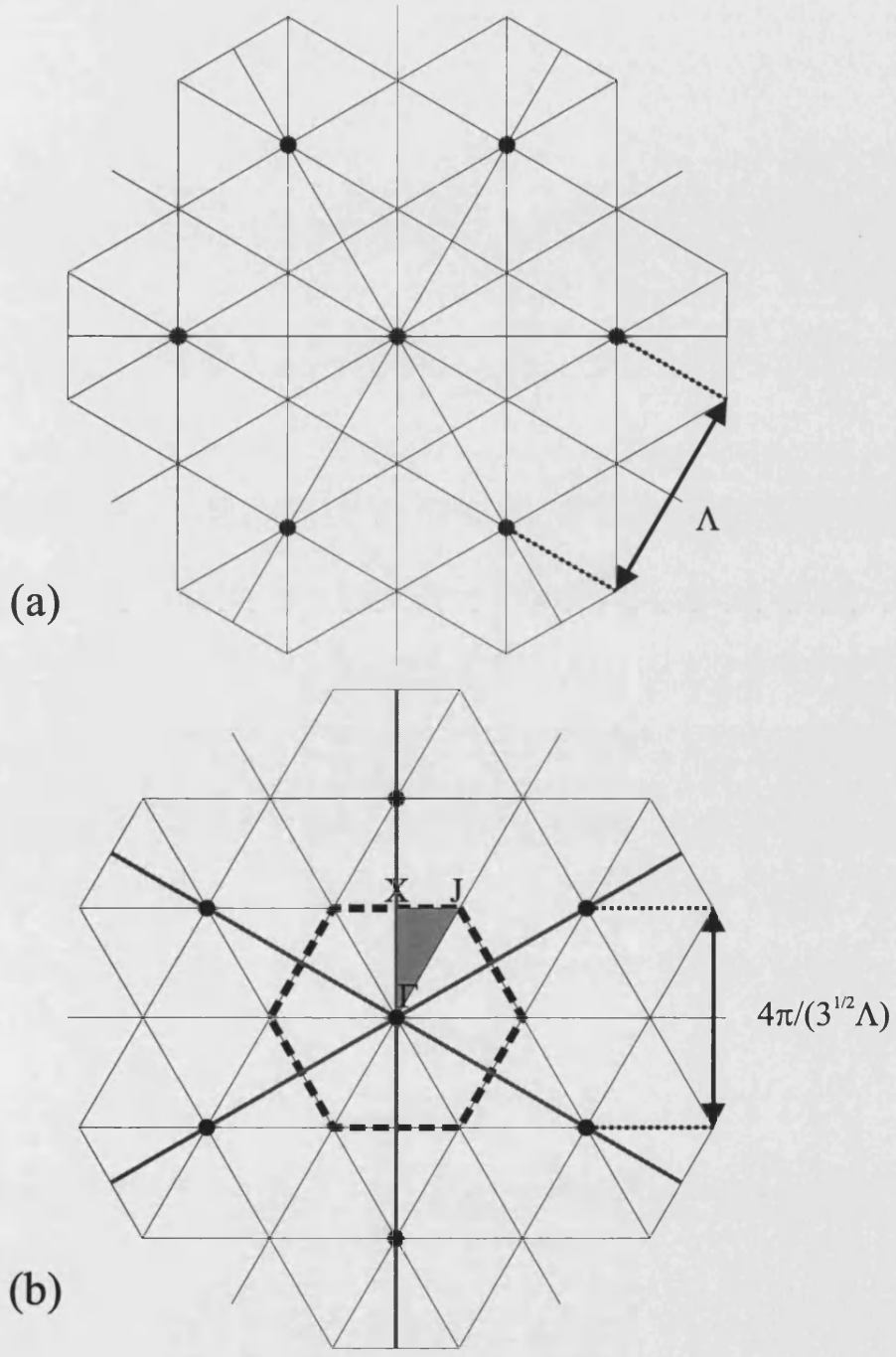

Figure 2.1: The direct (a) and reciprocal (b) lattices for a triangular array (not to scale). The boundaries of the first Brillouin zone are marked with dashed lines in (b), and its irreducible portion is shaded.

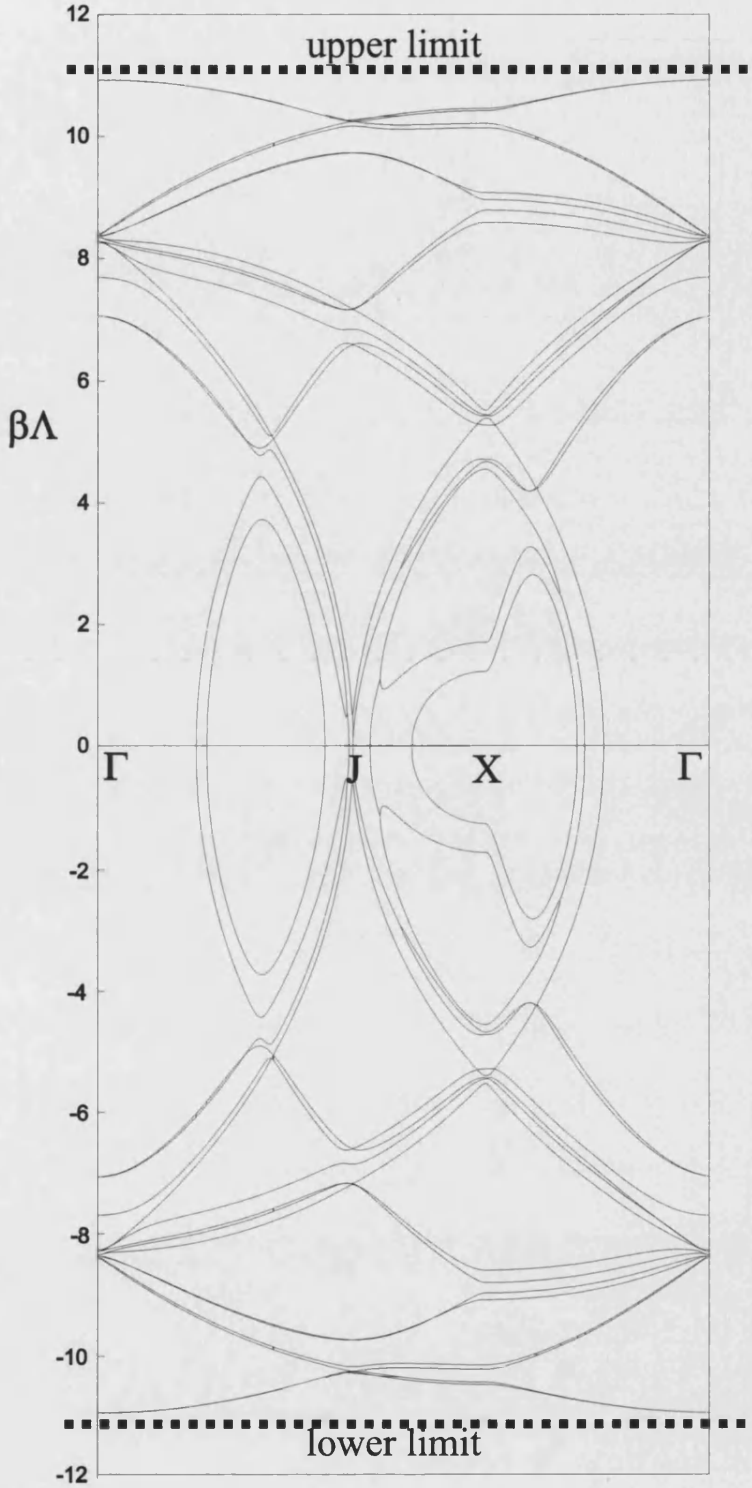

Figure 2.2: $\beta(\underline{k_p})$ bandstructure of a triangular lattice of holes, at constant operational optical frequency. The upper and lower limits of $\beta\Lambda$ are marked with dotted lines.

2.5 Supercells

To allow for the presence of intentional defects in the crystal (as in Chapter 6), such as the absence of a hole in an otherwise perfectly periodic array of holes, the following method (borrowed from solid-state physics) can be employed [52]. The Bloch modes of a structure having a defect may be calculated by tiling a truncated version of it (a so-called 'supercell') to fill an infinite plane, whereupon it becomes a periodic structure again. Provided that the distance between neighbouring defects is sufficiently large, each defect is effectively isolated from its neighbours, because the fields decay exponentially as one moves away from the defect, so that they are effectively zero at the boundaries of the supercell. Even though the defect modes are not strictly Bloch modes, they are nevertheless true Bloch modes of the tiled truncated structure. The evaluation of the matrix elements ε^{ji}, $\overline{\varepsilon}^{ji}$, and C_{μ}^{ji} of a supercell structure may be done by first calculating an integral $\mathcal{I}$ over one hole. The integral over any other hole in the supercell is related to this integral $\mathcal{I}$ by a phase-factor that takes account of its position within the supercell (which can be proved simply by a change of variables in the integration). The integral over the entire supercell is then merely the sum of all such integrals. Of course, it is also possible to use the same technique to calculate the Bloch modes of a structure that really does tile in this way, rather than using it as an approximation to a structure that does not.

Figure 2.3 shows contour and surface plots of the electric field intensity, at a frequency corresponding to a vacuum wavelength of 980nm, of a defect mode in a host crystal that has the same parameters as in Figure 2.2. Since the host crystal does not have a band-gap at this frequency, Figure 2.3 demonstrates that it is not necessary to have an in-plane band-gap in order for a defect mode to exist. This fact should be well-known but it is often overlooked. Here, the in-plane confinement of the fields within the tiled defects is due to the raised index of the defect relative to that of the surrounding host crystal, which is the guidance mechanism of non-bandgap photonic crystal fibres [22].

2.6 Conclusions

In this chapter, we have explained the implementation of a method of calculating the Bloch modes of a TFPC, based on the Fourier expansion technique, that will be used in the subsequent chapters. The way that we have chosen to represent the refractive index function $n(x, y)$ inside the TFPC guarantees that the accuracy of the eigenmode solutions will increase monotonically as the number of expansion basis elements increases. This scheme also allows the inclusion of defects in an otherwise regular periodic struc-

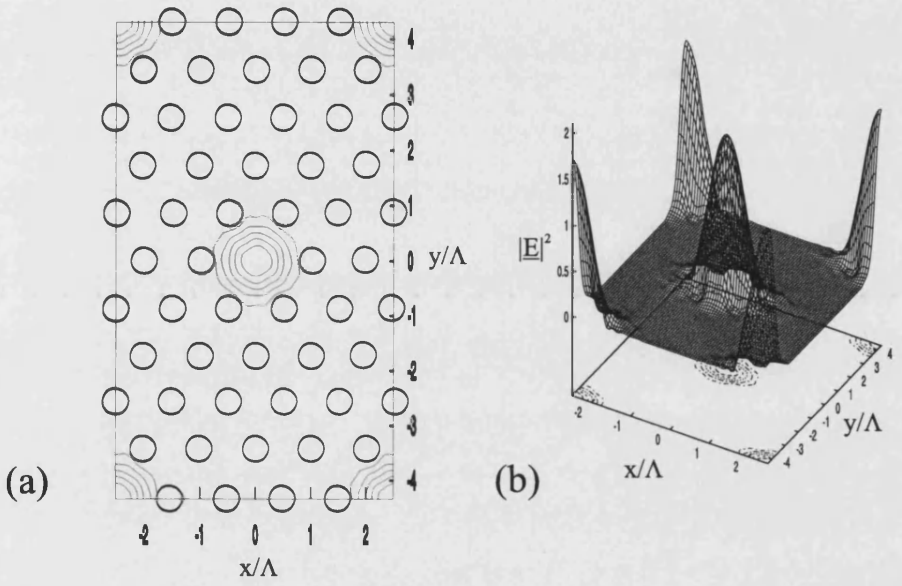

Figure 2.3: (a)Isocontour plot and (b) surface plot of the electric field intensity of a defect mode, within a plane of constant z-coordinate. Note that the host crystal, which has the same parameters as for Figure 2.2, has no bandgap at this frequency (which corresponds to a vacuum wavelength of 980nm). The centres of the missing holes form a triangular array having pitch 5Λ where Λ is the lattice pitch of the host crystal. The electric field intensity is given in arbitrary units, and the circles represent the hole-boundaries.

ture, if required. We have also justified our choice of internal structure; namely, that of the triangular lattice of cylindrical holes. Of course, the Bloch modes of a TFPC will not all be of equal significance: some will be weakly excited upon internal or external illumination, whilst others may be strongly excited, and one can only determine the relative intensities of the excited Bloch modes by imposing boundary conditions on the electric and magnetic fields, which will be the subject of the next chapter.

Chapter 3

Radiative resonant modes of a TFPC

3.1 Introduction

In this chapter, which constitutes the foundation upon which the remaining chapters are built, the fundamental characteristics of the radiative modes of uniformly-periodic TFPCs are investigated. The content of this chapter has been published in a single paper [1], subsequent to which there has been a sudden avalanche of publications on similar topics, although mostly with a very different emphasis, reflecting a recent revival of interest in thin-film photonic crystals.

The fact that the eigenmodes of a thin-film photonic crystal (TFPC) can be highly dispersive, in terms of both frequency and in-plane angle, implies that they could potentially form the basis of a new family of ultra-compact optical devices. That is one of the motivations for this work, apart from its intrinsic interest. References [58] and [59] demonstrate that low-index-contrast TFPCs can perform novel functions such as 'beam-squeezing'. The practicality of using high-index-contrast TFPCs containing point defects as VCSEL microcavities has been verified in Reference [60] (TFPC-based VCSEL cavities without point defects will be discussed in Chapter 4). It has also been confirmed that Wavelength-Division Multiplexing can be done with relatively thick photonic crystal films [61]. Reassuringly, the authors of Reference [62], although working in a different parameter regime to us, have at least observed low-Q resonances in TFPCs, in a series of experiments, and have obtained favourable agreement with their numerical modelling.

By the time-reversal symmetry of Maxwell's equations, the radiative modes of a TFPC can be calculated by the imposition of boundary conditions under external illumination of the film, following the computation of its Bloch eigenmodes as described in Chapter 2. The 'inputless' case, yielding the truly-guided modes, requires a non-trivial extension of the techniques dicussed here. This will be covered in chapter 5.

The structure (shown in Figure 3.1) to be considered in this chapter is a TFPC consisting of a triangular lattice of hollow cylinders bounded by two parallel planar interfaces, which are separated by a distance L that is typically no greater than the lattice pitch (to avoid the existence of too many modes, which is often a practical requirement). In this case, the internal structure of the TFPC itself has one axis of translational invariance, and this axis (the z axis) will be aligned so that it is normal to the interface-planes. The TFPC will be assumed to be infinite in extent in the plane of the film, and a validation of this assumption is to be found in Chapter 6.

In order to determine the optical response of a TFPC to incident light, it is necessary to first calculate the set of z-evanescent and z-propagating modes of the film, and also the z-evanescent and z-propagating modes of the semi-infinite unpatterned media above and below the patterned film. A unique solution in a given situation can be obtained by imposing the constraint that the $\underline{E}$ and $\underline{H}$ field vector components parallel to the plane of the TFPC film must be continuous functions with respect to the z-coordinate.

There are several ways of imposing the required boundary conditions. Perhaps the most obvious of these is simply to construct a single matrix equation that expresses all of the boundary conditions, which is then solved with a linear matrix equation solution routine. I will call this the 'direct' method. Another method is to consider each interface individually, constructing separate coefficient matrices for each interface, from which one can derive the coefficient matrix of the entire TFPC by one of two possible routes. This will be called the 'indirect' method. The direct method of solution will be used in this chapter to investigate the properties of the radiative resonant modes of a TFPC. In subsequent chapters, more flexible 'indirect' methods will be employed. However, the 'direct' method is sufficient for our present purposes, and it also provides a convenient way of checking the accuracy of more elaborate approaches. This method was first proposed in 1995 [20] and has been used before for the calculation of the truly- guided modes [44, 45] of TFPCs possessing two axes of translational invariance (i.e. having so-called '1D periodicity'). The work presented in this chapter is effectively an extension of that published in the three papers referred-to above, although here we deal with the high-Q quasi-guided modes of '2D-patterned' TFPCs rather than with the guided modes of '1D-patterned' TFPCs.

3.2 Description of the 'direct solution' method

It can be shown that the solutions (i.e. the Bloch modes) of the matrix eigensystem derived in the previous chapter form a *complete set* in terms of which the field distribution inside a 2D photonic crystal film can be expressed. Let $\{B_\mu^j \exp(i(\beta_j z - k_o ct))\}$ be the set of Bloch modes (with no implicit summation). Each Bloch mode can in turn be expressed as a linear superposition of the elements of the Fourier basis set, and we shall use the symbol $B_{\mu,i}^j$ to denote the i^{th} Fourier component of the projection along the μ axis of the j^{th} Bloch mode, excluding the factor $\exp(i(\beta_j z - k_o ct))$.

The $B_{\mu,i}^j$ are, in fact, the eigenvectors of the 'bandstructure matrix' M (see Chapter 1), which is in general non-Hermitian. The eigenvalues β_j^2 will always be real, which allows the z-momenta β_j of the eigenmodes to be either purely real or purely imaginary. Hence there will be some Bloch modes that are evanescent along the z axis, and some that are non-evanescent along the z-axis. For any Bloch mode corresponding to a particular complex value of β there must also exist another Bloch mode corresponding to a negated version of that β value, because the eigenvalues of M are $\{\beta_j^2\}$, and $(-\beta_j)^2 = \beta_j^2$. Hence the most general solution for the fields inside a 2D photonic crystal film must be a linear combination of Bloch modes having both positive and negative complex momenta along the z axis. So we will construct two Bloch mode sets of equal size, $\{B_\mu^j \exp(i(+\beta_j z - k_o ct))\}$ and $\{B_\mu^j \exp(i(-\beta_j z - k_o ct))\}$, from the set of eigenvectors of matrix M, $\{B_{\mu,i}^j\}$, the corresponding modes from each set differing only by reflection.

From elementary considerations, the in-plane components of the $\underline{E}$ and $\underline{H}$ fields must be continuous functions of position, even where the electric permittivity has a finite discontinuity. The steady-state field distribution that will be established when one shines light at a photonic crystal film must be that which satisfies these boundary conditions at both the upper and lower interfaces simultaneously. Note that it is not possible to obtain a unique solution to the fields by imposing the boundary conditions separately: both boundaries must be dealt-with at the same time to obtain a self-consistent solution.

The μ-component of the magnetic field inside the photonic crystal film can be written in the following form (using implicit summation again):

$$H_\mu^{CRYSTAL} = b_j^+ \exp(+i\beta_j z)\exp(-ik_o ct)B_\mu^j + b_j^- \exp(-i\beta_j z)\exp(-ik_o ct)B_\mu^j \quad (3.1)$$

where

$$B_\mu^j = B_{\mu,i}^j \left|\underline{K}^i\right\rangle \quad (3.2)$$

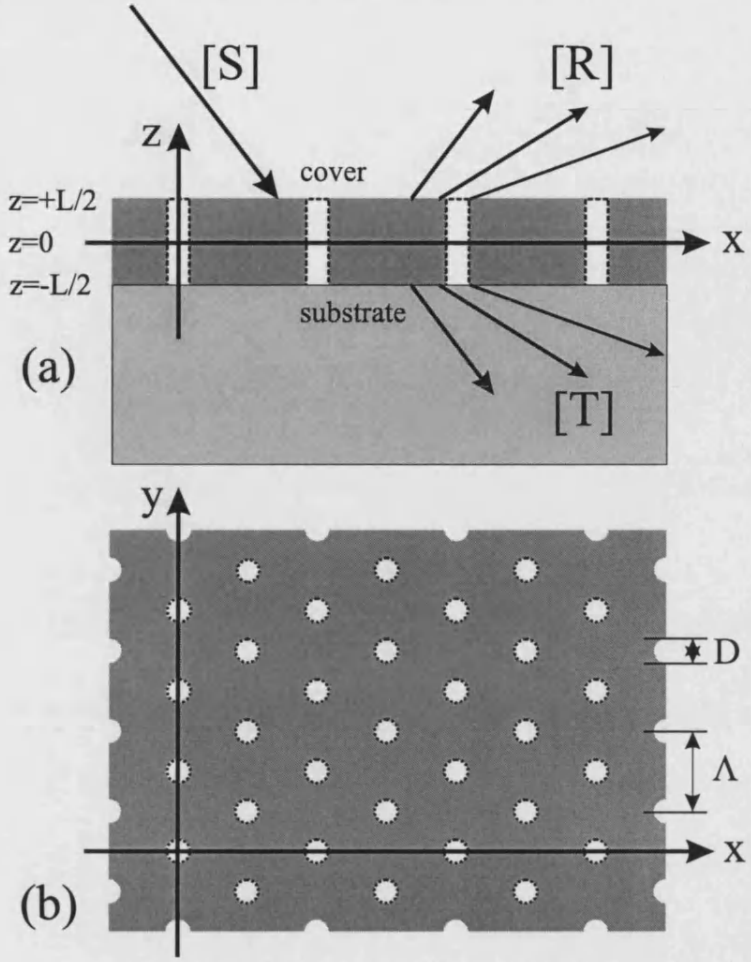

Figure 3.1: A schematic diagram of the structure to be analysed. A cross-sectional view is given in (a), cutting through a row of holes, and a plan view is given in (b). The origin of the (x, y) plane coincides with the major axis of a cylindrical hole, whilst the origin of the z axis is such that the plane $z = 0$ is half-way between the upper and lower interfaces at $z = L/2$ and $z = -L/2$ respectively.

and μ is either x or y. Consider the situation in which the photonic crystal film is sandwiched between two semi-infinite unpatterned media and illuminated by a plane wave from above. This is shown schematically in figure 3.1. Now, in the medium above the film (the 'cover', medium 1) from which light is assumed to be incident, we have the following contributions to the total in-plane magnetic field:

$$H_\mu^{SOURCE} = w_{S,\mu}^i \exp(-i\alpha_1^i z)\exp(-ik_o ct)\left|\underline{K}^i\right\rangle \tag{3.3}$$

$$H_\mu^{REFLECTED} = w_{R,\mu}^i \exp(+i\alpha_1^i z)\exp(-ik_o ct)\left|\underline{K}^i\right\rangle \tag{3.4}$$

where $w_{S,\mu}^i$ and $w_{R,\mu}^i$ are the incident ('source') and reflected amplitudes and $\{\alpha_1^i\}$ is the set of z-momenta determined from $K_z^i = \sqrt{k_o^2\varepsilon - \left((K_x^i)^2 + (K_y^i)^2\right)}$. Similarly, the

in-plane magnetic field components in the second unpatterned region (the 'substrate', medium 2) will be:

$$H_{\mu}^{TRANSMITTED} = w_{T,\mu}^{i} \exp(-i\alpha_2^i z) \exp(-ik_o ct) \left| \underline{K}^i \right\rangle \tag{3.5}$$

We can think of the index i as a number specifying a particular ray of light, and the electric field components of the i^{th} ray can be obtained from its in-plane and out-of-plane magnetic field components by applying Maxwell's equations (in which summation is not to be assumed):

$$\underline{E}_{3D}^{i} = -\frac{1}{k_o c\varepsilon} \underline{K}_{3D}^{i} \wedge \underline{H}_{3D}^{i} \tag{3.6}$$

$$i\underline{K}_{3D}^{i} \cdot \underline{H}_{3D}^{i} = 0 \tag{3.7}$$

Hence

$$E_{\mu}^{SOURCE} = -\frac{1}{k_o c\varepsilon_1} \left(\underline{K}_{3D}^{i} \wedge \underline{H}_{3D}^{SOURCE,i} \right)_{\mu} \tag{3.8}$$

$$E_{\mu}^{REFLECTED} = -\frac{1}{k_o c\varepsilon_1} \left(\underline{K}_{3D}^{i} \wedge \underline{H}_{3D}^{REFLECTED,i} \right)_{\mu} \tag{3.9}$$

$$E_{\mu}^{TRANSMITTED} = -\frac{1}{k_o c\varepsilon_2} \left(\underline{K}_{3D}^{i} \wedge \underline{H}_{3D}^{TRANSMITTED,i} \right)_{\mu} \tag{3.10}$$

$$E_{\mu}^{CRYSTAL} = -\frac{1}{k_o c} \varepsilon_{CRYSTAL}^{-1}(\underline{r}) \left(\underline{K}_{3D}^{i} \wedge \underline{H}_{3D}^{CRYSTAL,i} \right)_{\mu} \tag{3.11}$$

The boundary conditions that must be imposed on the in-plane components of the electric and magnetic fields are as follows, where the upper interface is at $z = +T$ and the lower interface is at $z = -T$:

$$\sum_i \left[H_{\mu}^{SOURCE,i} |_{z=+T} + H_{\mu}^{REFLECTED,i} |_{z=+T} \right] = \sum_i \left[H_{\mu}^{CRYSTAL,i} |_{z=+T} \right] \tag{3.12}$$

$$\sum_i \left[E_{\mu}^{SOURCE,i} |_{z=+T} + E_{\mu}^{REFLECTED,i} |_{z=+T} \right] = \sum_i \left[E_{\mu}^{CRYSTAL,i} |_{z=+T} \right] \tag{3.13}$$

$$\sum_i \left[H_{\mu}^{TRANSMITTED,i} |_{z=-T} \right] = \sum_i \left[H_{\mu}^{CRYSTAL,i} |_{z=-T} \right] \tag{3.14}$$

$$\sum_i \left[E_{\mu}^{TRANSMITTED,i} |_{z=-T} \right] = \sum_i \left[E_{\mu}^{CRYSTAL,i} |_{z=-T} \right] \tag{3.15}$$

The superscripts *source*, *reflected*, *transmitted*, and *crystal* will be abbreviated to S, R, T, and C respectively. To change these boundary conditions into a form that can

be programmed into a computer, the following Fourier expansions will be made:

$$\varepsilon^{-1}_{CRYSTAL} = |\underline{G}^k\rangle\langle\underline{G}^k|\varepsilon^{-1}_{CRYSTAL}\rangle \tag{3.16}$$

$$H^X_\alpha = |\underline{K}^i\rangle\langle\underline{K}^i|H^X_\alpha\rangle \tag{3.17}$$

$$E^X_\alpha = |\underline{K}^i\rangle\langle\underline{K}^i|E^X_\alpha\rangle \tag{3.18}$$

where the symbol X stands for either S, R, T, or C.

Now, even with these Fourier expansions, the boundary conditions above are not in a conveniently programmable form: somehow, the in-plane position dependence must be removed. This can be done by simply projecting both sides of each boundary condition equation onto a fixed Fourier basis vector $|\underline{K}^m\rangle$, which transforms, for example, the in-plane position-dependent term $\left|\underline{G}^k + \underline{K}^i\right\rangle$ into $\left\langle\underline{K}^m \mid \underline{G}^k + \underline{K}^i\right\rangle = \left\langle\underline{G}^m \mid \underline{G}^k + \underline{G}^i\right\rangle = \delta_{m,k+i} = \delta_{k,m-i}$, which is of course independent of both x and y.

To get a complete picture of what happens inside and outside a photonic crystal film when it is illuminated, one merely needs to solve for the set of amplitudes $\{w^i_{R,\mu}, w^i_{S,\mu}, w^i_{T,\mu}, b^j_+, b^j_-\}$.

Let us use from now on a total of N reciprocal lattice vectors in all of our truncated Fourier expansions. Then, since the matrix M will have dimensions $2N \times 2N$, there will be a total of $2N$ eigenvectors produced during the diagonalisation of M. Hence there will be $2N$ values of the index j, and N values of the index i. In order to make the enumeration of constraints and unknowns easier, I will arbitrarily partition each of the sets $\{b^j_+\}$ and $\{b^j_-\}$ into two halves, with the appended subscripts A and B. Hence the solution vector is now $\{w^i_{R,\mu}, w^i_{S,\mu}, w^i_{T,\mu}, b^j_{+A}, b^j_{+B}, b^j_{-A}, b^j_{-B}\}$, where the indices i and j both run from 1 to N.

This solution vector has a total length of $10N$, but during a practical calculation we would always specify the full set of incident amplitudes $\{w^i_{S,\mu}\}$ at the beginning. Hence $\{w^i_{S,\mu}\}$ can be removed from the set of unknowns, leaving a total of eight unknowns per reciprocal lattice vector. But there are two interfaces, each having four separate boundary conditions involving E_x, E_y, H_x, and H_y, making a total of eight linearly independent constraints per reciprocal lattice vector. Hence the number of independent constraints is equal to the number of unknowns, which ensures that unique and nontrivial solutions exist.

The set of $8N$ boundary conditions can be written in the form

$$Q_{k,l}U_l = Y_k \tag{3.19}$$

where U_l is the previously described vector of unknowns, and Y_k is a constant vector. This equation is shown below in a more detailed way:

$$[Q]\begin{pmatrix} w^i_{R_x} \\ w^i_{R_y} \\ w^i_{T_x} \\ w^i_{T_y} \\ b^{+,j}_A \\ b^{+,j}_B \\ b^{-,j}_A \\ b^{-,j}_B \end{pmatrix} = \begin{pmatrix} f^{m,i}_{E^{S+}_x} w^i_{S_x} \\ f^{m,i}_{E^{S+}_y} w^i_{S_y} \\ f^{m,i}_{H^{S+}_x} w^i_{S_x} \\ f^{m,i}_{H^{S+}_y} w^i_{S_y} \\ 0 \\ 0 \\ 0 \\ 0 \end{pmatrix}$$

where

$$[Q] = \begin{pmatrix} -f^{m,i}_{E^{R+}_x} & 0 & 0 & 0 & g^{1,m,j}_{E^+_x} & g^{2,m,j}_{E^+_x} & g^{3,m,j}_{E^+_x} & g^{4,m,j}_{E^+_x} \\ 0 & -f^{m,i}_{E^{R+}_y} & 0 & 0 & g^{1,m,j}_{E^+_y} & g^{2,m,j}_{E^+_y} & g^{3,m,j}_{E^+_y} & g^{4,m,j}_{E^+_y} \\ -f^{m,i}_{H^{R+}_x} & 0 & 0 & 0 & g^{1,m,j}_{H^+_x} & g^{2,m,j}_{H^+_x} & g^{3,m,j}_{H^+_x} & g^{4,m,j}_{H^+_x} \\ 0 & -f^{m,i}_{H^{R+}_y} & 0 & 0 & g^{1,m,j}_{H^+_y} & g^{2,m,j}_{H^+_y} & g^{3,m,j}_{H^+_y} & g^{4,m,j}_{H^+_y} \\ 0 & 0 & -f^{m,i}_{E^{T-}_x} & 0 & g^{1,m,j}_{E^-_x} & g^{2,m,j}_{E^-_x} & g^{3,m,j}_{E^-_x} & g^{4,m,j}_{E^-_x} \\ 0 & 0 & 0 & -f^{m,i}_{E^{T-}_y} & g^{1,m,j}_{E^-_y} & g^{2,m,j}_{E^-_y} & g^{3,m,j}_{E^-_y} & g^{4,m,j}_{E^-_y} \\ 0 & 0 & -f^{m,i}_{H^{T-}_x} & 0 & g^{1,m,j}_{H^-_x} & g^{2,m,j}_{H^-_x} & g^{3,m,j}_{H^-_x} & g^{4,m,j}_{H^-_x} \\ 0 & 0 & 0 & -f^{m,i}_{H^{T-}_y} & g^{1,m,j}_{H^-_y} & g^{2,m,j}_{H^-_y} & g^{3,m,j}_{H^-_y} & g^{4,m,j}_{H^-_y} \end{pmatrix}$$

in which the $g^{n,m,j}$ (where $n = 1, 2, 3, 4$) are matrices containing the Fourier coefficients of the Bloch modes, and where both $f^{m,i}$ and $g^{n,m,j}$ contain the in-plane wavevector components of the members of our truncated Fourier basis set. Note that the subscripts $+$ and $-$ on the elements of matrix $Q_{k,l}$ indicate the particular interface at which they are evaluated (i.e. $z = +T$ or $z = -T$ respectively). This linear matrix equation is directly soluble by inversion of the 'field-matching matrix' $Q_{k,l}$.

3.3 Overview of practical implementation

The practical details of the calculation of the transmission and reflection properties of a TFPC for any 3D angle of incidence will now be discussed. Since Maxwell's equations for linear media obey the law of superposition, it is convenient to make separate calculations for two orthogonal incident polarisation states, the solution vectors of which can be superposed to obtain the solution vector in the case of an arbitrary incident polarisation state, if necessary. Let these two orthogonal polarisation states

be TE and TM. In the TE case, the electric field vector is parallel to the (x, y) plane, and in the TM case, the magnetic field vector is parallel to the (x, y) plane. Hence $TE \leftrightarrow E_z = 0$ and $TM \leftrightarrow H_z = 0$. From Maxwell's equations, it is easy to show that $E_z = 0 \leftrightarrow (H_x, H_y) \propto (k_x, k_y)$ and $H_z = 0 \leftrightarrow (H_x, H_y) \propto (k_y, -k_x)$. These two polaristion states are indeed orthogonal because $\underline{H}_{3D}^{TE} \cdot \underline{H}_{3D}^{TM} \propto (k_x k_y - k_y k_x + 0) = 0$. Note that for exactly normal incidence (ie $k_\mu = 0$), the incident beam is both TE and TM, so we should use, for example, the orthogonal states $H_x = 0$ and $H_y = 0$ in this special case.

An outline of the steps involved in a typical calculation using a computer will now be given, in chronological order. The source-code of the program was written in Fortran 90.

1. Specify k_x, k_y, and k_o.
2. Specify the incident polarisation state (TE or TM) and set-up the source amplitudes $\{w_{S_x}^i\}$ and $\{w_{S_y}^i\}$ accordingly.
3. Specify the structural parameters of the photonic crystal film:
   (a) pitch of the lattice, Λ
   (b) hole diameter, D
   (c) film thickness, L
   (d) background refractive index of the film n_{film}
   (e) refractive index in the holes, n_a
4. Calculate the matrix elements $C_\mu^{ji}, \varepsilon^{ji}$, and the matrix elements corresponding to the function $\varepsilon^{-1}(x, y)$, $\overline{\varepsilon}^{ji}$. These matrix elements can be evaluated as described in Chapter 1 and stored in separate files.
5. Construct the bandstructure matrix M using the C_μ^{ji} and ε^{ji} elements already calculated.
6. Find the eigenvalues and eigenvectors of matrix M.
7. Specify the refractive indices of the regions above and below the photonic crystal film, n_{cov} and n_{sub}.
8. Construct the matrix Q using the eigenvalues and eigenvectors of M, and the matrix elements $\overline{\varepsilon}^{ji}$.
9. Construct the vector of knowns $\underline{Y}$ using the source amplitudes.
10. Solve for the vector of unknowns $\underline{U}$.

11. Calculate the z-components of the transmitted, reflected, and incident power flux density vectors.

12. Store the transmittance and reflectance (normalised to the z-component of the power flux density vector of the incident beam).

3.4 Results obtained by 'direct solution'

Since our calculation method relies on the truncation of Fourier series, it is important to ensure that we do not terminate the expansions too 'early', resulting in the loss of significant terms and therefore an unacceptable reduction in the accuracy of our calculations. Calculated transmission, reflection, and bandstructure plots generated using a total of 200 plane waves were compared with those made using 600 plane waves, and no significant difference between them was found, so we can conclude that a total of 200 plane waves (i.e. 100 plane waves per polarisation state) is a sufficient number.

Now that we have developed and implemented a method of rigorously calculating the behaviour of a TFPC under external illumination, we can find-out what effect periodic perforation has upon the optical characteristics of a thin high-index film. As an example, we shall consider a planar film having a refractive index $n_{film} = 3.46$ and a thickness $L = 240nm$, placed upon a semi-infinite substrate material of refractive index $n_{sub} = 1.6$. This structure is obtainable in practice by depositing unoxidised Al_xGaAs_{1-x} upon oxidised Al_yGaAs_{1-y}. The cover material will be air, so $n_{cov} = 1.0$. Without periodic patterning, the transmittance curve of this structure for TM-polarised incident light at the $Ti:Sapph$ wavelength $\lambda_o = 980nm$ is the dotted line in Figure 3.2. The horizontal axis of this graph is k_p/k, where k_p is the component of the incident wavevector parallel to the plane of the film, and k is the magnitude of the incident wavevector $\underline{k}$. This transmittance curve is very flat and featureless, as expected.

Let us now periodically pattern our imaginary film and see what happens. A periodic array of cylindrical holes will be etched into the film, each hole having a depth equal to the film thickness. Let the radius of every hole be $r = 56nm$, and let the holes be distributed such that their centres form a regular triangular array with pitch $\Lambda = 500nm$. From our collaboration with the University of Glasgow, we know that these parameters are comfortably within practical fabrication limits. A naive model for this structure might simply replace the patterned film with an unpatterned film having a lower index, to account for the presence of the holes. This would merely give a transmittance curve that is qualitatively similar to the dotted line in Figure 3.2.

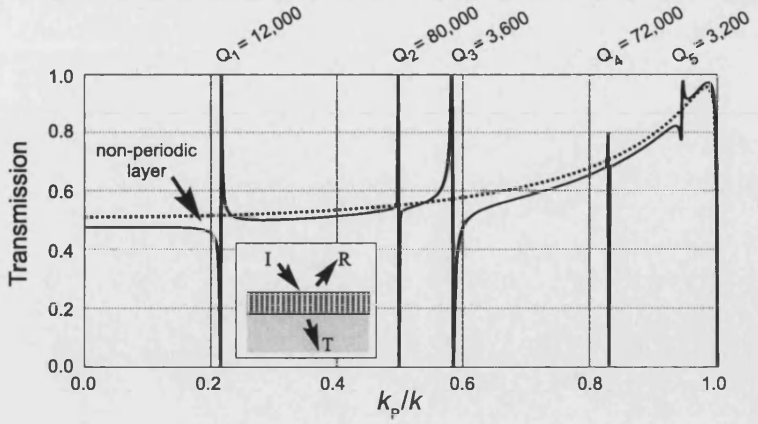

Figure 3.2: Normalised film transmittance before (dotted line) and after (solid line) periodic patterning, against in-plane wavevector. The curve is flat and featureless before patterning, but many sharp spikes appear after patterning.

However, this is utterly wrong: what actually happens to the transmittance curve when the holes are introduced is that several very sharp spikes appear at various values of k_p/k corresponding to several different out-of-plane angles of incidence (see the solid line in Figure 3.2). Note that, in this case, the in-plane angle of incidence has been fixed such that the in-plane wavevector component of the incident light is parallel to the $\Gamma - J$ crystallographic axis. These transmittance spikes are also very 'sharp' with respect to changes in the angular frequency of the incident beam, which implies that they correspond to very high Q-factor resonances, since $Q = \omega_o/\delta\omega$, where ω_o is the central angular frequency of the resonance and $\delta\omega$ is its FWHM. The resonances in Figure 3.2 are labeled with their Q-factors, two of which have Q-factors of the order of 10^5, which is very high indeed.

There are three things that are unusual about the resonances of a TFPC: their Q-factors may be very high, their 'line-shapes' are non-Lorentzian, and their fields may be concentrated either in the holes or in the solid material, or both.

Numbering the resonances in Figure 3.2 from 1 to 5, starting at the lowest angle of incidence, the microstructure of the electric field at resonance 1 is represented in Figure 3.3(a). This figure is a density plot of the electric field intensity for a cross-sectional slice through the film (with white indicating maximum intensity). The plane of the slice cuts through the centres of a line of holes, parallel to the $\Gamma - X$ crystallographic axis. The electric field of resonance 1 is concentrated in the solid parts of the film, whilst a similar plot (Figure 3.3(b)) shows that resonance 2 is strongly concentrated in the holes. This observation implies that it is possible to selectively excite either the solid or the gaseous parts of the perforated film. Possible applications of these 'dielectric resonances' and 'air resonances' will be discussed later. The shape of the transmittance

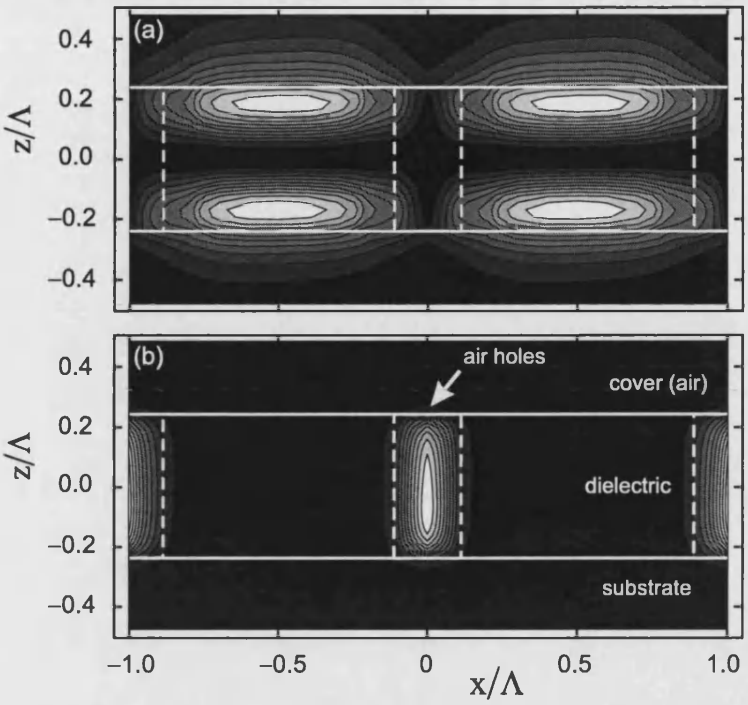

Figure 3.3: Electric field microstructure for (a) resonance 1 (upper diagram) and (b) resonance 2 (lower diagram).

curve in the neighbourhood of a TFPC resonance is consistently similar to that of an integral sign (or its mirror-image) rather than that of a Lorentzian function. However, the intensity curve of a resonant Bloch wave within the film does have the familiar Lorentzian form. Maximum or minimum transmittance can only be obtained by either positive or negative detuning from the central resonant frequency, as shown in Figure 3.4. This is unexpected, and will be explained later in this chapter. The locations of the high-Q resonances of a TFPC can be plotted in $(\underline{k}_p, \omega)$ space to form a set of three-dimensional dispersion surfaces, from which the in-plane group velocity of a resonance belonging to a particular dispersion surface can be determined by applying the equation

$$v_{\mu}^{group} = \frac{\partial \omega}{\partial k_{\mu}} \tag{3.20}$$

where μ is either of the in-plane coordinate axes, x or y. If we traverse an 'equi-frequency' path along such a dispersion surface then, since the frequency gradient will be zero along this path, the group velocity locally parallel to it must always be zero. Therefore, the in-plane group velocity of a resonance must be locally perpendicular to a constant-frequency slice through a resonance dispersion surface. An example of such a constant-frequency slice (for the parameter set mentioned earlier) is shown in Figure 3.5. The dotted hexagon marks the boundaries of the first Brillouin zone. In this diagram, the inner-most dispersion curve, which corresponds to resonance 1, is approximately

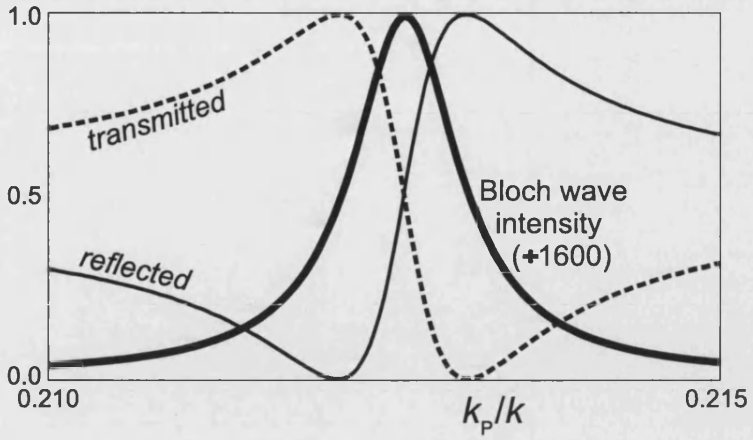

Figure 3.4: Calculated transmittance, reflectance, and total Bloch wave intensity in the neighbourhood of resonance 1

circular. Resonance 1 is therefore relatively isotropic, in the sense that its in-plane group velocity vector is roughly parallel to the in-plane direction of the incident beam for any in-plane angle of incidence. The starfish-shaped curve immediately beyond this, however, corresponds to a markedly anisotropic dielectric resonance. The resonant waves would, in this case, travel in a significantly different direction to that of the in-plane component of the wavevector of the incident beam, provided that one avoids the $\Gamma - J$ and $\Gamma - X$ directions, for which the incident in-plane wavevector and the in-plane group velocity of the resonant waves are parallel. This resonance could therefore be used to amplify the angular width of a composite beam (i.e. a beam composed of a finite or infinite number of plane-waves having different in-plane wavevectors), as will be discussed later. Note that in the dispersion diagram in Figure 3.5, there are certain isolated points along the resonance loci at which the coupling between an incident beam and the resonant state is nullified. At these 'null-coupling' points, light can pass through the film but it cannot excite a resonance. For example, resonance 1 has a null-coupling to a TE-polarised incident beam if it is directed along $\Gamma - J$. This null-coupling point is marked on the diagram as an open circle. Null-coupling points typically occur along the symmetry axes of the crystal, and the polarisation state of light leaking from a resonant state at a null-coupling point is either pure TE or TM. At all other points on the resonance loci, light leaving or coupling to a resonance is of mixed polarisation state.

There are many resonance loci in Figure 3.5, but in practical applications it may be advantageous to have fewer loci, along which the resonances would ideally have controllable Q-factors. The number of loci and the Q-factors of the resonances that exist along them are strongly dependent upon the parameters of the TFPC. Let the

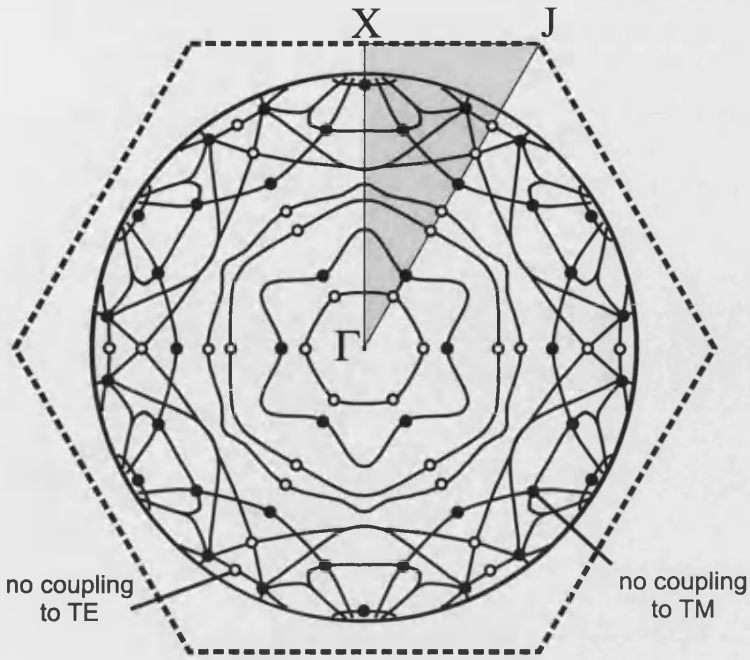

Figure 3.5: Wavevector diagram of the radiative resonant modes.

parameter set of our previous example TFPC structure be Π_1, where

$$\begin{aligned} \Pi_1 &= \{ \ \Lambda/nm, \ r/nm, \ L/nm, \ \lambda_o/nm, \ n_{cov}, \ n_{film}, \ n_{sub} \ \} \\ &= \{ \ 500, \ 56, \ 240, \ 980, \ 1.0, \ 3.46, \ 1.6 \ \} \end{aligned}$$

Then, for example, if parameter set Π_2 is the same as Π_1 except that the film thickess is only 15 nm, and Π_3 is the same as Π_1 except that the hole radius is 120nm, then parameter set Π_2 gives a single high-Q resonance ($Q = 200,000$) along $\Gamma - J$ (see Figure 3.6), whilst set Π_3 gives a single low-Q resonance ($Q = 120$) along this direction (see Figure 3.7). This demonstrates that it is possible to control the number of resonances, and their respective Q-factors, to match desired specifications. There are no obvious trends that can be exploited when designing a TFPC resonator for a particular application, but an 'iterative' approach can often yield a satisfactory set of parameters. This iteration process is viable because the calculations are fast enough to provide 'feedback' within a resonable length of time: a full transmittance curve can be generated using our DEC Alpha workstation in approximately 30 minutes.

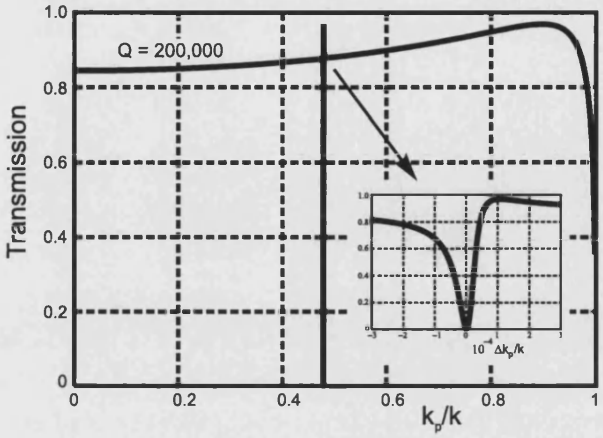

Figure 3.6: Transmittance of a structure that has a single high-Q resonance at 980nm.

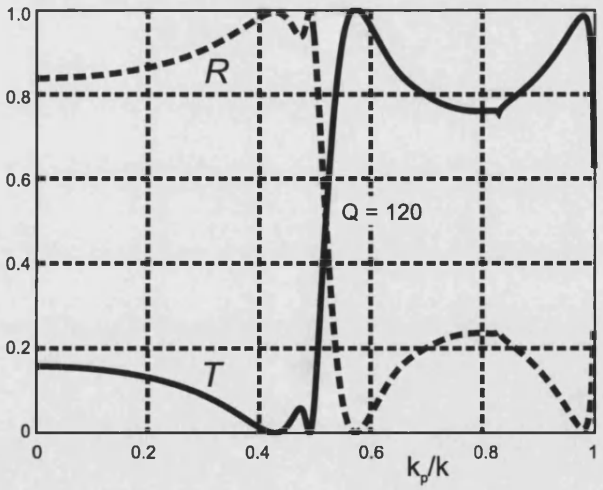

Figure 3.7: Transmittance (T) and reflectance (R) of a structure that has a single low-Q resonance at 980nm.

3.5 Explanation of the properties of TFPC resonances

In the previous section we found, by numerical calculations, that TFPCs can support an unusual type of resonance that breaks the traditional rules of resonances in thin layers. They have non-Lorentzian line-shapes, their fields can be strongly confined in the low-index parts of the film, and the Q-factors can be exceedingly high. Perhaps even more remarkably, a TFPC film that supports a multitude of high-Q resonances may be so thin that it would not even support a single low-Q resonance if its holes were filled-in.

We would like to understand why TFPC resonances have these unusual properties. Since we chose a modal method by which to perform our calculations, we have access to complete information on the Bloch wave composition of the resonances, and we can also readily obtain the plane-wave composition of each Bloch wave. By identifying which Bloch modes are involved in a typical high-Q resonance and then examining their individual plane-wave components, we hope to determine the mechanism whereby TFPCs can support high-Q air-resonances and dielectric-resonances. The non-Lorentzian line-shapes will then be explained with a simple 'toy model'.

3.5.1 Light confinement in a TFPC

A high Q-factor is indicative of strong light-confinement, which implies that there must be very little coupling between a TFPC resonance and radiative modes in the cover and substrate. We must explain why this is so.

A TFPC resonance consists of a superposition of Bloch modes and the most important of these modes will be those with purely real values of β, because all other modes will decay with time if the optical 'driving force' is removed. So it should be informative to plot a $(\underline{k}_p, \beta)$ bandstructure diagram of the crystal and label the most intense modes, for all five resonances in the case of our example structure (parameter set Π_1). This is shown in Figure 3.8, in which the position of each resonance along the in-plane wavevector axis is indicated with a vertical dotted line. Cutoff of the cover radiation modes occurs along the dotted quarter-circle. From this diagram, we can see that all five resonances consist of at least two significant z-propagating Bloch modes. This appears to be a general feature of all TFPC resonances, after trying many sets of parameters. Let us now concentrate on a particular resonance. The plane-wave spectrum of the most significant Bloch mode involved in resonance 1 is represented in Figure 3.9. This is an

in-plane wavevector diagram in which the termination point of the in-plane wavevector of each plane-wave component is indicated by a black dot. The hexagons are the tiled First Brillouin Zone boundaries, and the displacement vector of each black dot from the centre of its respective hexagon is shown as a black line. Beside each wavevector termination point, the percentage contribution of its corresponding plane-wave to the total intensity is marked. The shaded circles centred on the origin of wavevector space are the cutoff loci of the substrate and cover radiation modes. One can see from this diagram that most of the electromagnetic energy is carried by plane waves that lie beyond these cutoff loci and are therefore trapped within the film. In this case, a mere 0.01% of the total intensity is carried by the only component that can radiate. This is an example of 'quasi-guidance,' where confinement of light within the film is *almost* total, and it explains why TFPC resonances can have high Q-factors. Furthermore, since the plane-wave spectrum of each resonant Bloch mode consists of an infinite set of wavevectors, whose termination points form a space-filling lattice, the spatial frequencies of features in the field microstructure of a resonant mode may be so high that individual holes can be 'imaged'. This 'super-resolution' effect, the possiblility of which was suggested in Reference [16], explains why the resonances can be strongly concentrated in the holes. Figure 3.9 also illustrates another unusual property of optical Bloch waves: that of negative refraction [10]. The most intense pair of component rays, each of which carry 47.6% of the total intensity, point nominally in an opposite direction to that of the incident beam (labelled '0.01%').

3.5.2 Line-shapes of TFPC resonances

The fact that TFPC resonances generally involve at least two significant simultaneously resonant Bloch modes suggests a possible reason why the transmission curve of a TFPC in the immediate locality of a resonance is non-Lorentzian. In an ordinary unpatterned thin-film, there is always only one internal wave at resonance, which follows a zig-zag path as it bounces between the upper and lower interfaces. However, if it were somehow able to support more than one internal wave, then it seems likely that the interference between them would result in a non-Lorentzian line-shape.

To confirm this hypothesis, we need a simple 'toy model' that closely follows the traditional treatment of thin-film interference except that it must allow for more than one internal wave. We would like to be able to calculate the transmittance curve given the internal transmission coefficients of each internal wave, their β-values, and the thickness of the film. For this, it is necessary to introduce the concept of an optical scattering matrix. Scattering matrices will be used extensively in subsequent chapters, so our description of the 'toy model' will be preceded by a thorough discussion of the

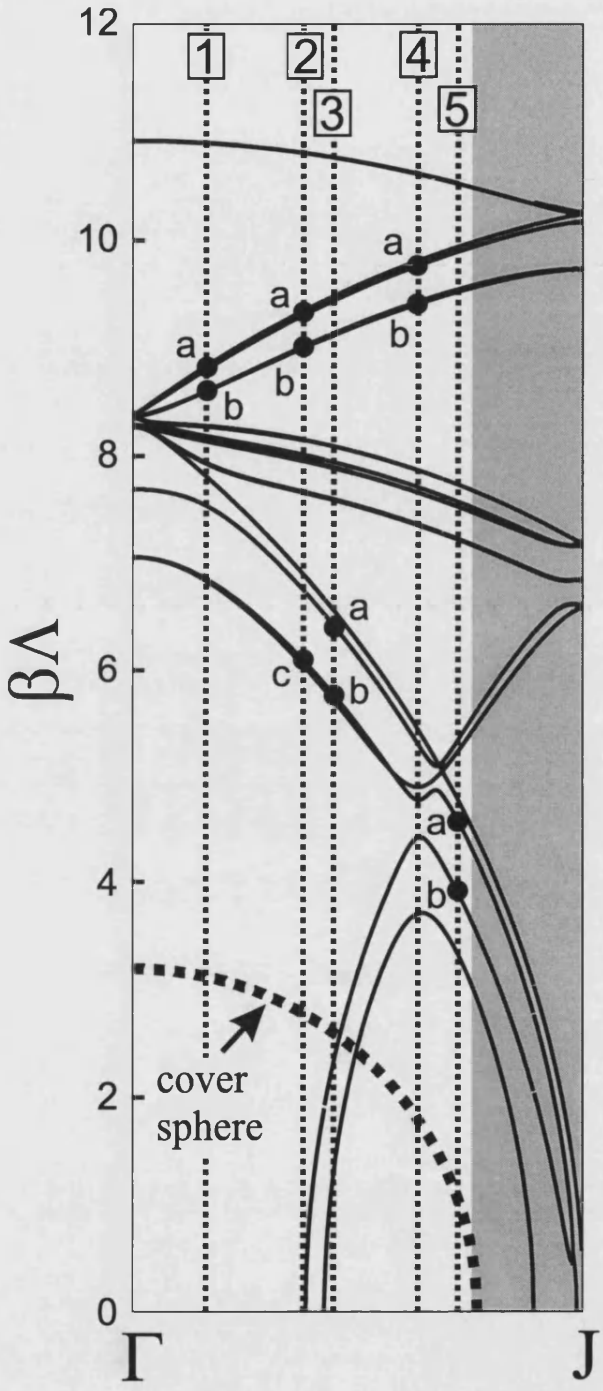

Figure 3.8: Calculated $\beta(\underline{k}_p)$ bandstructure (along the $\Gamma - J$ axis, and at 980nm) of the TFPC. The locations of the resonances are marked with dotted vertical lines.

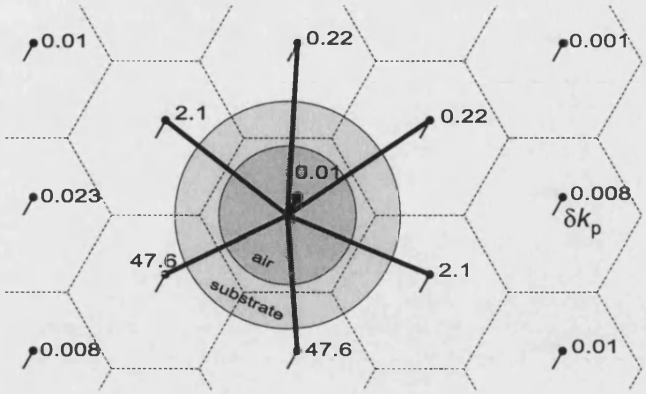

Figure 3.9: Plane-wave spectrum of the most significant Bloch mode for resonance 1.

definition of the scattering matrix and its properties.

The scattering matrix: definition and properties

A scattering matrix relates the amplitudes of waves that are incident upon an interface, or a composite structure consisting of more than one interface, to the amplitudes of the waves scattered away from it. There are many ways in which the 'input' and 'output' amplitude vectors can be arranged. For example, it is often convenient (as in later chapters) to define the scattering matrix $[S]$ to be such that

$$\begin{pmatrix} A_1^R \\ \vdots \\ A_N^R \\ A_1^T \\ \vdots \\ A_N^T \end{pmatrix} = \left(\begin{bmatrix} S_{11}^{++} & \cdots & S_{1N}^{++} \\ \vdots & \ddots & \vdots \\ S_{N1}^{++} & \cdots & S_{NN}^{++} \\ S_{11}^{-+} & \cdots & S_{1N}^{-+} \\ \vdots & \ddots & \vdots \\ S_{N1}^{-+} & \cdots & S_{NN}^{-+} \end{bmatrix} \begin{bmatrix} S_{11}^{+-} & \cdots & S_{1N}^{+-} \\ \vdots & \ddots & \vdots \\ S_{N1}^{+-} & \cdots & S_{NN}^{+-} \\ S_{11}^{--} & \cdots & S_{1N}^{--} \\ \vdots & \ddots & \vdots \\ S_{N1}^{--} & \cdots & S_{NN}^{--} \end{bmatrix} \right) \begin{pmatrix} A_1^U \\ \vdots \\ A_N^U \\ A_1^S \\ \vdots \\ A_N^S \end{pmatrix} \tag{3.21}$$

where A_i^R, A_j^T, A_k^U, and A_l^S are the amplitudes of the externally reflected, internally transmitted, internally incident, and externally incident rays respectively. We assume that there are N rays of each type, making a total of $4N$ rays (any of which are allowed to have zero amplitudes, so that one can have an unequal number of rays on either side of the interface if necessary). This equation can be represented more compactly as

$$\begin{pmatrix} \underline{A}^R \\ \underline{A}^T \end{pmatrix} = \begin{pmatrix} [S^{++}] & [S^{+-}] \\ [S^{-+}] & [S^{--}] \end{pmatrix} \begin{pmatrix} \underline{A}^U \\ \underline{A}^S \end{pmatrix} = [S] \begin{pmatrix} \underline{A}^U \\ \underline{A}^S \end{pmatrix} \tag{3.22}$$

The amplitude A in this case is typically chosen to be defined to be such that $E_\mu = A\exp(i(\underline{k}\cdot\underline{r}-\omega t))$ for any particular ray, where μ is x or y, in the case of TM or TE polarisation respectively.

The arrangement of the submatrices $[S^{++}]$,$[S^{+-}]$,$[S^{-+}]$, and $[S^{--}]$ in equation 3.22 is convenient in the sense that the upper and lower halves of the operand and result vectors both contain the amplitudes of upwards-travelling waves, and the lower halves of these vectors both refer to downwards-travelling waves. However, this submatrix configuration destroys a symmetry property that the scattering matrix $[S]$ can have if it is defined in a certain way. In order to make the matrix $[S]$ have this convenient symmetry, which will be apparent later, its submatrices will be re-arranged. In addition to this, we shall also re-define the amplitudes upon which these submatrices act. The symbol α will be used instead of A for amplitudes that conform to our new definition, and the new scattering matrix will be labeled $[\sigma]$ instead of $[S]$. This new scattering matrix $[\sigma]$ will be such that

$$\begin{pmatrix} \underline{\alpha}^R \\ \underline{\alpha}^T \end{pmatrix} = \begin{pmatrix} [\sigma^{+-}] & [\sigma^{++}] \\ [\sigma^{--}] & [\sigma^{-+}] \end{pmatrix} \begin{pmatrix} \underline{\alpha}^S \\ \underline{\alpha}^U \end{pmatrix} = [\sigma] \begin{pmatrix} \underline{\alpha}^S \\ \underline{\alpha}^U \end{pmatrix} \tag{3.23}$$

where the amplitude α_j of a particular ray is related to its corresponding amplitude under the old definition, A_j, as follows:

$$A_j = \left(+\sqrt{\frac{Z_j}{\cos(\theta_j)}} \right) \alpha_j \tag{3.24}$$

in which Z_j is the electromagnetic impedance encountered by the ray, which is equal to $\sqrt{(\mu_j/\varepsilon_j)} = \sqrt{(\mu_j)}/n_j$, and θ_j is the angle that it makes with the surface-normal.

To see why we have re-scaled the amplitudes in this way, consider the conservation equation for the time-averaged normal component of the power flux density vector, $J_z^{power} = \underline{E}^* \wedge \underline{H}$, for a planar interface. The conservation equation is

$$\sum_{i=1}^{N} |J_{z,i}^S| + \sum_{j=1}^{N} |J_{z,j}^U| = \sum_{k=1}^{N} |J_{z,k}^R| + \sum_{l=1}^{N} |J_{z,l}^T| \tag{3.25}$$

in which $J_{z,j} = (1/Z_j)\cos(\theta_j)A_j^* A_j$ for any particular ray, irrespective of its polarisation state. However, under our new amplitude definition, J_z^{power}, in any medium and for any polarisation state, is merely equal to the squared modulus of the amplitude:

$$J_{z,j} = \alpha_j^* \alpha_j \tag{3.26}$$

Therefore, under our new amplitude definition, equation 3.25 is simply

$$\underline{\alpha}^{S*} \cdot \underline{\alpha}^{S} + \underline{\alpha}^{U*} \cdot \underline{\alpha}^{U} = \underline{\alpha}^{R*} \cdot \underline{\alpha}^{R} + \underline{\alpha}^{T*} \cdot \underline{\alpha}^{T} \tag{3.27}$$

and if we define the vectors $\underline{u}$ and $\underline{v}$ to be such that

$$\underline{u} = \begin{pmatrix} u_1 \\ \vdots \\ u_N \\ u_{N+1} \\ \vdots \\ u_{2N} \end{pmatrix} = \begin{pmatrix} \alpha_1^S \\ \vdots \\ \alpha_N^S \\ \alpha_1^U \\ \vdots \\ \alpha_N^U \end{pmatrix} \quad and \quad \underline{v} = \begin{pmatrix} v_1 \\ \vdots \\ v_N \\ v_{N+1} \\ \vdots \\ v_{2N} \end{pmatrix} = \begin{pmatrix} \alpha_1^R \\ \vdots \\ \alpha_N^R \\ \alpha_1^T \\ \vdots \\ \alpha_N^T \end{pmatrix} \tag{3.28}$$

then we can write equation 3.27 in component form as follows, where summation over repeated indices is implicitly assumed in this and all subsequent expressions involving matrix elements and vector components in this section.

$$u_m^* u_m = v_i^* v_i \tag{3.29}$$

The input amplitudes will be chosen to be normalised such that $u_m^* u_m = \mathcal{N}$. Under this normalisation, equation 3.29 reduces to

$$v_i^* v_i = \mathcal{N} \tag{3.30}$$

Equation 3.23 can be written in component form as

$$v_i = \sigma_{ij} u_j \tag{3.31}$$

so equation 3.30 can be expressed in terms of the scattering matrix elements by substitution as follows:

$$v_i^* v_i = (\sigma_{ij} u_j)^* (\sigma_{ik} u_k) = \mathcal{N} \tag{3.32}$$

Rearrangement of this gives

$$(\sigma_{ij} u_j)^* (\sigma_{ik} u_k) = \sigma_{ji}^{T*} \sigma_{ik} u_k u_j^* = \mathcal{N} \tag{3.33}$$

where the superscript 'T' indicates the matrix transpose. If we let $\Upsilon_{jk} = \sigma_{ji}^{T*} \sigma_{ik}$ and $w_{kj} = u_k u_j^*$ then we have

$$\Upsilon_{jk} w_{kj} = \mathcal{N} \tag{3.34}$$

But from our normalisation condition, we know that $w_{kk} = \mathcal{N}$, which is equivalent to

$$\delta_{jk} w_{kj} = \mathcal{N} \tag{3.35}$$

By comparing equations 3.34 and 3.35, we can see that $\Upsilon_{jk} = \delta_{jk}$, since the matrix elements w_{lm} have arbitrary values. Therefore, $\sigma_{ji}^{T*}\sigma_{ik} = \delta_{jk}$, which is equivalent to the matrix equation

$$[\sigma]^{T*}[\sigma] = [I] \tag{3.36}$$

which states that $[\sigma]$ must be a unitary matrix. Any valid scattering matrix must satisfy this energy conservation condition, provided that the wave amplitudes are defined as described earlier and that its quadrants are arranged as shown above. Another condition that a scattering matrix must satisfy is that of time-reversal invariance. Merely interchanging and complex-conjugating the 'input' and 'output' wave amplitudes (u_j and v_i respectively) in the scattering equation

$$v_i = \sigma_{ij}u_j \tag{3.37}$$

must give the equation that describes the time-reversed scattering event [63]:

$$u_j^* = \sigma_{jk}v_k^* \tag{3.38}$$

The complex conjugation is required in order to change, for example, an amplitude phasor that leads another phasor into one that lags behind it instead. Substituting equation 3.38 into equation 3.37 gives

$$v_i = \sigma_{ij}\sigma_{jk}^*v_k. \tag{3.39}$$

But

$$v_i = \delta_{ik}v_k \tag{3.40}$$

from the definition of the δ tensor. Comparing equations 3.39 and 3.40 gives

$$\sigma_{ij}\sigma_{jk}^* = \delta_{ik} \tag{3.41}$$

which, in matrix form, is

$$[\sigma]^*[\sigma] = [I] \tag{3.42}$$

after complex-conjugating both sides. By comparing equations 3.36 and 3.42, one can also deduce that

$$[\sigma]^T = [\sigma] \tag{3.43}$$

which states that the scattering matrix must be symmetric. Equations 3.42 and 3.43 are important because they significantly reduce the number of independent scattering matrix elements.

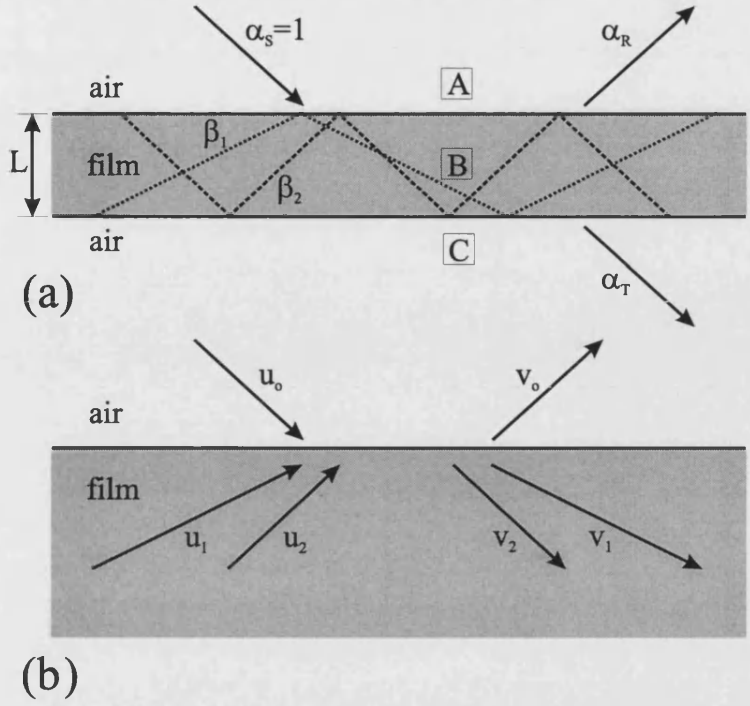

Figure 3.10: (a)A schematic illustration of the multiple-wave resonator model, showing the pair of 'zig-zag' resonant waves (having β values β_1 and β_2) and the incident, reflected, and transmitted rays. (b)The ray amplitudes at a single film/air interface. Four rays in the film are coupled to two rays in the air.

Multiple-wave resonator model

Consider a planar film illuminated by a single plane wave of unit amplitude. Let there be two internal waves and one external wave in the neighbourhood of both interfaces. The problem to be solved is shown schematically in Figure 3.10(a). Using our 'new' amplitude definition, the amplitude of the transmitted ray emerging from the film is $\sqrt{T}$ if the transmittance is T, and similarly for the reflectance, R. We know that there will only be one externally reflected beam and one externally transmitted beam because Figure 3.9 shows that we are working in a regime where there is only one wavevector inside the cutoff circles of the cover and substrate. For simplicity, let us set the cover and substrate indices to be equal to that of the vacuum. This structure is mirror-symmetric about the plane $z = L/2$, so the the scattering matrix of the A/B interface, σ_{AB}, will be related to the scattering matrix of the B/C interface, σ_{BC}, by a mere reversal of signs in the superscripts on their quadrants: $\sigma_{BC}^{++} = \sigma_{AB}^{--}$, $\sigma_{BC}^{+-} = \sigma_{AB}^{-+}$, $\sigma_{BC}^{-+} = \sigma_{AB}^{+-}$, and $\sigma_{BC}^{--} = \sigma_{AB}^{++}$. This mirror-symmetry also ensures that the 'total' scattering matrix of the film, σ_{AC}, is symmetric about its major and minor diagonals: $\sigma_{AC}^{--} = \sigma_{AC}^{++}$, and $\sigma_{AC}^{+-} = \sigma_{AC}^{-+}$. Substituting these relations into the multiple-scattering series-summation formulae described in the next chapter, we see that the two distinct

quadrants of the total scattering matrix σ_{AC} are given by

$$\sigma_{AC}^{++} = \sigma_{AB}^{++}\left[I - P\sigma_{AB}^{-+}P\sigma_{AB}^{-+}\right]^{-1}P\sigma_{AB}^{--} \tag{3.44}$$

$$\sigma_{AC}^{+-} = \sigma_{AB}^{+-} + \sigma_{AB}^{++}P\sigma_{AB}^{-+}\left[I - P\sigma_{AB}^{-+}P\sigma_{AB}^{-+}\right]^{-1}P\sigma_{AB}^{--} \tag{3.45}$$

Each scattering matrix in this case acts on the amplitudes of rays such as those shown in Figure 3.10(b). At each interface, two rays in the air are therefore coupled (via the scattering matrix elements) to four rays in the film. The propagation matrix P is required to account for the phase change of each ray in travelling from one interface to the other, and in this case it must be such that $P_{ij} = \delta_{ij}\exp(i|\beta_j L|)$. Since scattering matrices are symmetric (if suitably defined), $\sigma_{AB}^{++} = \sigma_{AB}^{--}$ and $\sigma_{AC}^{++} = \sigma_{AC}^{--}$. Also, the externally incident wave has unit amplitude, so $\sigma_{AC}^{--} = \sqrt{T}$ and $\sigma_{AC}^{+-} = \sqrt{R}$. Therefore, equations 3.44 and 3.45 are equivalent to

$$\sqrt{T} = \sigma_{AB}^{++}P\left[I - \left(\sigma_{AB}^{-+}P\right)^2\right]^{-1}\sigma_{AB}^{--} \tag{3.46}$$

$$\sqrt{R} = \sigma_{AB}^{+-} + \sigma_{AB}^{--}P\sigma_{AB}^{-+}P\left[I - \left(\sigma_{AB}^{-+}P\right)^2\right]^{-1}\sigma_{AB}^{--} \tag{3.47}$$

These equations express the transmittance T and reflectance R in terms of the propagation matrix P and the quadrants of the scattering matrix σ_{AB}, so all that remains to be done is to express σ_{AB} in terms of the internal transmission coefficients σ_{10} and σ_{20}. σ_{AB} (see Figure 3.10(b) for an illustration of the rays involved) is such that

$$\begin{pmatrix} v_0 \\ v_1 \\ v_2 \end{pmatrix} = \begin{pmatrix} \sigma_{00} & \sigma_{01} & \sigma_{02} \\ \sigma_{10} & \sigma_{11} & \sigma_{12} \\ \sigma_{20} & \sigma_{21} & \sigma_{22} \end{pmatrix}\begin{pmatrix} u_0 \\ u_1 \\ u_2 \end{pmatrix} = [\sigma_{AB}]\begin{pmatrix} u_0 \\ u_1 \\ u_2 \end{pmatrix} \tag{3.48}$$

But the scattering matrix σ_{AB} must be symmetric, and it must also satisfy the time-reversal invariance condition (equation 3.42). Therefore, assuming for simplicity that all of the scattering matrix elements are real-valued, which is true in the special case of a high-index film with symmetric low-index cladding:

$$\begin{pmatrix} \sigma_{00} & \sigma_{10} & \sigma_{20} \\ \sigma_{10} & \sigma_{11} & \sigma_{21} \\ \sigma_{20} & \sigma_{21} & \sigma_{22} \end{pmatrix}\begin{pmatrix} \sigma_{00} & \sigma_{10} & \sigma_{20} \\ \sigma_{10} & \sigma_{11} & \sigma_{21} \\ \sigma_{20} & \sigma_{21} & \sigma_{22} \end{pmatrix} = \begin{pmatrix} 1 & 0 & 0 \\ 0 & 1 & 0 \\ 0 & 0 & 1 \end{pmatrix} \tag{3.49}$$

This set of equations can be solved to obtain the values of the elements of the scattering matrix σ_{AB} in terms of the internal transmission coefficients σ_{10} and σ_{20}. Let the z-axis propagation constants of the two internal waves be β_1 and β_2 and let the thickness of the film be L. Then the various matrices that have to be substituted into equations

3.46 and 3.47 in order to solve for the transmittance and reflectance spectra are

$$[P] = \begin{pmatrix} \exp(i\beta_1 L) & 0 \\ 0 & \exp(i\beta_2 L) \end{pmatrix} \tag{3.50}$$

$$\sigma_{AB}^{+-} = \begin{pmatrix} \sigma_{00} \end{pmatrix}, \sigma_{AB}^{++} = \begin{pmatrix} \sigma_{10} & \sigma_{20} \end{pmatrix} \tag{3.51}$$

$$\sigma_{AB}^{--} = \begin{pmatrix} \sigma_{10} \\ \sigma_{20} \end{pmatrix}, \sigma_{AB}^{-+} = \begin{pmatrix} \sigma_{11} & \sigma_{21} \\ \sigma_{21} & \sigma_{22} \end{pmatrix} \tag{3.52}$$

We can now try a particular arbitrary set of parameters. Let $\sigma_{10} = 0.1$, $\sigma_{20} = 0.9$, $\beta_1 L = (1.5)\omega$, and $\beta_2 L = (1.0)\omega$, where ω is the angular frequency of the incident beam. In this situation, the two Bloch waves (numbered 1 and 2) have very different internal transmission coefficients: Bloch wave 1 is relatively weakly coupled to the cover and substrate radiation modes, since $\sigma_{10} = 0.1$, whilst Bloch wave 2 is strongly coupled: $\sigma_{20} = 0.9$. Therefore, Bloch wave 1 is fairly well confined within the film, and Bloch wave 2 is poorly confined. The inter-coupling between these high-Q and low-Q resonant modes (respectively) gives spectral transmittance and reflectance curves (see Figure 3.11), $T(\omega)$ and $R(\omega)$, that are very similar in shape to those generated by our complete model (see Figure 3.4) in the locality of resonance 1.

The total power flux (along the z-axis) carried by the Bloch waves, or 'Bloch wave intensity,' is proportional to $u_1^2 + u_2^2$, where

$$\begin{pmatrix} u_1 \\ u_2 \end{pmatrix}\Bigg|_{interfaceB/C} = \left[I - \left(\sigma_{AB}^{-+} P\right)^2\right]^{-1} \sigma_{AB}^{--} \tag{3.53}$$

The Bloch wave intensity, as defined above, is plotted in Figure 3.11 and it agrees well, qualitatively, with the Bloch wave intensity plot in Figure 3.4, which is for an actual TFPC resonance. The strong agreement between this 'toy model' and the calculated transmittance, reflectance, and Bloch wave intensity curves in the neighbourhood of a resonance of a 'real' TFPC, confirms that the unusual non-Lorentzian lineshape of a TFPC resonance is due to the presence of at least two simultaneously resonant Bloch waves, one having a high Q-factor and the other having a low Q-factor. The low-Q resonances provide the smoothly-varying background transmittance, the high-Q resonances produce the sharp spikes, and the coupling between them makes the spikes non-Lorentzian.

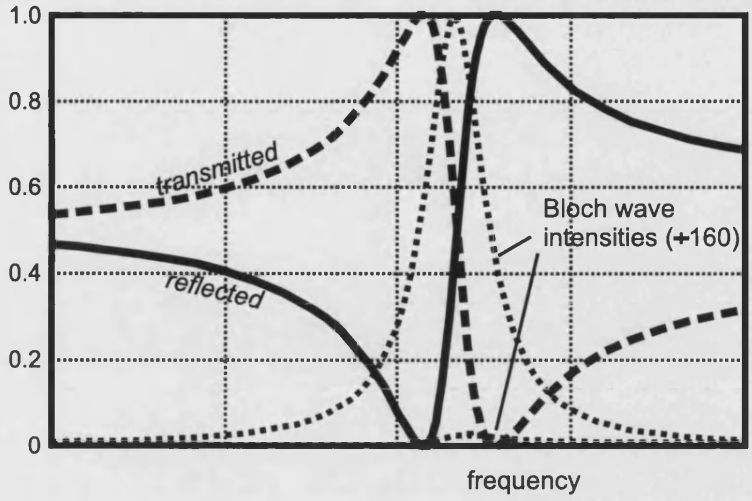

Figure 3.11: Transmittance, reflectance, and Bloch wave intensity in the neighbourhood of a resonance, according to our two-wave resonator 'toy model.'

3.6 Conclusions

In this chapter, a model for the optical characteristics of a TFPC under external illumination was devised, and implemented on a UNIX workstation. Using this model, we found that a TFPC can support an unusual class of high-Q resonance [1] that may be strongly confined within either the holes or the solid parts of the film. The properties of TFPC resonances were then explained by identifying the Bloch modes involved in a typical resonance and examining their plane-wave compositions.

TFPC resonators possess a host of possible applications. Indeed, they can be employed wherever a compact dispersive high-Q resonant cavity or a wavelength/angle-selective low-loss mirror is required. The conventional way of confining light in a thin film, as in the case of a semiconductor vertical cavity surface-emitting laser (VCSEL), is to place multilayer dielectric mirrors above and below it. The problem is that these multilayer mirrors occupy a lot of space and also have high electrical resistance, thus limiting the maximum attainable output power. A TFPC, however, can confine light without the aid of multilayer mirrors, which makes TFPCs an attractive alternative option when attempting to construct compact integrated semiconductor laser cavities (see Chapter 4). As another example, the high-Q air-resonances of a TFPC could be used as the basis of a very sensitive gas detector. Wavevector diagrams of TFPC resonances (for example, Figure 3.5) show that they can exhibit strong in-plane angular dispersion, a property that could be exploited to create miniature beam-steering components. Since the angular dispersion can be highly wavelength-dependent, WDM applications are also plausible (see Chapters 1, 5, and 6). Non-linear effect enhancement is also possible:

the combination of high cavity Q-factor and low in-plane group-velocity (for TFPC resonances close to the Γ-point in wavevector space) can greatly increase the strengths of field-material interactions, leading to the possibility of broad-band quasi-continuum generation and wavelength-conversion [45] in TFPC microstructures.

Chapter 4

Optical feedback in semiconductor VCSEL lasers by TFPC reflectors

4.1 Introduction

In this chapter, we investigate the feasibility of using 2D-TFPCs instead of distributed Bragg reflectors (DBRs, otherwise known as 'multilayer mirrors', 'multilayer stacks', or 'Bragg mirrors') for optical confinement in semiconductor vertical-cavity surface-emitting lasers (VCSELs) [51]. We assume that the problems of optical confinement and carrier confinement can be decoupled and therefore dealt-with separately. This is an assumption that is routinely made in the design of the more conventional DBR-VCSELs.

VCSELs, which have been in existence (in their present form) since 1979 [64], are interesting because, as their name suggests, they can be made to emit laser light from the top surface rather than from the side (as in the everyday edge-emitting semiconductor laser found in laser printers, bar-code scanners, and CD players). The top surface has a much larger area than the active portion of an end-face, so a VCSEL emits a comparatively broad beam that has a relatively low angular divergence, enabling efficient coupling into a conventional single-mode optical fibre placed directly above the device (which can be held in position by suitable packaging). Coupling light efficiently from an edge-emitting laser into a fibre is much less straightforward and may require expensive miniature lenses to be interposed between the laser and the fibre. Another advantage

of VCSELs is that, because they can be much more compact than edge-emitting lasers and can be fabricated in a small number of relatively inexpensive and easy steps, it is possible to produce, at low cost, very densely packed monolithic 2D arrays [65, 66] of individually-addressable VCSELs, each of which may have a different emission wavelength. These VCSEL arrays enable the use of many separate wavelength channels in WDM telecommunication systems.

Many groups have modelled moderately high-Q resonances localised at isolated point defects [60] in a TFPC possessing an in-plane bandgap, by means of the FDTD method. Point-defect resonances are, however, subject to the fundamental limitation that the emitted beam of light will have a high angular divergence, due to the strong localisation of the cavity field in the (x, y) plane, thus reducing the attainable output-coupling efficiency. In the type of TFPC-based VCSEL that we propose, the cavity field is essentially delocalised over the entire patterned area, whilst being quite strongly confined along the z axis, providing a significant reduction in the output-beam divergence compared to that of a point-defect cavity.

We shall begin with a very brief review of conventional semiconductor VCSELs. A good account of the fundamental physics involved is to be found in Reference [67]. The concepts involved are the same as those in the case of the edge-emitting semiconductor laser.

4.2 Operational principles of a semiconductor VCSEL

In a typical electrically-pumped semiconductor VCSEL laser (usable within the wavelength range 800-1000nm if it is composed of $Al_xGa_{1-x}As$ [68, 69, 70]), there is a thin semiconductor layer in which spontaneous and stimulated radiative recombination of electrons and holes takes place. The wavelength at which lasing occurs normally corresponds to a photon energy equal to the energy difference between the lowest conduction band level and the highest valence band level. The recombination ('active') layer is embedded in the centre of the intrinsic region of a forward-biased p-i-n junction, by the action of which electrons and holes are injected into it. Electrons are injected primarily from the n-type region, whilst holes are injected primarily from the p-type region. The material of the active layer (often InGaAs) is deliberately chosen to be such that the energy gap between its lowest conduction and highest valence band levels is less than that in the surrounding intrinsic region of the p-i-n junction, thus creating a potential well that traps the charge-carriers, providing high electron and hole densities and therefore a high probability of recombination, with a relatively low threshold current. If the forward-biasing potential difference is sufficiently high, then a population

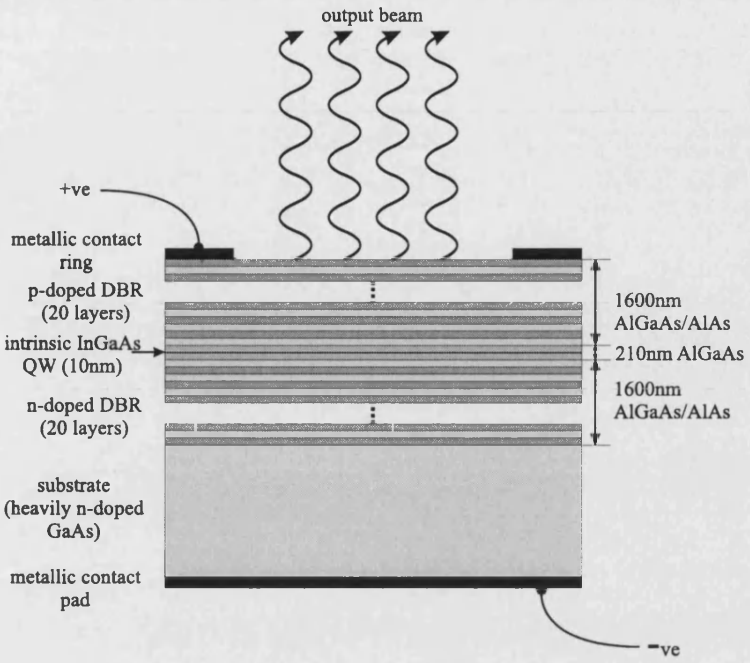

Figure 4.1: Schematic diagram of a conventional DBR-VCSEL employing an $Al_yGa_{1-y}As$ material set, emitting at a vacuum wavelength of 980nm (which is in the minimum-loss band of the materials). The active layer, in which stimulated and spontaneous recombination of electrons and holes takes place, is typically in the form of a thin quantum well (QW) or planar quantum dot (QD) array .

inversion can occur in the active layer, which makes stimulated radiative recombination processes possible, provided that the emitted photons are prevented from escaping for long enough so that they have time to trigger further recombination events. The emitted photons are usually confined by placing DBRs (each of which would typically consist of twenty unpatterned dielectric layers of alternating refractive index) above and below the active region, with the upper mirror forming the p-region of the p-i-n junction and the lower mirror forming the n-region. The operation of a VCSEL laser thus depends on the confinement of both charge-carriers and photons in the neighbourhood of the active layer. A schematic diagram of a conventional semiconductor DBR-VCSEL is shown in Figure 4.1.

4.2.1 Quantum wells

A particularly useful effect occurs when the active layer has a thickness that is of the order of the electron wavelength, e.g. 10nm, in which case it is called a 'quantum well' (QW) [71]. When the active layer is as thin as this, the electron energy levels within a band can no longer be approximated as a continuum. The electronic intra-band energy

levels are substantially discretised, and they depend on the precise thickness of the active layer, enabling emission wavelength tuning simply by varying the active layer thickness. Also, because the density of unwanted energy levels is greatly reduced, a smaller number of narrower spectral emission lines will be produced, thus improving the overall efficiency of the laser and lowering its threshold current. Another effect of using QWs instead of 'bulk' active layers is that the temperature-dependence of the gain is reduced, thus increasing the temperature-stability.

4.2.2 Quantum dots

Further improvement in overall efficiency, temperature stability, and threshold current can be obtained, in principle, by using arrays of quantum dots instead of quantum wells. These improvements are all attributable to the form of the electronic density-of-states function of a quantum dot (QD), which is similar to that of an individual atom in that it consists of delta-function spikes at particular energies. A quantum dot could be called an 'artificial atom' in the sense that its atom-like energy levels can be tailored, unlike those of a natural atom, enabling the output spectrum of a QD laser to be designed to suit a particular application to an even greater extent than that of a QW laser.

4.3 TFPCs versus DBRs

The reason why DBRs are used in semiconductor VCSELs is that it is generally thought that no other type of easily-fabricatable dielectric mirror can provide a high enough reflectivity. The reflectivity must indeed by very high ($\geq$ 99.5%) [51] because the nonzero-gain portion of the round-trip path length inside a VCSEL cavity is so short that a photon must make many round-trips, on average, before it can induce a radiative recombination event. Metallic mirrors cannot be employed because they are too lossy in terms of both reflectance and transmittance, the sum of which is of course not unity in this case due to the complex-valued refractive index.

Whilst it is nevertheless true that DBRs can provide sufficiently high reflectivities, there are several problems associated with them. All of these problems arise from the fact that a DBR is made of two different materials. The semiconductor materials constituting the layers of alternating refractive index in the DBR must be carefully lattice-matched to avoid strain-induced lattice dislocations (which would otherwise cause many atomic lattice defects to exist, thus greatly increasing the electrical resistance). This places a

tight constraint on the maximum refractive index contrast that can be achieved in the stack, thus necessitating a large number of layers to achieve the required reflectance. Since many layers are needed, each DBR must be quite tall (especially at long wavelengths, such as in the silica fibre minimum-loss band 1.3-1.5μm), and will therefore have a substantial electrical resistance, which will result in a large heating rate at high forward-bias voltages, which must be counteracted by an equal and opposite heat dissipation rate to avoid thermal device failure, typically introduced by means of metallic pins driven through the substrate and attached to cooling fins. This requirement for supplementary cooling at high bias voltages limits the optical power that a compact VCSEL can produce, because the thermal conduction pins and their associated hardware consume a lot of space, both horizontally and vertically. The purpose of this chapter is to convince the reader that all of these problems can be solved simultaneously by replacing DBRs with TFPCs.

Essentially, there are three possible options for the structure of a TFPC-based semiconductor VCSEL:

1. *A TFPC having a uniform background permittivity* (as discussed in Chapter 3). In this case, an array of quantum dots would be embedded within the film.

2. *A TFPC-coated unpatterned film* (i.e. a thin unpatterned high-index film with TFPC cladding layers placed above and below), which can be viewed as a single TFPC having an unpatterned planar defect (see Figure 4.2(a)). The TFPC layers would act as reflectors at certain internal angles of incidence, thus providing a certain degree of confinement within the unpatterned 'core,' which would contain at least one quantum well or at least one quantum dot array. This structure permits etch-damage sites to be kept well away from the active media, thereby eliminating possible problems with non-radiative recombination.

3. *A TFPC with non-uniform background permittivity* (non-constant along the z-axis) in which there is a definite 'core' region of higher background index than the adjacent patterned 'cladding' regions above and below it. This may also be regarded either as a multi-TFPC 'sandwich' with a patterned filling or a single TFPC with a patterned planar defect (see Figure 4.2(b)). A quantum dot array could be accommodated in the 'core' layer. The advantage of this structure is that it enables easier control over the number of quasi-guided core-modes at fixed frequency (see later).

Structure 3 would perhaps be easier to make than structure 2, since it may be produced by fully etching-through after a series of deposition processes rather than by alternating between etching and deposition. In all three options, the quantum dots or quantum

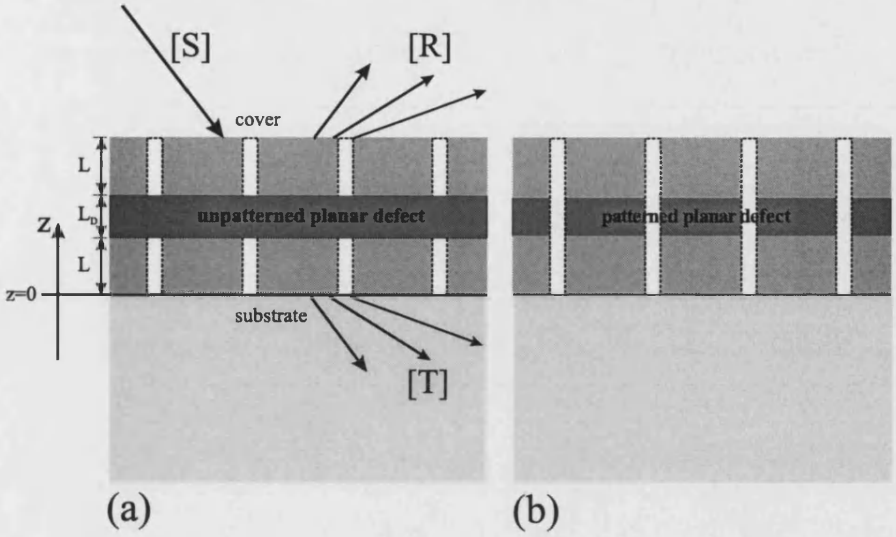

Figure 4.2: Unpatterned (a) and patterned (b) planar defects in a TFPC structure.

wells would be positioned such that maximum overlap with the field of the desired quasi-guided cavity mode is achieved. In this way, particular cavity modes can be preferentially selected.

We intend to model the optical confinement properties of the VCSEL cavity structures described above, so that a choice can be made between them. Before describing our calculation method and presenting a series of results, the design criteria for a semiconductor VCSEL will be briefly reviewed, preceded by some necessary definitions and background information. In the next three sections, we will make an estimate of the Q-factor of a typical DBR-VCSEL (to be used later), define the standard optical confinement factor Γ, and then derive a simple equation that connects the VCSEL threshold current with these two parameters Q and Γ.

4.4 Q-factor estimate for a DBR-VCSEL cavity

As stated earlier, the field intensity reflection coefficients at the effective cavity boundaries in a conventional semiconductor DBR-VCSEL must be typically 99.5% [51] (at a vacuum wavelength of 980nm) in order for lasing to occur at an acceptably small threshold current. For our present purposes, it would be convenient to translate this reflectance value into a cavity Q-factor, since the Q-factor can be more easily obtained from our model by measuring the width of the associated resonance feature on a spectral transmittance plot and applying the formula $Q_{cavity} = \omega_o/\Delta\omega$, where $\Delta\omega$ is the FWHM of the cavity field intensity as a function of angular frequency, which is approxi-

mately equal to the angular frequency separation between the transmittance maximum and minimum on either side of the central resonant angular frequency ω_o (see Figure 3.4).

Let the intensity (rather than amplitude) reflection coefficients of the upper and lower mirrors forming the resonant cavity be R_1 and R_2 respectively. The cavity field intensity after N cycles ('round-trips') will then be $I_o(R_1R_2)^N$, assuming that the cavity is at resonance and that the initial intensity is I_o. Therefore, the number of round-trips (each lasting a time $T_{cav} = mT$, where T_{cav} is the cavity round-trip time, T is the optical period $2\pi/\omega_o$, and m is the effective cavity mode order) required for the cavity field intensity to decay to $1/e$ times its initial value will be $N_d = (\ln((R_1R_2)^{-1}))^{-1}$, which gives an estimated cavity resonance lifetime $\tau = N_d mT = 2\pi m(\omega_o \ln((R_1R_2)^{-1}))^{-1}$. However, assuming an exponential decay of the cavity field amplitude of the form $A = A_o \exp(-\gamma t)\exp(i\omega_o t)$ gives a resonance lifetime $\tau = (2\gamma)^{-1}$. Equating this resonance lifetime with the previous resonance lifetime gives the required decay rate $\gamma = (\omega_o/4\pi m)\ln((R_1R_2)^{-1})$.

The cavity Q-factor (as defined by $Q = \omega_o/\Delta\omega$) can be obtained from this decay rate by one more step: taking the Fourier transform $A(\omega)$ of the cavity field amplitude function $A(t)$. This will be done next, after a brief diversion. Consider the excitation of a resonant cavity mode at frequency ω_o by a light source of constant intensity. When the light source is 'switched on' at time $-t_{on}$, the cavity field amplitude envelope will build-up from zero, asymptotically approaching a saturation value A_{sat} in a similar way to that of a capacitor being charged. For as long as the source is 'on', the cavity field amplitude envelope will increase with time according to $A_{sat}(1-\exp(-\kappa(t+t_{on}))$, but when it is 'switched off' at time $t_{off} = 0$ exponential decay of the envelope function will begin according to $A_{sat}\exp(-\gamma t)$. If we let t_{on} tend to ∞ then the Fourier transform $A(\omega)$ of the cavity field amplitude-versus-time curve $A(t)$ becomes proportional to

$$\begin{aligned}\int_{-\infty}^{0} A_{sat}\exp(i\omega_o t)\exp(-i\omega t)dt + \int_{0}^{\infty} A_{sat}\exp[[i(\omega_o-\omega)-\gamma]t]dt \\ = A_1\delta(\omega-\omega_o) + A_2(i(\omega-\omega_o)+\gamma)^{-1} \\ \propto A(\omega) \qquad (4.1)\end{aligned}$$

so that

$$I(\omega) = A^*(\omega)A(\omega) \propto \frac{1}{\gamma^2+(\omega-\omega_o)^2} \qquad (4.2)$$

for $\omega \neq \omega_o$ (in order to avoid the δ-function spike). This function gives the shape of the spectral intensity curve contribution due to the imperfect confinement of the cavity field, which is Lorentzian in form and is symmetric about the line $\omega = \omega_o$. Perfect confinement would leave only the δ-function term in equation 4.1. The FWHM of the Lorentzian spectral intensity distribution above is 2γ, and this fact, together with the

previously derived expression for the decay rate γ, can be used to obtain the following expression for the cavity Q-factor:

$$Q = \frac{\omega_o}{\Delta\omega} = \frac{\omega_o}{2\gamma} = \omega_o \tau = \frac{2\pi m}{\ln\left(\frac{1}{R_1 R_2}\right)} \tag{4.3}$$

In practice, a typical effective cavity length in a conventional semiconductor VCSEL operating at 980nm is $1.5\mu m$ [51] (for an $Al_xGa_{1-x}As$ material set). The corresponding effective cavity mode order m can be evaluated by $m = 2L_{cav}n_{cav}/\lambda_o$ in which λ_o is the vacuum wavelength and n_{cav} is the cavity index (typically 3.4 for an $Al_xGa_{1-x}As$ structure). By this, we obtain an m-value of 10.2, implying the existence of approximately ten field intensity lobes within the effective cavity length, superimposed upon the roughly Gaussian envelope function of the intensity as a function of z. Given that the minimum reflectances of the cavity mirrors are both 99.5%, equation 4.3 yields the following cavity Q-factor for a typical DBR-VCSEL operating at a vacuum wavelength of 980nm:

$$Q^{DBR} = \frac{2\pi 10.2}{\ln\left(\frac{1}{(0.995)^2}\right)} \approx 6400, \tag{4.4}$$

with a corresponding resonance lifetime $\tau^{DBR} = \lambda_o Q_{min}/(2\pi c) = 3ps$.

4.5 The optical confinement factor, Γ

Suppose that the envelope function of the cavity field intensity at resonance is approximately Gaussian in form with respect to the z-coordinate, with FWHM equal to L_{field}, as follows:

$$I(z) = A^*(z)A(z) = I_o exp[(-2(z - z_o)/L_{field})^2] \tag{4.5}$$

where z_o is the z-coordinate of the centre of the active region. The optical confinement factor Γ is defined [71] to be the normalised overlap integral of the cavity field intensity with the active region, and it provides a measure of the extent of spatial confinement of the cavity field along the z-axis. Let the active region have thickness L_{active}. Transforming to coordinates such that $Z = z - z_o$, we have:

$$\Gamma = \frac{\langle A(Z) \mid F(Z) \mid A(Z) \rangle}{\langle A(Z) \mid A(Z) \rangle} \tag{4.6}$$

where the 'top-hat' function $F = F(Z)$ is such that $F = 1$ if $|Z| \leq L_{active}/2$ but is otherwise equal to 0. Therefore,

$$\Gamma = \frac{\int_{-L_{active}/2}^{L_{active}/2} I(Z)dZ}{\int_{-\infty}^{\infty} I(Z)dZ} \tag{4.7}$$

By a standard integral the denominator is

$$\int_{-\infty}^{\infty} I_o \exp((-2Z/L_{field})^2) dZ = I_o \sqrt{\pi} L_{field}/2, \tag{4.8}$$

and since the active region is much smaller than the FWHM (L_{field}) of the cavity field, the numerator is approximately equal to $I_o L_{active}$. The optical confinement factor Γ is, consequently,

$$\Gamma = \frac{2 I_o L_{active}}{I_o \sqrt{\pi} L_{field}} \approx \frac{L_{active}}{L_{field}}. \tag{4.9}$$

For simplicity, we have ignored any high-spatial-frequency oscillations that may be present in the cavity field intensity, because these oscillations depend on the cavity mode order. Provided that the active region is positioned at an antinode, this approximation nevertheless gives a reliable measure of the spatial confinement. For a typical DBR-VCSEL, the reciprocal of the optical confinement factor, $1/\Gamma$, is

$$\frac{1}{\Gamma^{DBR}} = \frac{L_{field}}{L_{active}} = \frac{1500nm}{10nm} = 150 \tag{4.10}$$

using the effective cavity length from the previous section and a typical QW width/QD diameter of 10nm.

It should be noted that if a QD array is employed instead of a QW, then the optical confinement factor will be multiplied by the fraction of the area in the (x, y) plane occupied by the quantum dots. In this chapter, we are merely interested in comparing the relative performance of DBR-VCSELs and TFPC-VCSELs, so, since this reduction in the optical confinement factor will be common to both cavity types, it will be ignored. The attainable gain coefficient for a QD array is actually much higher than that for a QW, because of the form of its electronic density-of-states function, so the threshold current can still be acceptably small. In the next section, we will discuss the relationship between threshold current, Q, and Γ.

4.6 The relationship between threshold current, Q, and Γ

The relation between threshold current density J_{th}, Q, and Γ can be determined by combining a simple lasing threshold condition [51] for a VCSEL laser with the standard empirical expression [71] for the dependence of the gain coefficient g on the charge current density J. The threshold condition, which describes the fine balance between the round-trip loss and gain required in order to be on the threshold of lasing, is

$$R_1 R_2 \exp(2 g L_{active} - 2\alpha L_{field}) = 1 \tag{4.11}$$

where g is the gain coefficient and α is the material loss coefficient. Rearranging the threshold condition gives

$$\left(\frac{1}{2L_{field}}\right)\ln\left(\frac{1}{R_1R_2}\right) = g\left(\frac{L_{active}}{L_{field}}\right) - \alpha. \tag{4.12}$$

Hence, at threshold,

$$g\Gamma = \alpha + \frac{1}{2L_{field}}\ln\left(\frac{1}{R_1R_2}\right) \tag{4.13}$$

The standard empirical equation for the dependence of the gain coefficient on the charge current density is

$$g = \beta J_o \ln(J/J_o), \tag{4.14}$$

where β is a known constant for a particular quantum well or quantum dot, and J_o is the 'transparency current density' [71], the current density at which gain begins. From section 4.4,

$$Q = \frac{2\pi m}{\ln(\frac{1}{R_1R_2})}, m = \frac{2L_{field}n_{cav}}{\lambda_o}. \tag{4.15}$$

Therefore, by equating Equations 4.13 and 4.14, and eliminating R_1R_2 using Equation 4.15,

$$J_{th} = J_o \exp\left[\left(\frac{\alpha}{\Gamma} + \frac{2\pi n_{cav}}{\Gamma Q \lambda_o}\right)\frac{1}{\beta J_o}\right]. \tag{4.16}$$

The first term in the rounded brackets in this equation is a loss-related term, whilst the second is gain-related. The loss-related term can be decreased by increasing Γ, because of the resulting decrease in the overlap integral of the optical field with the inactive material, whilst the gain-related term can be decreased by increasing the value of the product ΓQ, which implies that a deficiency in the cavity Q-factor can be compensated by an excess in Γ. Therefore, if a particular TFPC-VCSEL is found to have a comparatively low Q but nevertheless has a relatively high Γ then it may still be useful in practice, i.e. it may still have a sufficiently low threshold current. This will be discussed further in the next sections, in conjunction with other considerations that affect the usefulness of a practical VCSEL.

4.7 Performance requirements for a VCSEL

The three major performance requirements are:

1. Low threshold current I_{th}. The sum of the two terms in the argument of the threshold current equation in the previous section (see Equation 4.16) must be minimised as far as possible, whilst simultaneously satisfying all other design

constraints. For the attainment of a low threshold current, the carrier confinement condition described later must also be satisfied.

2. High gradient of the output-power characteristic curve (against excess forward current beyond theshold). This is proportional to the differential quantum efficiency η_D defined in the next section.

3. High maximum attainable output power P_{max}. This requires a low device resistance Z, so that the thermal dissipation rate increases 'slowly' with increasing current, thus lowering the onset of thermal breakdown.

4.8 Optical design criteria

There are two main optical parameters that need to be controlled in the design of a semiconductor VCSEL laser: the cavity Q-factor and the optical confinement factor Γ.

The gradient of the P-I characteristic curve beyond threshold (i.e. $\partial P/\partial(I - I_{th})$), where P is the optical output-power, is approximately equal to $(h\nu/e)\eta_D$ [72] where η_D is the differential quantum efficiency. The equation connecting the differential quantum efficiency [51] η_D with the cavity Q-factor is, ignoring the internal quantum efficiency,

$$\eta_d = \frac{1}{\left(1 + \left(\frac{Q\alpha\lambda_o}{2\pi n_{cav}}\right)\right)}, \tag{4.17}$$

where Equation 4.15 has been used to eliminate the product R_1R_2. This pseudo-reciprocal dependence on the Q-factor is to be expected, since a high Q implies a low optical energy extraction rate. This dependence also indicates a potential conflict between the requirements of low threshold current and high η_D, which can however be resolved by having a sufficiently high optical confinement factor. Much higher optical confinement factors can be attained in a TFPC-VCSEL compared with a DBR-VCSEL. This will be shown later.

It would be helpful, when comparing the performance of TFPC-VCSELs against DBR-VCSELs, to have a single parameter that is a clear indicator of the threshold current. The threshold current density equation given above (see Equation 4.16) can be re-written using the previously-stated expression for the dependence of the differential quantum efficiency on the Q-factor as follows:

$$J = J_o \exp[(\alpha/\beta J_o)S] \tag{4.18}$$

where we have defined the non-standard parameter S such that

$$S = \frac{1}{\Gamma}\left(1 + (\eta_D^{-1} - 1)^{-1}\right). \tag{4.19}$$

This parameter will be named the 'S-factor'. For a VCSEL to have a low threshold current, the S-factor should be as low as possible. Increasing the optical confinement factor decreases the S-factor, and so does decreasing the differential quantum efficiency. However, the situation is complicated by the fact that we need a high differential quantum efficiency in order to have a high output power, so the S-factor cannot be too low. A compromise is therefore necessary. Adopting a typical value for the material loss coefficient α of $20cm^{-1}$, and assuming that the effective index of the cavity mode is the same as the background value (typically 3.4) yields a differential quantum efficiency η_D of approximately 0.63 for a standard DBR-VCSEL. Taking the effective cavity length of the VCSEL to be 1500nm as before, and supposing that the QW width is 10nm, gives the following value for the S-factor:

$$S^{DBR} = \frac{1500nm}{10nm}\left(1 + (0.63^{-1} - 1)^{-1}\right) \quad = \quad 405. \tag{4.20}$$

By comparing the 'S-factor' of a TFPC-VCSEL structure with the value given above, one can determine whether its threshold current will be higher or lower than that of a typical DBR-VCSEL, on the assumption that all of the quantities α, β, and J_o remain unchanged by the introduction of periodic patterning. The actual value of the threshold current, of course, depends on the parameters β and J_o but our aim here is to merely compare the threshold currents associated with various cavity designs in a way that does not depend, as far as possible, upon the physical structure or chemical composition of the active media.

4.9 Electronic design criteria

The main electronic (as opposed to optical) design criterion is that, for obtaining a low threshold current, the charge-barriers must be sufficiently 'high' and 'wide' to confine electrons and holes in the neighbourhood of the active media, ensuring strong coupling between the carriers and the optical field. The barrier potential 'height' is determined by the difference in the electronic bandgap widths between the active material and the barrier material, which is a constant for a particular set of materials. For a given material set, the barrier width w must be greater than a minimum value w_{min}. A typical value of w_{min} for practical $Al_xGa_{1-x}As$ structures is $100nm$. It is also important that there should be no etch-damage sites (such as those produced at the hole boundaries during the patterning process) within a radius equal to $w_{min} + r_{QD}$ of the centre of a

quantum dot or within a distance $w_{min} + L_{QW}/2$ of the central plane of a quantum well, where r_{QD} is the quantum dot radius and L_{QW} is the quantum well thickness. The reason for this is that non-radiative recombination of electrons and holes can occur at etch-damage sites, and the presence of a significant number of these may raise the threshold current density to or beyond a value that would result in the destruction of the device.

A VCSEL cavity based on either a single-film TFPC or a TFPC with a patterned defect layer can only be used in conjunction with quantum dot arrays because an embedded QW would intersect the etch-damage sites surrounding the holes. In these cavities, the minimum barrier width condition $w \geq w_{min}$ imposes constraints on the lattice pitch Λ, hole radius r, and TFPC layer thickness L. If, for example, each quantum dot is embedded so that it is equidistant from the centres of its neighbouring holes and also half-way between the upper and lower interfaces then in order for the condition $w \geq w_{min}$ to be satisfied, a circle of radius $w_{min}+r_{QD}$ concentric with each quantum dot of radius r_{QD} must not intersect any interfaces. The following pair of conditions must therefore be satisfied simultaneously: $\Lambda \geq 2(r + w_{min} + r_{QD})$, $L \geq 2(w_{min} + r_{QD})$. Typically, r_{QD} is approximately 5nm, and $w_{min} + r_{QD}$ may be taken to be around 100nm. Therefore, $\Lambda \geq 2(r + 100nm)$ and $L \geq 200nm$. Hence, if for example, $\Lambda = 400nm$ then $r \leq 100nm$. Fortunately, this is compatible with the parameter regime in which we have been working (i.e. in the intra-passband regime). TFPCs having in-plane bandgaps would however be excluded by this constraint on the hole radius, since for these the hole diameter must be a large fraction of the lattice pitch. These particular structural parameter constraints apply to the case in which the fundamental (i.e. single-lobed) quasi-guided dielectric mode is employed, giving a large field intensity overlap integral with the centrally-positioned quantum dots. If higher-order dielectric modes, such as the double-lobed mode in Figure 3.3(a) were used then different (but similar) conditions would apply.

For a TFPC cavity containing an unpatterned defect layer, the carrier-confinement constraints are not so restrictive in the sense that any combination of hole radius and lattice pitch is acceptable. Either QWs or QD arrays can be incorporated in the unpatterned defect layer, and the condition $w \geq w_{min}$ is satisfied if merely $L \geq 2(w_{min}+l)$ is satisfield, where l is either the half-thickness h_{QW} of a QW or r_{QD} (which normally have similar values in practice).

Another electronic design criterion concerns the device resistance. The total electrical resistance Z of the resonant cavity structure, ignoring that of the substrate and the terminal pads, must be low enough so that a high maximum optical power output is possible. The optical power output is limited by the thermal energy production rate $P_{thermal} = ZI$, where I is the product of the current density and the in-plane

device area. Beyond a particular heating rate, irreversible thermal device failure will occur. The maximum optical power can be raised by externally-imposed cooling, as mentioned earlier, but this would make the VCSEL much less compact, so we will reject this option. It can also be raised by decreasing the device thickness. Let us define the device thickness L_{tot} to be the sum of the thickness of the planar defect layer and the thicknesses of all of the mirror layers. An estimate of the reduction ratio of the device resistance Z of a given VCSEL compared to a typical DBR-VCSEL is given by the ratio of the device thicknesses. We will therefore define a device-resistance reduction factor Y such that $Y = L_{tot}^{DBR}/L_{tot}$.

Typically, each DBR in a DBR-VCSEL has 20 quarter-wave layers, each of thickness around 80nm, making a total DBR height of 1600nm. The unpatterned defect layer, including the QW or QD array, would have a thickness of approximately 210nm. Therefore, the total thickness L_{tot}^{DBR}, of the two DBRs and the defect layer, would be approximately 3410nm.

4.10 Summary of the optical and electronic design criteria

Our full set of design criteria, of which two are optical and two are electronic, will now be stated:

$$J_{th} \leq J_{th}^{DBR} \iff S \leq 405 \tag{4.21}$$

$$\partial P/\partial(I - I_{th}) \geq (\partial P/\partial(I - I_{th}))^{DBR} \iff \eta_D \geq 0.63 \tag{4.22}$$

$$P_{max} \geq P_{max}^{DBR} \iff Y \geq 1 \tag{4.23}$$

$$sufficient\ \ carrier\ \ confinement \iff w \geq 100nm. \tag{4.24}$$

The last two design criteria, involving the 'Y-factor' and the barrier width w, are independent of both each other and the first two, whereas the first two are coupled together as shown in Figure 4.3. Figure 4.3 shows the variation of the S-factor with the differential quantum efficiency η_D for a range of different values of $1/\Gamma$. The area of (S, η_D) space in which the first two design criteria are satisfied is shaded. This area is entirely contained within the limits of the horizontal and vertical axes.

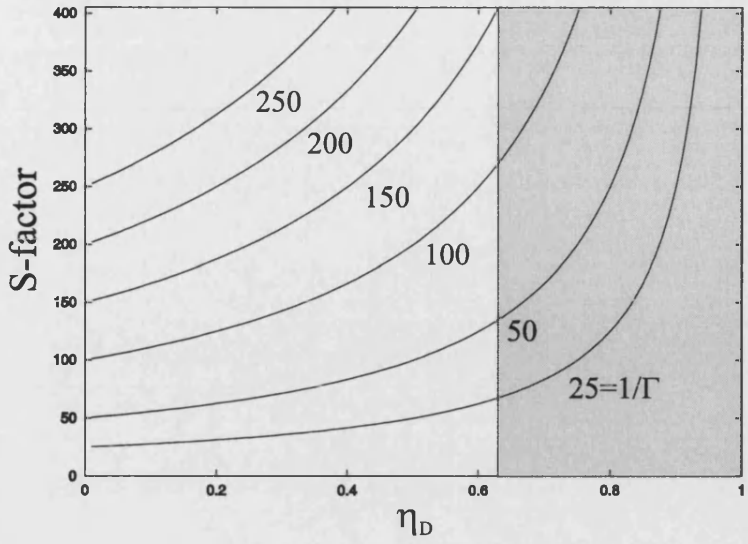

Figure 4.3: S-factor against differential quantum efficiency η_D for various values of $1/\Gamma$. The region in which the first two design criteria are satisfied is shaded. The S-factor is a non-standard parameter defined in Section 4.8.

4.11 Method for modelling optical confinement in multiple-film TFPC-VCSEL cavities

Having presented the design criteria, our modelling method will now be explained. For modelling TFPC-VCSEL structures containing patterned and unpatterned planar defects, the 'direct method' used in the previous chapter is not suitable, because the 'field-matching matrix' quadruples in area with each additional interface, making the computation time unacceptably long for a multi-TFPC structure. Instead, an 'indirect method' must be applied to the case of the VCSEL cavity, and for the implementation of this it is first necessary to consider the imposition of boundary conditions at a single interface before proceeding to the general case in which there are multiple interfaces. In 'indirect methods', the sizes of the matrices involved in the boundary condition equations remain constant, irrespective of the number of interfaces, wherein lies their advantage.

4.11.1 Boundary conditions at a single photonic crystal interface

Let the field vector $\underline{F}$ be either $\underline{E}$ or $\underline{H}$, and let $\nu = x, y$. Then the boundary conditions on the in-plane $\underline{E}$ and $\underline{H}$ fields at the planar interface $z = 0$ that separates the 'crystal'

and the 'cover' regions, which are patterned and unpatterned respectively, are:

$$F_\nu^{CRYSTAL}\Big|_{z=0} = F_\nu^{COVER}\Big|_{z=0}. \tag{4.25}$$

If we define the matrix elements f^{ijk} to be such that

$$F_a = \sum_{ijk} f_a^{ijk} \exp(i(\underline{K}^i \cdot \underline{r} + K_z^{jk} z - \omega t)) \tag{4.26}$$

where $a = x, y, z$ and the superscript k indicates the polarisation state and the out-of-plane direction (of free propagation or decaying propagation) of each ray, then

$$F_a|_{z=0} = \sum_{ijk} f_a^{ijk} \exp(i(\underline{K}^i \cdot \underline{r} - \omega t)) = \sum_m \left(\exp(i(\underline{K}^m \cdot \underline{r})) \sum_{jk} f_a^{mjk} \exp(-i\omega t) \right). \tag{4.27}$$

But, from the definition of a Fourier series expansion,

$$F_a|_{z=0} = \sum_m (|\underline{K}^m\rangle \langle \underline{K}^m \mid F_a\rangle|_{z=0}) = \sum_m (\exp(i(\underline{K}^m \cdot \underline{r})) \langle \underline{K}^m \mid F_a\rangle|_{z=0}). \tag{4.28}$$

Therefore, by comparing Equations 4.27 and 4.28,

$$\langle \underline{K}^m \mid F_a\rangle|_{z=0} = \sum_{jk} f_a^{mjk} \exp(-i\omega t). \tag{4.29}$$

Now if we project both sides of Equation 4.25 onto the fixed Fourier basis vector $|\underline{K}^m\rangle$, in order to remove the positional dependence, then we obtain

$$\langle \underline{K}^m \mid F_\nu^{CRYSTAL}\rangle|_{z=0} = \langle \underline{K}^m \mid F_\nu^{COVER}\rangle|_{z=0}. \tag{4.30}$$

Equation 4.29 enables this to be written as

$$\sum_{jk} f_{\nu,CRYSTAL}^{mjk} = \sum_{jk} f_{\nu,COVER}^{mjk}, \tag{4.31}$$

where the time-dependence $\exp(-i\omega t)$ cancels from both sides. Equation 4.31 is equivalent to the original boundary condition equation (Equation 4.25), and it can be transformed to a more convenient form by separating-out the amplitudes A^{jk} of the in-plane magnetic field components such that

$$f_a^{mjk} = \eta_{F_a}^{mjk} A^{jk}, \tag{4.32}$$

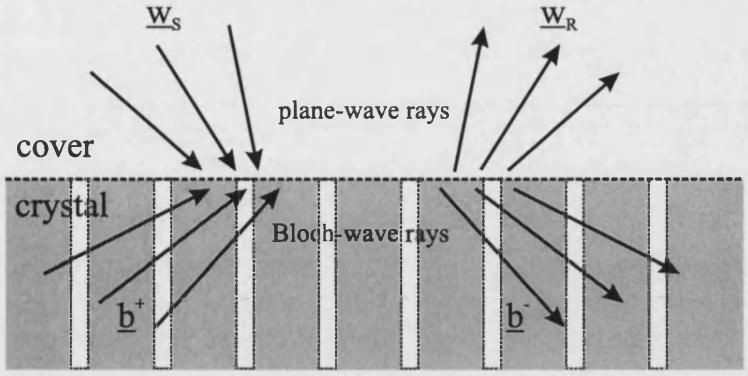

Figure 4.4: A schematic diagram of waves in the locality of a single planar interface between a photonic crystal and an unpatterned medium. Note that the interface is perpendicular to the axis of continuous translational invariance of the 2D grating.

where

$$A^{jk}_{CRYSTAL} = \begin{cases} b^j_{+A} & if \quad k=0 \\ b^j_{+B} & if \quad k=1 \\ b^j_{-A} & if \quad k=2 \\ b^j_{-B} & if \quad k=3 \end{cases} \quad and \quad A^{jk}_{COVER} = \begin{cases} w^j_{Rx} & if \quad k=0 \\ w^j_{Ry} & if \quad k=1 \\ w^j_{Sx} & if \quad k=2 \\ w^j_{Sy} & if \quad k=3 \end{cases} . \tag{4.33}$$

Equation 4.31 can now be written as

$$\sum_{jk} \eta^{mjk}_{F^{CRYSTAL}_{\nu}} A^{jk}_{CRYSTAL} = \sum_{jk} \eta^{mjk}_{F^{COVER}_{\nu}} A^{jk}_{COVER} \tag{4.34}$$

which, in matrix form, is

$$\begin{bmatrix} \eta^{mj0}_{E^1_x} & \eta^{mj1}_{E^1_x} & \eta^{mj2}_{E^1_x} & \eta^{mj3}_{E^1_x} \\ \eta^{mj0}_{E^1_y} & \eta^{mj1}_{E^1_y} & \eta^{mj2}_{E^1_y} & \eta^{mj3}_{E^1_y} \\ \eta^{mj0}_{H^1_x} & \eta^{mj1}_{H^1_x} & \eta^{mj2}_{H^1_x} & \eta^{mj3}_{H^1_x} \\ \eta^{mj0}_{H^1_y} & \eta^{mj1}_{H^1_y} & \eta^{mj2}_{H^1_y} & \eta^{mj3}_{H^1_y} \end{bmatrix} \begin{bmatrix} b^j_{+A} \\ b^j_{+B} \\ b^j_{-A} \\ b^j_{-B} \end{bmatrix} = \begin{bmatrix} \eta^{mj0}_{E^2_x} & \eta^{mj1}_{E^2_x} & \eta^{mj2}_{E^2_x} & \eta^{mj3}_{E^2_x} \\ \eta^{mj0}_{E^2_y} & \eta^{mj1}_{E^2_y} & \eta^{mj2}_{E^2_y} & \eta^{mj3}_{E^2_y} \\ \eta^{mj0}_{H^2_x} & \eta^{mj1}_{H^2_x} & \eta^{mj2}_{H^2_x} & \eta^{mj3}_{H^2_x} \\ \eta^{mj0}_{H^2_y} & \eta^{mj1}_{H^2_y} & \eta^{mj2}_{H^2_y} & \eta^{mj3}_{H^2_y} \end{bmatrix} \begin{bmatrix} w^j_{Rx} \\ w^j_{Ry} \\ w^j_{Sx} \\ w^j_{Sy} \end{bmatrix} \tag{4.35}$$

where the labels 'crystal' and 'cover' have been replaced by '1' and '2' respectively. This matrix equation neatly expresses all of the required boundary conditions in the situation illustrated in Figure 4.4. We will now show how the matrix elements $\eta^{ijk}_{F_a}$ can be calculated. Let us begin with the case of the crystal region (i.e. $z \leq 0$). The values of the matrix elements $\eta^{ijk}_{H^1_\nu}$ can be derived directly from the eigenvectors B^{iJ}_ν of the bandstructure matrix (see Chapter 2), where $J = 1, \ldots, 2N$ and $j = 1, \ldots, N$, in which N is the number of elements retained in our truncated set of Fourier basis vectors, as follows:

$$\eta^{ijk}_{H^1_\nu} = \begin{cases} B^{ij}_\nu & if \quad k=0 \quad or \quad 2 \\ B^{i(j+N)}_\nu & if \quad k=1 \quad or \quad 3 \end{cases} \tag{4.36}$$

and the values of the matrix elements K_z^{jk} can be obtained from the square-roots of their corresponding eigenvalues $(\beta^J)^2$:

$$K_z^{jk} = \begin{cases} +\beta^j & if \;\; k = 0 \\ +\beta^{(j+N)} & if \;\; k = 1 \\ -\beta^j & if \;\; k = 2 \\ -\beta^{(j+N)} & if \;\; k = 3 \end{cases} \tag{4.37}$$

For any individual Fourier component, $\underline{\nabla} = i\underline{K}_{3D}$. But $\underline{\nabla} \cdot \underline{H} = 0$, from Maxwell's equations, so $\underline{K}_{3D}^{ijk} \cdot \underline{h}^{ijk} = 0$, which implies that $h_z^{ijk} = -[K_x^i h_x^{ijk} + K_y^i h_y^{ijk}]/[K_z^{jk}]$. Also, from Equation 4.32, $h_a^{ijk} = \eta_{H_a}^{ijk} A^{jk}$. Therefore, the matrix elements $\eta_{H_z}^{ijk}$ can be expressed in terms of $\eta_{H_\nu}^{ijk}$ and K_z^{jk} as follows:

$$\eta_{H_z}^{ijk} = -\left[\frac{K_x^i}{K_z^{jk}}\eta_{H_x}^{ijk} + \frac{K_y^i}{K_z^{jk}}\eta_{H_y}^{ijk}\right] \tag{4.38}$$

Again, for any Fourier component, $\partial_t = -i\omega$. But $\underline{\nabla} \wedge \underline{H} = \partial_t \underline{D}$, from another Maxwell equation, so $i\underline{K}_{3D}^{ijk} \wedge \underline{h}^{ijk} = -i\omega\varepsilon\underline{e}^{ijk}$, which implies that $\underline{e}^{ijk} = -(\omega\varepsilon)^{-1}\underline{K}_{3D}^{ijk} \wedge \underline{h}^{ijk}$. Therefore,

$$\begin{bmatrix} e_x^{ijk} \\ e_y^{ijk} \\ e_z^{ijk} \end{bmatrix} = \varepsilon^{-1}(x,y)\frac{1}{\omega}\begin{bmatrix} -K_y^i h_z^{ijk} & + & K_z^{jk} h_y^{ijk} \\ +K_x^i h_z^{ijk} & - & K_z^{jk} h_x^{ijk} \\ -K_x^i h_y^{ijk} & + & K_y^i h_x^{ijk} \end{bmatrix} \tag{4.39}$$

Expressions for $\eta_{E_a}^{ijk}$ can now be derived, bearing in mind that in order to reconstruct the function $\varepsilon^{-1}(x,y)$ in Equation 4.39, one must use its corresponding Fourier expansion coefficients $\overline{\varepsilon}_l$, which are such that

$$\varepsilon^{-1}(x,y) = \sum_l \overline{\varepsilon}_l \exp(i\underline{G}^l \cdot \underline{r}) \tag{4.40}$$

As an example, consider $\eta_{E_x}^{ijk}$. For this, we must first project E_x onto a fixed Fourier basis vector $|\,\underline{K}^m\rangle$, where the integration is over a unit cell of area $\mathcal{A}$:

$$\begin{aligned} \langle \underline{K}^m \mid E_x \rangle &= \mathcal{A}^{-1} \int\int dxdy E_x \exp(-i\underline{K}^m \cdot \underline{r}) \\ &= \mathcal{A}^{-1} \int\int dxdy \sum_{ijk} e_x^{ijk} \exp(i(\underline{K}^i \cdot \underline{r} - \underline{K}^m \cdot \underline{r} + K_z^{jk} z - \omega t)) \end{aligned} \tag{4.41}$$

But, from Equations 4.39 and 4.40,

$$e_x^{ijk} = \omega^{-1}\left[-K_y^i h_z^{ijk} + K_z^{jk} h_y^{ijk}\right] \sum_l \overline{\varepsilon}_l \exp(i\underline{G}^l \cdot \underline{r}) \tag{4.42}$$

Substituting this into Equation 4.41, setting z to 0, and using the fact that

$$\mathcal{A}^{-1}\int\int dxdy\exp(i(\underline{G}^l+\underline{G}^i-\underline{G}^m)\cdot\underline{r})=\delta_{\underline{G}^m,\underline{G}^l+\underline{G}^i}=\delta_{\underline{G}^l,\underline{G}^m-\underline{G}^i} \tag{4.43}$$

gives

$$\langle\underline{K}^m\mid E_x\rangle|_{z=0}=\omega^{-1}\sum_{ijk}\left[\overline{\varepsilon}^{mi}\left[-K_y^ih_z^{ijk}+K_z^{jk}h_y^{ijk}\right]\exp(-i\omega t)\right] \tag{4.44}$$

where $\overline{\varepsilon}^{mi}=\overline{\varepsilon}(\underline{G}^m-\underline{G}^i)$ (see Chapter 3).

Also, from Equations 4.29 and 4.32,

$$\langle\underline{K}^m\mid E_x\rangle|_{z=0}=\sum_{jk}\eta_{E_x}^{mjk}A^{jk}\exp(-i\omega t) \tag{4.45}$$

By comparing Equations 4.44 and 4.45, one can see that

$$\eta_{E_x}^{mjk}A^{jk}=\frac{1}{\omega}\sum_i\left[\overline{\varepsilon}^{mi}\left[-K_y^ih_z^{ijk}+K_z^{jk}h_y^{ijk}\right]\right] \tag{4.46}$$

However, from Equation 4.32, $h_z^{ijk}=\eta_{H_z}^{ijk}A^{jk}$ and $h_y^{ijk}=\eta_{H_y}^{ijk}A^{jk}$. Therefore,

$$\eta_{E_x}^{mjk}=\frac{1}{\omega}\sum_i\left[\overline{\varepsilon}^{mi}\left[-K_y^i\eta_{H_z}^{ijk}+K_z^{jk}\eta_{H_y}^{ijk}\right]\right] \tag{4.47}$$

Similarly,

$$\eta_{E_y}^{mjk}=\frac{1}{\omega}\sum_i\left[\overline{\varepsilon}^{mi}\left[K_x^i\eta_{H_z}^{ijk}-K_z^{jk}\eta_{H_x}^{ijk}\right]\right] \tag{4.48}$$

$$\eta_{E_z}^{mjk}=\frac{1}{\omega}\sum_i\left[\overline{\varepsilon}^{mi}\left[-K_x^i\eta_{H_z}^{ijk}+K_y^i\eta_{H_x}^{ijk}\right]\right] \tag{4.49}$$

We have now given expressions for all of the matrix elements on the LHS of Equation 4.35. The elements of the matrix on the RHS of Equation 4.35 are simpler, because the electric permittivity of the cover medium is independent of position. In this case, $\overline{\varepsilon}^{mi}$ is merely equal to the diagonal matrix $(1/\varepsilon_{cover})\delta^{mi}$. The eigenmodes of the cover medium are individual plane waves rather than Bloch modes, which implies that $\eta_{H_x^2}^{ijk}$ and $\eta_{H_y^2}^{ijk}$ are also diagonal matrices.

Let us define the following vectors, in which there are N Fourier basis vectors per

polarisation state:

$$\underline{w}^R = \begin{pmatrix} w^1_{Rx} \\ \vdots \\ w^N_{Rx} \\ w^1_{Ry} \\ \vdots \\ w^N_{Ry} \end{pmatrix}, \quad \underline{w}^S = \begin{pmatrix} w^1_{Sx} \\ \vdots \\ w^N_{Sx} \\ w^1_{Sy} \\ \vdots \\ w^N_{Sy} \end{pmatrix}, \quad \underline{b}^+ = \begin{pmatrix} b^1_{+A} \\ \vdots \\ b^N_{+A} \\ b^1_{+B} \\ \vdots \\ b^N_{+B} \end{pmatrix}, \quad \underline{b}^- = \begin{pmatrix} b^1_{-A} \\ \vdots \\ b^N_{-A} \\ b^1_{-B} \\ \vdots \\ b^N_{-B} \end{pmatrix} \tag{4.50}$$

In terms of these vectors, the boundary condition matrix equation (4.35) can be written more compactly as

$$[M_2] \begin{pmatrix} \underline{w}^R \\ \underline{w}^S \end{pmatrix} = [M_1] \begin{pmatrix} \underline{b}^+ \\ \underline{b}^- \end{pmatrix} \tag{4.51}$$

Multiplication of both sides of this equation from the left by the matrix inverse of $[M_2]$ gives

$$\begin{pmatrix} \underline{w}^R \\ \underline{w}^S \end{pmatrix} = [M_2]^{-1} [M_1] \begin{pmatrix} \underline{b}^+ \\ \underline{b}^- \end{pmatrix} \tag{4.52}$$

The matrix on the RHS of this equation transforms the set of ray amplitudes in the medium immediately below the interface (which is the photonic crystal in this case) to those in the medium immediately above it (which is unpatterned). This matrix, $[M_2]^{-1}[M_1]$, must therefore be the so-called 'transfer matrix' of the interface. If we now re-label this transfer matrix as '$[T]$,' then one can re-express equation 4.52 in terms of the four quadrants of the transfer matrix in the following way:

$$\begin{pmatrix} \underline{w}^R \\ \underline{w}^S \end{pmatrix} = \begin{pmatrix} [T^{++}] & [T^{+-}] \\ [T^{-+}] & [T^{--}] \end{pmatrix} \begin{pmatrix} \underline{b}^+ \\ \underline{b}^- \end{pmatrix} \tag{4.53}$$

In practice, however, it would be much more convenient if the amplitudes of the rays scattered away from the interface ($\underline{w}^R$ and $\underline{b}^-$) were on the same side of the equation, with the amplitudes of the incident rays ($\underline{w}^S$ and $\underline{b}^+$) on the opposite side. In other words, we would prefer a scattering matrix rather than a transfer matrix. Scattering matrices were discussed briefly in Chapter 3. Fortunately, a transfer matrix can be transformed into a scattering matrix by a set of matrix operations on its quadrants as described below.

From equation 4.53,

$$\underline{w}^S = [T^{-+}]\, \underline{b}^+ + [T^{--}]\, \underline{b}^- \tag{4.54}$$

Therefore,

$$[\underline{b}^-] = [T^{--}]^{-1} \left(\underline{w}^S - [T^{-+}]\, \underline{b}^+ \right) \tag{4.55}$$

But, from equation 4.53,

$$\underline{w}^R = [T^{++}]\,\underline{b}^+ + [T^{+-}]\,\underline{b}^- \tag{4.56}$$

Substituting the RHS of equation 4.55 in place of the '$\underline{b}^-$' term in equation 4.56 gives

$$\underline{w}^R = [T^{++}]\,\underline{b}^+ + [T^{+-}]\left([T^{--}]^{-1}\left(\underline{w}^S - [T^{-+}]\,\underline{b}^+\right)\right) \tag{4.57}$$

Equation 4.57 expresses $\underline{w}^R$ in terms of $\underline{b}^+$ and $\underline{w}^S$, whilst equation 4.55 expresses $\underline{b}^-$ in terms of $\underline{b}^+$ and $\underline{w}^S$. These two equations can therefore be written as a single matrix equation, as shown below:

$$\begin{pmatrix} \underline{w}^R \\ \underline{b}^- \end{pmatrix} = \begin{pmatrix} \left([T^{++}] - [T^{+-}][T^{--}]^{-1}[T^{-+}]\right) & \left([T^{+-}][T^{--}]^{-1}\right) \\ \left(-[T^{--}]^{-1}[T^{-+}]\right) & \left([T^{--}]^{-1}\right) \end{pmatrix} \begin{pmatrix} \underline{b}^+ \\ \underline{w}^S \end{pmatrix} \tag{4.58}$$

The matrix in this equation is the scattering matrix of the interface, $[S]$, the quadrants of which are enclosed in rounded brackets. Given the quadrants of the scattering matrix ($[S^{++}]$, $[S^{+-}]$, $[S^{-+}]$, and $[S^{--}]$), one can solve for the amplitudes of the transmitted and reflected rays for any given set of incident rays.

At this point, we know how to calculate the scattering matrix of a planar interface between a photonic crystal and an unpatterned medium, and it would be possible to use this scattering matrix on its own to deal with the case in which a semi-infinite photonic crystal is illuminated from an adjacent semi-infinite unpatterned medium. However, of course, the scattering matrix of a given interface is not changed by the presence of other interfaces, either above or below it, so we merely need some way of combining scattering matrices of individual interfaces to obtain the 'total' scattering matrix of even a very elaborate multi-TFPC structure. There are several ways of doing this, two of which are described in the next section.

4.11.2 Scattering matrix of a series of photonic crystal interfaces

When dealing with more than one interface, it is essential to be able to take account of the phase changes in the rays as they propagate between adjacent interfaces. For this purpose, we define a 'propagation matrix' $[P]$ such that $P_{ij} = \delta_{ij}\exp(i\beta_j l)$, where l is the change in z-coordinate that a ray experiences (in time) in going between the interfaces, and β_j is the z-momentum of a particular Fourier component ray. Of course, the matrix $[P]$ can be reduced to size $2N \times 2N$ rather than $4N \times 4N$, because an upwards-going ray has a positive value of l and positive β_j, whilst an otherwise equivalent downwards-going ray has a negative l and negative β_j, which undergoes the same phase change since the phase angle is equal to the product of β_j and l.

It is possible merely to concatenate a series of transfer and propagation matrices to obtain the transfer matrix of a structure having many interfaces, and the resultant 'total' transfer matrix can be transformed to a scattering matrix. Convenient as this may seem, this approach suffers from numerical instabilities caused by the Bloch modes that are evanescent along the z-axis. Combining the scattering matrices of adjacent individual interfaces by the summation of infinite multiple-scattering series is much more stable, as concluded in References [17] and [73]. The multiple-scattering-series summation equations [17] are listed below.

$$[S^{++}] = [S_2^{++}]\Big[[I] - [P][S_1^{+-}][P][S_2^{-+}]\Big]^{-1}[P][S_1^{++}] \quad (4.59)$$

$$[S^{+-}] = [S_2^{+-}] + [S_2^{++}][P][S_1^{+-}]\Big[[I] - [P][S_2^{-+}][P][S_1^{+-}]\Big]^{-1}[P][S_2^{--}] \quad (4.60)$$

$$[S^{-+}] = [S_1^{--}]\Big[[I] - [P][S_2^{-+}][P][S_1^{+-}]\Big]^{-1}[P][S_2^{--}] \quad (4.61)$$

$$[S^{--}] = [S_1^{-+}] + [S_1^{--}][P][S_2^{-+}]\Big[[I] - [P][S_1^{+-}][P][S_2^{-+}]\Big]^{-1}[P][S_1^{++}] \quad (4.62)$$

where $[P]$ is the propagation matrix between the two adjacent interfaces (labelled '1' and '2'). Note that the scattering matrices appearing in this and subsequent chapters will *not* have any of the symmetry properties discussed in Chapter 3. The reason for this is that we have not deliberately re-scaled the ray amplitudes to effectively cancel-out the differences in optical impedance encountered by the various rays, and we have also not re-arranged the matrix quadrants in the way that was described. Without these deliberate adjustments, the scattering matrix will have no convenient symmetries.

Combining the scattering matrices of two adjacent interfaces in the way described above effectively reduces the number of interfaces involved by one, so repeated application of the multiple-scattering series-summation (MSSS) equations enables the entire structure to be replaced, in effect, by a single interface that has a known scattering matrix. Once the scattering problem is solved for this single 'effective interface', the calculated amplitudes of the transmitted and reflected waves can be substituted back into the relevant scattering equations to obtain the wave amplitudes in all parts of the actual multi-layer structure, and therefore the resultant electric and magnetic fields in the various layers. Results generated by the 'direct' (see Chapter 3) and 'indirect' methods were compared and were found to be identical.

We are now in a position to model optical confinement in VCSEL cavities incorporating unpatterned and patterned planar defects. We will concentrate on QW and QD VCSELs made from $Al_xGa_{1-x}As$, rather than those with 'bulk' active media, because of their superior electronic density-of-states properties (see earlier). In the modelling, we will ignore the presence of the embedded quantum dots and quantum wells, since their dimensions are typically very small (approximately 10nm) compared to the lattice pitch (probably around 400-550nm) and of similar refractive index (typically 3.6) to

the barrier material (typical index 3.4).

4.12 Numerical modelling results

4.12.1 Patterned planar defects

In this discussion it will be implicitly assumed that the word 'guided' means 'quasi-guided' for brevity, although occasionally the term 'quasi-guided' will be used for emphasis. Breaking the continuous translational symmetry of the background index of a TFPC has a pronounced effect on the spatial field distributions of the quasi-guided eigenmodes. With a uniform background, they can only be guided by internal reflection at the external planar interfaces (i.e. 'film-guided'). After adding a 'top-hat' function perturbation of magnitude $|\zeta(z)|$ to the background index to form a central 'core' layer surrounded by cladding layers of lower background index, however, the set of quasi-guided eigenmodes can in general be partitioned into three subsets containing modes that are guided by the external interfaces (case 1), the internal interfaces (case 2), or by both the internal and external interfaces (case 3). These three cases will be called 'film-guided', 'core-guided', and 'cladding-guided' respectively. There is therefore a much greater variety in the spatial field distributions of the quasi-guided modes when a definite 'core' layer exists. Our nomenclature for the various layers involved is given in Figure 4.6.

If the background index discontinuity between the core and the inner cladding layers is relatively small, we would expect there to be a small number of core-guided modes, in analogy with a standard optical fibre. On the other hand, if the background index of the cladding layers is depressed whilst keeping the core background index fixed then we would expect the number of film-guided modes to be reduced, since the background index discontinuity between the inner cladding and the outer cladding would be lower than before. These considerations suggest that it is possible to have much greater control over the form and multiplicity of the quasi-guided eigenmodes of a TFPC by introducing a non-uniform background index.

Modelling results for two example TFPCs with non-uniform background index will now be presented to illustrate and confirm this hypothesis.

The calculated transmission spectrum of a TFPC incorporating a patterned defect layer of raised background index is shown in Figure 4.5. The material system is 'silicon on silica', and the raised background index of the defect layer could be achieved by heavily

doping it. The vacuum wavelength is $1.55\mu m$, which is within the minimum-loss band of these materials. The structural parameters and other relevant quantities are stated in the caption. It can be seen that there are three quasi-guided modes, corresponding to distinct spikes, labelled 'a', 'b', and 'c'. The electric field intensity profiles (within a unit cell centred on the major axis of a hole) of these three modes are to be found in the insets. These field profiles clearly show quasi-guidance within the core layer (modes 'a' and 'b') and also quasi-guidance by the external interfaces (mode 'c'). Modes 'a' and 'b' are air-modes whilst mode 'c' is concentrated in both the holes and the solid material.

Our second example is for an $AlGaAs$/oxidised-$AlGaAs$ material system, which is often used for semiconductor VCSELS, operating at a vacuum wavelength of 980nm. The structural parameters are quite different (see caption) to those in the first example. The lattice pitch, hole radius, and defect layer thickness all conform to the 'minimum barrier width condition' given earlier.

In this case, the cladding layers are very thin compared to the core layer. Also, the background index discontinuity between the core and cladding layers is much larger than in the first example (3.4-1.6 rather than 3.5-3.45). Figure 4.6 is the transmission spectrum of this structure, together with insets showing the field profiles of the various modes. This structure has four quasi-guided eigenmodes labelled 'a','b', 'c', and 'd'. It can be seen that modes 'a' and 'd' are film-guided (in the solid and in the air respectively), whilst modes 'b' and 'c' are cladding-guided. This example proves that, at a fixed optical frequency within the minimum loss-band of a practically viable material system, it is possible to reduce the 'density of usable states' in a TFPC such that only one mode (mode 'a' in Figure 4.6) will have nonzero overlap with an array of quantum dots embedded in the centre of the core layer, enabling single-mode VCSEL operation (assuming an infinite cavity area in the (x, y) plane. This mode emits light at a fairly small angle (approximately 9 degrees in air) with respect to the surface normal. The lattice pitch and hole radius could be fine-tuned in order to achieve more nearly vertical emission.

These two examples, taken together, prove that core-guided, film-guided, and cladding-guided modes can exist in a TFPC having non-uniform background index. These examples also confirm that it is possible to obtain true quasi-guided defect modes in a TFPC that has a patterned planar defect layer, in contrast to a TFPC having an unpatterned planar defect (discussed later).

The improvements in mode-control in a patterned-defect-layer TFPC-VCSEL are obtained at the expense of a lower Q-factor. For example, mode 'a' in the second example (Figure 4.6) has a Q-factor of 1200, which is an order of magnitude below the Q-factor

of the double-lobed single-TFPC mode in Chapter 3, and a factor of 5.3 below the estimated Q-factor of a typical DBR-VCSEL. However, the optical confinement factor Γ is still much higher than that of a DBR-VCSEL, which ensures that the threshold-current criterion $S \leq S^{DBR}$ is still satisfied even though the Q-factor is lower: the S-factor of mode 'a' is approximately given by

$$S = \frac{250nm}{10nm}\left(1 + (0.9^{-1} - 1)^{-1}\right) \quad = \quad 250 \tag{4.63}$$

where the differential quantum efficiency η_D was estimated to be approximately 0.9 directly from the Q-factor of 1200 (by the equation given earlier). The reduction in the Q-factor increases the differential quantum efficiency, which is 0.63 for the DBR-VCSEL, and therefore increases the slope of the P-I characteristic curve beyond threshold. The Y-factor of this cavity (as defined earlier) will be

$$Y = L_{tot}^{DBR}/L_{tot} = 3410nm/250nm \quad \approx \quad 13.6, \tag{4.64}$$

implying a much lower electrical resistance in the neighbourhood of the cavity, leading to a substantial possible increase in the maximum optical output power. The lattice pitch Λ, hole radius r, and patterned defect layer thickness L_D all satisfy the carrier-confinement condition $w \geq w_{min}$. As stated earlier, this condition is equivalent to the following pair of conditions in the case of a triangular array of centrally-embedded quantum dots that maximally overlap with a single-lobed cavity field intensity profile: $\Lambda \geq 2(r + 100nm)$ and $L \geq 200nm$. Since $\Lambda = 400nm$, radius r must be such that $r \leq 100nm$, which is satisfied because the hole radius is $56nm$. All of our four design criteria summarised in Section 4.10 are therefore satisfied by this TFPC-VCSEL cavity design. Therefore, on the basis of our simple design criteria, TFPC-VCSELs are not ruled-out and may provide much higher maximum attainable output powers, whilst also being much more compact, than conventional VCSELs.

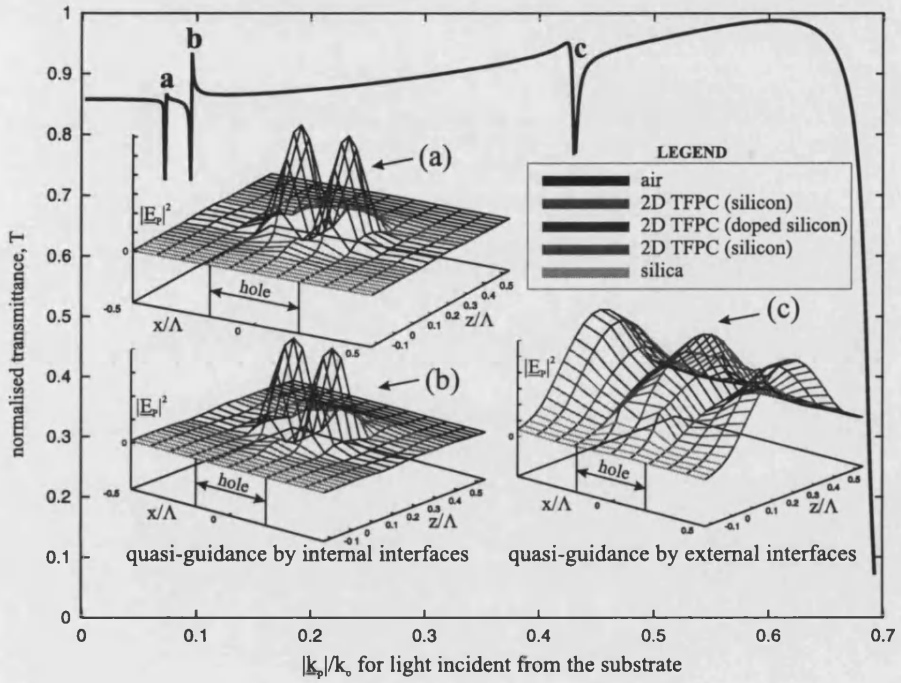

Figure 4.5: Transmittance plot for our first example of a TFPC incorporating a thick patterned planar defect layer, against k_p/k_o, for incidence from the substrate rather than from the cover to ensure that all possible quasi-guided modes are probed (hence the substrate and cover positions are exchanged in the modelling). The parameters are: Λ=536nm, r=100nm, $\phi = 15^o$ measured from $\Gamma - X$, λ_o=1550nm, polarisation state=TM, inner cladding layer thickness=75nm, defect layer thickness=112.5nm, substrate index=1.6, cover index=1.0, inner cladding background index=3.45, defect layer background index=3.5.

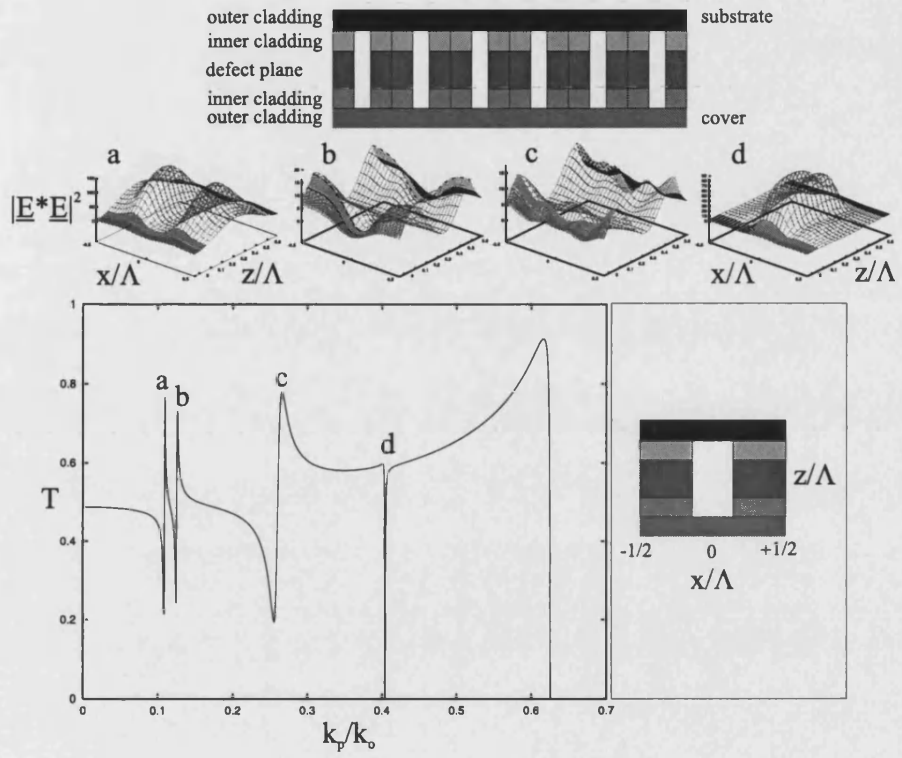

Figure 4.6: Transmittance plot for our second example of a TFPC incorporating a thick patterned planar defect layer, against k_p/k_o, for incidence from the substrate. The insets are as follows: the field intensity profiles of the quasi-guided eigenmodes, a diagram showing the relation between the holes and the coordinate axes of the field profiles, and another diagram showing a cross-sectional view (not to scale) of the cavity structure, cutting through the centres of a row of holes. The parameters for this example are as follows: Λ=400nm, r=56nm, $\phi = 15^o$ away from $\Gamma - X$, λ_o =980nm, polarisation state=TM, inner cladding layer thickness=20nm, defect layer thickness=210nm, substrate index=1.6, cover index=1.0, inner cladding background index=1.6, defect layer background index=3.4.

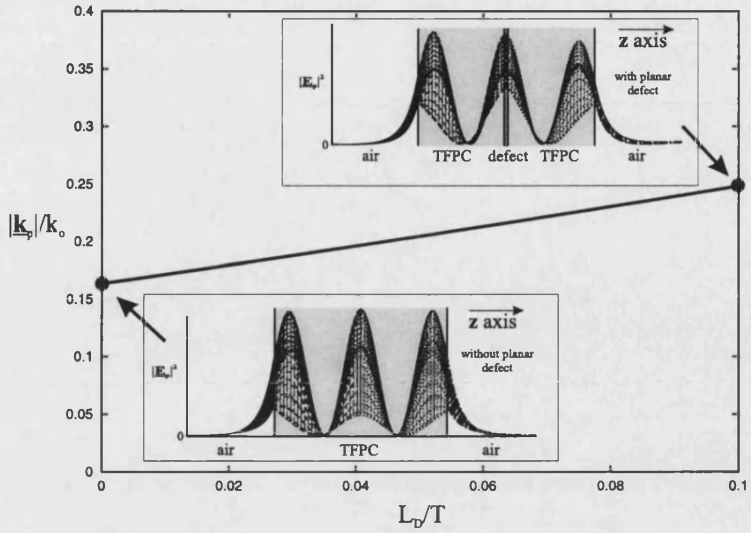

Figure 4.7: The effect, on the location of a particular resonant super-mode, of increasing the thickness L_D of a very thin centrally-embedded unpatterned planar defect. The insets are the electric field intensity profiles along the z axis (at $x = 0$ and $y = 0$) of the super-modes for $L_D/T = 0$ and $L_D/T = 0.1$. T is the half-thickness of the two TFPC layers. The parameters for this example are: λ=980nm, thickness of TFPC layers= 240nm, $\phi = 15^o$ from $\Gamma - X$, Λ=500nm, r=56nm, background index of TFPC layers and defect layer=3.46, polarisation state=TE.

4.12.2 Unpatterned planar defects

Thin planar defects (i.e. $L_D \ll \lambda_o$, where L_D is the defect layer width) introduce only very slight perturbations on the shapes of the field profiles of the resonant modes of a TFPC, although their locations in $(\omega, \underline{k}_p)$ space may be significantly shifted, due to a relatively large phase offset of the higher-order components of the Bloch modes of the unperturbed structure (which have large propagation angles with respect to the surface normal). This is shown in Figure 4.7. Though the planar defect in this case is too thin to support resonant modes of its own, the electric intensity of the resonant 'super-mode' of the entire multi-film structure may nevertheless be peaked at its centre (see insets to Figure 4.7). In this example, the defect plane (which has the same index as the TFPC background material) is centrally positioned and both the cover and substrate media are assumed to be air. The structural and electromagnetic parameters are given in the figure caption.

Much thicker (but still optically thin, i.e. $L_D \leq \lambda_o$) defect layers are able to accommodate one or more field-intensity lobes entirely within their boundaries, but it should be noted that the TFPCs above and below the defect must be resonant for this to occur, which implies that a TFPC having an unpatterned planar defect cannot support high-Q 'defect modes' as-such, because the field intensity cannot be concentrated

exclusively within the defect layer (although it may of course still support relatively low-Q Fabry-Perot resonances that decay away from the defect). Patterned planar defect layers, which were discussed in the previous section, can however support actual high-Q defect modes.

Figure 4.8 is a plot of the transmittance of a particular TFPC having an embedded unpatterned defect layer against the defect-layer thickness, at normal incidence. In addition to the relatively 'slow' periodic variation in the background transmittance with increasing defect-layer thickness, numerous sharp spikes can be seen. These sharp spikes are fairly (not exactly) regularly-spaced, and they correspond to high-Q resonances that emit light vertically from the plane of the film, each of which is labelled with a letter (a-h). Resonance (d) is invisible due to null-coupling. Plotting the electric field intensity of modes 'a', 'b', and 'c' (see Figure 4.9(a), (b), and (c) respectively) reveals that, out of these three resonant modes, only mode 'c' has a local maximum within the defect layer. This local maximum is much lower in height than the maximum field intensity in the TFPC reflectors on either side of the defect, which indicates that the Q-factor of this resonance is relatively low (320, in fact). Resonance 'e', however, has a maximum field intensity in the defect layer equal to that in the TFPC layers (though it has two field-intensity lobes in the defect layer), indicating that it has a relatively high Q-factor (1300 in value). An electric field intensity contour plot along a cross-sectional slice of the structure that supports resonance 'e' is shown in Figure 4.10. In this case, the defect layer is very thick compared with the thickness of the TFPC layers, but still only approximately 458nm. This result confirms that even a very thin TFPC 'coating' applied to the upper and lower surfaces of an unpatterned thin film can force it to have resonant modes of much higher Q-factor than it would otherwise be able to support. An estimate of the Q-factor of an unpatterned dilectric film of the same thickness and background index will now be made. At normal incidence, the internal reflection coefficient will be $R = (n_1 - n_2)^2/(n_1 + n_2)^2 = (1 - 3.46)^2/(1 + 3.46)^2 = 0.3$, and the effective mode number will be $m = 2L_{cav}n_{cav}/\lambda_o = 2 * 458 * 3.46/980 = 4$. Therefore, the corresponding Q-factor is $Q = 2\pi * 4/\ln(1/0.3^2) = 12$, which is two orders of magnitude below 1300.

Given that the Q-factor is 1300, the differential quantum efficiency η_D is approximately 0.9, as in the previous subsection, so the slope of the P-I characteristic curve should be comparable to that in the case of the patterned defect layer. The optical confinement factor Γ is less, however, because of the relatively large defect layer thickness:

$$\Gamma \approx 10nm/((100 + 458)nm) \approx 1/56 \tag{4.65}$$

The S-factor of resonance 'e' is given by

$$S = \frac{(458+100)nm}{10nm}\left(1+(0.9^{-1}-1)^{-1}\right) \quad = \quad 560. \tag{4.66}$$

This S-factor exceeds the limit of 405 in our first design criterion, so its threshold current would be higher than that of a conventional VCSEL. This cavity could of course only be used if the QD array or QW is embedded a quarter of the way into the unpatterned defect layer, thus obtaining maximal overlap with one of the intensity lobes. The Y-factor is, in this case,

$$Y = L_{tot}^{DBR}/L_{tot} = 3410nm/558nm \quad \approx \quad 6.1, \tag{4.67}$$

which implies that the electrical resistance would be higher than that of the cavity design in the previous subsection and therefore the maximum output power would be lower. The carrier-confinement condition $w \geq w_{min}$, where $w_{min} = 100nm$, affects only the defect layer thickness in this case, because the QW or QDs would be placed in the unpatterned layer. This condition is satisfied for the QD or QW positioning described above, because $458nm/4 = 114.5nm \geq 100nm$. This particular cavity design would not be usable in practice, however, because the cover and substrate consist of air rather than solid material, making electrical contact with the device impossible. Besides this, even if the substrate material were solid (in which case the S-factor was found to be even higher than the value given above, for a substrate index of 1.6) it would be very difficult to incorporate unpatterned layers between patterned layers, because of the need to alternate between patterning and deposition. Because this cavity design is impractical, the full spectrum of cavity modes at the operating frequency, emitting at angles other than parallel to the normal, was not investigated. We have discussed this design only for the sake of comparison with the apparently much more viable patterned-defect TFPC-VCSEL. A possible non-VCSEL-related application of unpatterned-defect TFPC resonant cavities is nevertheless mentioned in the Conclusion to this chapter.

4.12.3 Single-film TFPC cavities

In Chapter 3, we demonstrated that a single-film AlGaAs TFPC can support a double-lobed dielectric cavity mode of Q-factor 12000 (see Figure 3.3(a)). This is roughly a factor of 2 above the Q-value of a typical DBR cavity $Q^{DBR} = 6400$. a VCSEL. The corresponding differential quantum efficiency η_D is 0.48, and the S-factor is

$$S = \frac{240nm}{10nm}\left(1+(0.48^{-1}-1)^{-1}\right) \quad = \quad 46. \tag{4.68}$$

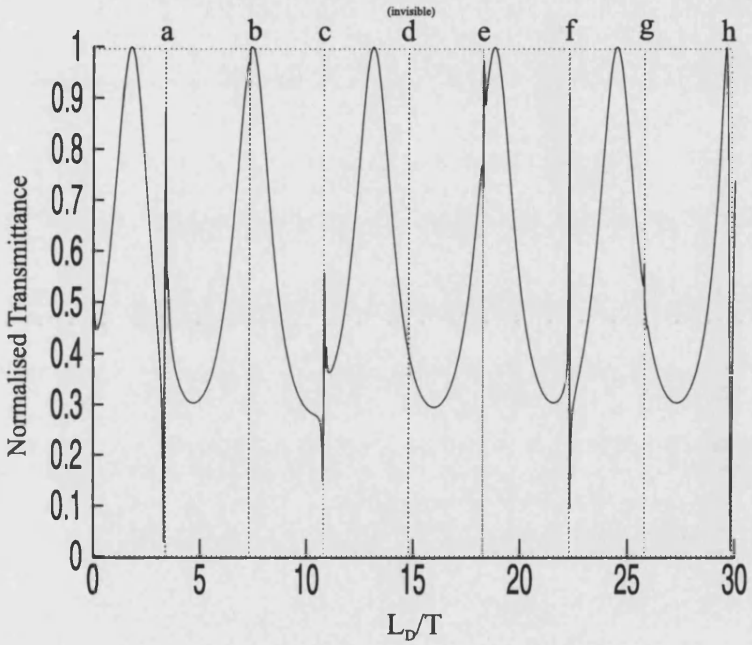

Figure 4.8: Vertically-emitting resonances of a TFPC 'sandwich' structure. The TFPC lattice pitch is 500nm, the TFPCs both have thicknesses of 50nm, the hole radius is 56nm, and all of the layers (patterned or unpatterned) have background refractive indices equal to 3.46. The defect layer thickness is normalised to that of the half-thickness of each TFPC layer, and the input plane-wave has the following parameters: λ_o=980nm, in-plane propagation angle $\phi = 15^o$ from $\Gamma - X$, out-of-plane propagation angle=0^o , polarisation state=TE.

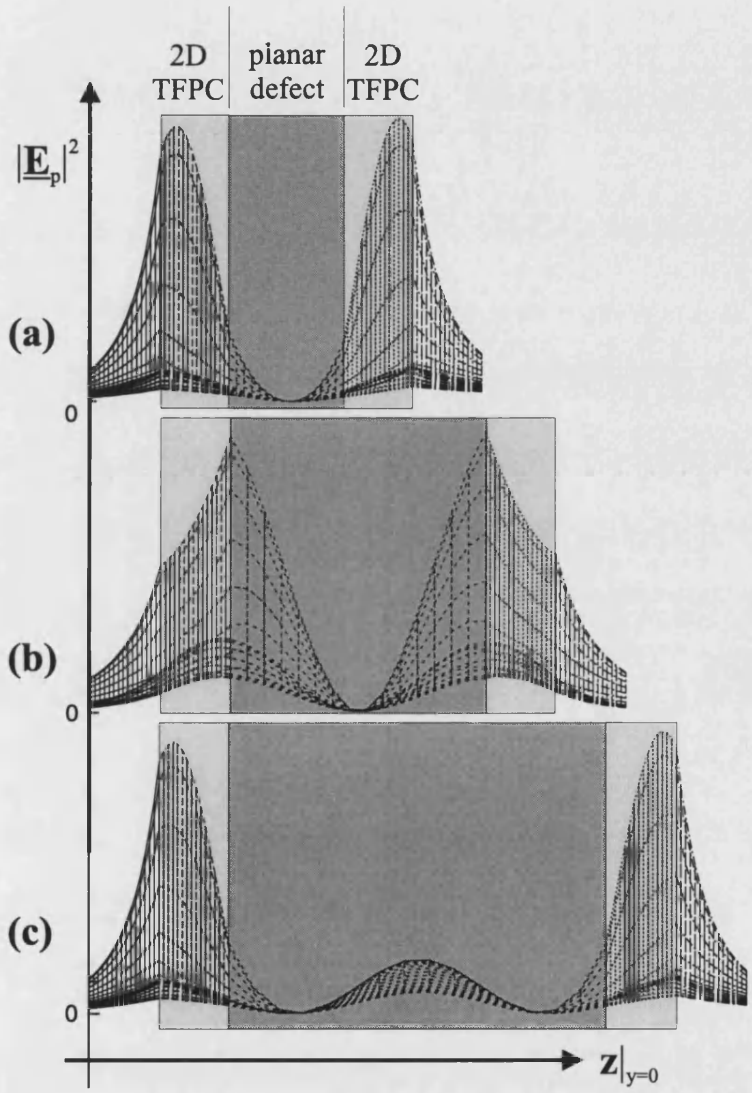

Figure 4.9: A set of electric field intensity profiles for resonances (a) 'a', (b) 'b', and (c) 'c' featured in Figure 4.8. Out of these three resonances, only resonance 'c' has a local maximum in the centre of the unpatterned planar defect.

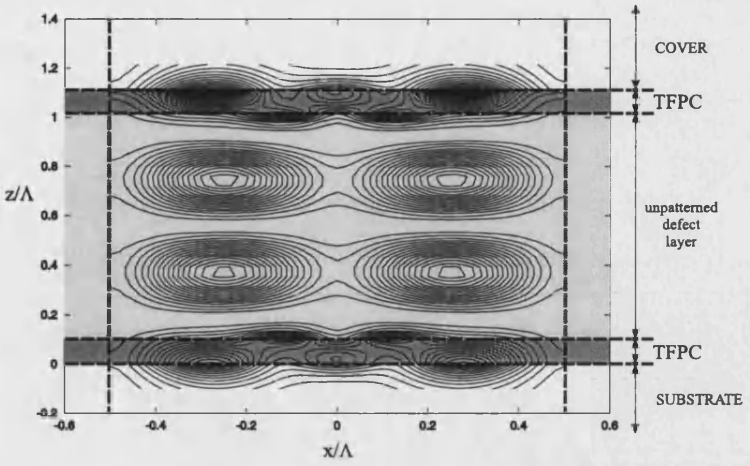

Figure 4.10: Electric field intensity profile of a moderately high-Q (Q=1300) vertically-emitting resonance (resonance 'e' in Figure 4.8) of a multi-film TFPC structure. The planar defect is unpatterned, and the maximum values of $|\underline{E}_p|^2$ in the TFPCs are equal to the maximum values in the defect layer.

The emission angle into air of this double-lobed mode is approximately 10 degrees. Fine-tuning of the structural parameters could decrease this angle. In this case, a quantum dot array with QDs coincident with the cavity field intensity maxima would have to be embedded to produce a VCSEL, but the charge-carrier confinement condition $w \geq w_{min}$ would not be satisfield, however, because the active material would then be too close to the upper or lower interface of the film. This rules-out the use of the double-lobed cavity mode, but there is actually another dielectric mode, at the same frequency, that emits at a near-grazing angle. This mode has a single intensity lobe along the z-axis, a Q-factor of 3200, and a corresponding η_D of 0.78. The S-factor is 109. This mode would have maximal overlap with centrally-located QDs, and the charge carrier confinement condition would be satisfied in this case. Also, the Y-factor would be $1500nm/240nm = 6.3$. Therefore, all of our design criteria are satisfied by this single-lobed mode, but the disadvantage is that the emitted light would not emerge approximately parallel to the surface-normal. The presence of the double-lobed cavity mode would not divert power away from the main emission angle, because the double-lobed mode would have a zero-valued overlap with centrally-embedded quantum dots.

The problem with single-film TFPC cavities in general is that it is more difficult (compared with the patterned-defect case) to find a structural parameter set that yields only one usable cavity mode (i.e. 'usable' in the sense of having non-zero overlap with the embedded active material) subject to the condition that the light emission be parallel to the surface-normal (which is more convenient for fibre-coupling). There are many quasi-guided modes, in general, and their loci in (ω, k_p) space are typically very sensitively dependent upon all parameters. Breaking the continuous translational symmetry

of the background index along the z-axis can improve the extent of control over the muliplicity of the quasi-guided eigenmodes having non-zero overlap with a particular QD array, as demonstrated in subsection 4.12.1.

4.13 Conclusions

By a combination of numerical modelling and the use of simple design criteria relating to differential quantum efficiency, optical confinement factor, threshold current, electrical resistance, and carrier-confinement potential-well width, we have argued that the most promising design for a TFPC-based semiconductor quantum-dot-array VCSEL operating in the near-infrared wavelength range would probably involve an AlGaAs TFPC containing a relatively thick patterned planar defect layer. This basic device structure offers the possibility of attaining a 43% improvement in the differential quantum efficiency and a 1260% reduction in the device resistance (excluding the substrate and the terminal pads) whilst having a slightly lower threshold current, compared to a conventional DBR-VCSEL. A TFPC-VCSEL could therefore, on the basis of our simple model, provide a higher optical output power at a given current beyond threshold, and a higher maximum output power, than a conventional VCSEL, whilst also being potentially much easier to mass-produce and having a similar beam-divergence. The sensitivity of the dependence of the number of usable cavity modes on the structural parameters is greatly reduced by the use of the patterned-defect TFPC structure.

TFPCs containing unpatterned defect layers were also briefly investigated, but our results suggest that they cannot out-perform either conventional VCSELs or our proposed patterned-defect TFPC-VCSELs. It was confirmed that even a pair of very thin (20nm thickness) TFPC 'reflectors' placed on either side of an optically thin unpatterned film could substantially confine light within its boundaries, with an associated Q-factor of at least 1300. Such a structure might be useful in any application in which one needs to concentrate light within a thin film of material that cannot or must not be etched (for example, if its chemical composition or lattice structure must not be altered). Fabrication would, however, be difficult in this case because of the necessity of alternating between patterning and deposition rather than proceeding via several deposition steps followed by a single patterning step, as for a patterned-defect TFPC microstructure.

A full, rigorous, investigation of the carrier-transport properties of TFPC-VCSELs would be required in order to be more certain of their feasibility, but in this chapter we have at least determined that the concept of a TFPC-VCSEL need not be dismissed as being preposterous, and that TFPC-VCSELs may offer many advantages

over 'ordinary' DBR-VCSELs.

Chapter 5

Guided modes of a TFPC and the 'Resonant Tunnelling' Calculation Method

5.1 Introduction

In addition to supporting quasi-guided modes, '2D-patterned' TFPCs also have truly-guided modes [2, 6], provided that the structural parameters satisfy certain criteria [74] which will be discussed later. In principle, therefore, total vertical confinement is possible, whilst still retaining strong and highly controllable modal dispersion. This opens-up the possibility of many additional TFPC-related applications, such as wavelength-selective filtering and beam-steering over relatively long distances (on a micrometric scale). Many groups [75, 76] have concentrated on waveguiding along line-defects in a bandgap-crystal, whilst others [77] have modelled wave-guidance in a thin planar defect embedded in a thick photonic crystal film. Highly dispersive multi-mode wave-guidance has been experimentally observed and partially modelled (by plotting cross-sections through the Bloch mode dispersion surfaces) in thick multi-layer stacks of honeycomb-patterned TFPCs, grown by 'self-assembly' using a composite silicon/silica material system, by Kosaka *et al* [30]. These approaches can indeed give much more guided-mode dispersion control than that attainable in an ordinary unpatterned planar waveguide, in addition to an enhancement in the optical confinment factor Γ (as defined in Chapter 4), but intra-passband TFPC waveguides of the type that we suggest are potentially much more satisfactory in that they can be significantly thinner and also easier to fabricate and test.

One of the main problems in, for example, the design of light-emitting diodes is that a very large fraction of the generated light is trapped in the truly-guided modes. A considerable increase in the output power can therefore be obtained by scattering-out the light from these true waveguide modes [78]. The extraction efficiency can also be improved by suppressing the truly-guided modes altogether, at the operational frequency. In a TFPC, the true waveguide modes can be conveniently suppressed merely by ensuring that the criteria (see later) for the existence of guided modes are not satisfied, by, for example, choosing a relatively large lattice pitch. Furthermore, the number of TFPC guided modes within a pre-specified frequency band or wavevector range can be varied by changing various parameters such as the hole radius, film thickness, and lattice pitch.

The guided modes of '1D-patterned' TFPCs were analysed and discussed in References [44] and [45]. Here, we extend the method employed in these references to the case of '2D-patterned' TFPCs. The extension to the 2D-patterned case is not straightforward, because numerical difficulties are introduced by the reduction in the number of translational axes of invariance. Nevertheless, these problems can be overcome and in this chapter we will present an efficient computational method for the determination of the truly-guided eigenmodes of a 2D-patterned TFPC, and by this method the general trends in the evolution of the guided-eigenmode spectrum with respect to the micro-patterning parameters will be explored.

The high-Q radiative resonant (otherwise known as 'quasi-guided') modes of a TFPC are very convenient for use in practical applications, because one can couple to them merely by aiming a laser beam, or light from a fibre, directly onto the surface of a TFPC from above. However, for certain applications, these modes may be unacceptably lossy. For example, even a small out-of-plane loss would not be desirable in the case of propagation over relatively long distances inside a TFPC. The fact that the quasi-guided modes of a TFPC have small but nevertheless nonzero out-of-plane losses can therefore be an advantage in some situations but a disadvantage in others.

Coupling to the truly guided modes of a TFPC is more difficult. One possible way would be to inject a strongly-focussed beam of light directly into an end-face of a cleaved TFPC, but this involves the splitting of the film and the substrate along a plane normal to the surface and intersecting the patterned area, which is not at all easy since the patterned area may typically be no more than 50 μm wide. Another way would be to excite low-Q radiative modes in an unpatterned part of the film adjacent to the patterned area, which would in turn excite a guided mode in the TFPC provided that the overlap integral between the radiative modes and the guided mode is nonzero. Because of the inevitably large optical impedance mismatch encountered by the injected light as it enters the TFPC, strong scattering will occur, which places

a very heavy restriction on the coupling efficiency of the low-Q radiative modes to the guided mode.

A much more satisfactory solution would be to construct a grating coupler, in which, for example, the lattice pitch of the crystal varies gently from one end of the TFPC to the other, providing a smooth adiabatic transition from quasi-guided to guided modes. With a grating-coupler arrangement such as this, one could excite a quasi-guided mode by direct illumination from above the film, which would then slowly blend into a guided mode whilst it propagates along the TFPC, giving a potentially high coupling efficiency into the guided modes. An experimental demonstration of grating-coupler action in corrugated polymer light-emitting diodes is given in Reference [78]. The propagation of the guided waves in these non-uniformly-periodic structures can be modelled, for example, by the Hamiltonian formalism, as described by Russell & Birks [49], or by the method presented in Chapter 6. Yet another solution to the guided-mode coupling problem, suggested and modelled by Fehrembach *et* al [79], is to superimpose a regular superlattice of small perturbations on the hole radii, thus enabling the originally guided mode to couple to radiation modes in the substrate and superstrate.

Though the calculation of the guided modes of a TFPC is, in principle, similar to that of the quasi-guided modes (see Chapter 3), the numerical methods that must be employed are quite different. This is because the guided-mode problem, as it is traditionally posed, is inputless. Mathematically, the inputless case can be modelled as in Chapter 3 by merely setting the elements of the vector of input amplitudes to zero and solving for the eigenvectors of the field-matching matrix that correspond to an eigenvalue of zero. However, this does not work numerically (in this case) because of quasi-random sign fluctuations in the eigenvalue (as discussed later), rendering iterative root-finding impossible. For 2D-patterned TFPCS, the guided-mode problem must therefore be re-cast into a mathematically equivalent but more numerically tenable form. Several possible methods are considered and tried in this chapter, after first suitably re-expressing the boundary-condition equations involved in the inputless case.

5.2 The inputless case

For convenience, we will begin by re-labelling the ray amplitude vectors in the unpatterned media $\underline{r}$, $\underline{s}$, $\underline{u}$, and $\underline{t}$, instead of $\underline{w}^R$, $\underline{w}^S$, $\underline{w}^U$, and $\underline{w}^T$ respectively.

Let us suppose that there are waves (propagating or evanescent) incident upon a single TFPC film from neither above nor below. In this 'inputless' case, $\underline{s} = \underline{0}$ and $\underline{u} = \underline{0}$.

Consider the transfer matrix of the lower interface (interface 1). This transfer matrix is such that

$$\begin{pmatrix} \left[T_1^{++}\right] & \left[T_1^{+-}\right] \\ \left[T_1^{-+}\right] & \left[T_1^{--}\right] \end{pmatrix} \begin{pmatrix} \underline{u} \\ \underline{t} \end{pmatrix} = \begin{pmatrix} \underline{b}^+ \\ \underline{b}^- \end{pmatrix} \tag{5.1}$$

Similarly, the transfer matrix of the upper interface (interface 2) is such that

$$\begin{pmatrix} \left[T_2^{++}\right] & \left[T_2^{+-}\right] \\ \left[T_2^{-+}\right] & \left[T_2^{--}\right] \end{pmatrix} \begin{pmatrix} [P]\,\underline{b}^+ \\ [P]^*\,\underline{b}^- \end{pmatrix} = \begin{pmatrix} \underline{r} \\ \underline{s} \end{pmatrix} \tag{5.2}$$

Where $[P]$ is the propagation matrix for the Bloch waves travelling or decaying between interfaces 1 and 2.

In the inputless case, the vector $\underline{u}$ in equation 5.1 is $\underline{0}$. Therefore, equation 5.1 can be reduced to the set of equations

$$\underline{b}^+ = \left[T_1^{+-}\right] \underline{t} \tag{5.3}$$

$$\underline{b}^- = \left[T_1^{--}\right] \underline{t} \tag{5.4}$$

Also, in equation 5.2, $\underline{s} = \underline{0}$ in the inputless case. Hence equation 5.2 reduces to

$$\left[T_2^{++}\right] [P]\,\underline{b}^+ + \left[T_2^{++}\right] [P]^*\,\underline{b}^- = \underline{r} \tag{5.5}$$

$$\left[T_2^{-+}\right] [P]\,\underline{b}^+ + \left[T_2^{--}\right] [P]^*\,\underline{b}^- = \underline{0} \tag{5.6}$$

Substituting 5.3 and 5.4 into equation 5.6 gives

$$\left(\left[T_2^{-+}\right] [P] \left[T_1^{+-}\right] + \left[T_2^{--}\right] [P]^* \left[T_1^{--}\right]\right) \underline{t} = \underline{0} \tag{5.7}$$

5.3 The 'determinant' method

Assuming that we are working in a region of in-plane wavevector space in which all waves in the substrate and cover media are constrained to be evanescent (i.e. beyond the radiation cutoff locus of the substrate yet within the boundaries of the first Brillouin zone), equation 5.7 states that the amplitude vector ($\underline{t}$) of the z-evanescent rays emerging from the TFPC at the lower interface must be an eigenvector of the matrix on the LHS that corresponds to an eigenvalue of precisely zero. At any point within the aforementioned region of wavevector space at which this condition is satisfied, there is a guided mode. The smallest non-zero eigenvalue of the matrix on the LHS may loosely be called a 'pseudo-determinant' because it resembles (from a practical point of view) the determinant in the traditional numerical method of finding the guided modes of a

fibre or a planar waveguide. When equation 5.7 is satisfied non-trivially, the matrix has a zero-valued determinant and therefore cannot be inverted.

In Silvestre *et al* [2], we transformed this equation to a slightly different form, because in practice it is not satisfactory for TFPCs. The reason why it is not satisfactory is that the numerically-computed complex eigenspectrum of the matrix in equation 5.7 typically has many small-magnitude members which oscillate quasi-randomly in sign as the in-plane wavevector or the frequency is varied, because of the presence of a large number of relatively weak high-order Bloch modes, which must nevertheless be retained in the computation for the sake of accuracy. If the sign of the 'pseudo-determinant' did not oscillate randomly in sign, one could employ a standard root-finding routine to 'zoom-in' on the guided mode solutions.

5.4 The 'round-trip-operator' method

A better approach is to re-write equation 5.7 so that the desired eigenvalue is unity rather than zero, as discussed in Silvestre *et al* [2]. This may be done in the following way.

Multiplying equation 5.7 from the left by $\left[T_2^{--}\right]^{-1}$, and from the right by $\left[T_1^{--}\right]^{-1}$ gives

$$\left(\left[T_2^{--}\right]^{-1}\left[T_2^{-+}\right][P]\left[T_1^{+-}\right]\left[T_1^{--}\right]^{-1}+[P]^*\right)\underline{t}=\underline{0} \tag{5.8}$$

Rearranging and multiplying throughout from the right by $[P]$, the inverse of which is its own conjugate, gives

$$\left(-\left[T_2^{--}\right]^{-1}\left[T_2^{-+}\right][P]\left[T_1^{+-}\right]\left[T_1^{--}\right]^{-1}[P]\right)\underline{t}=[I]\underline{t} \tag{5.9}$$

This can be written in a simpler form if we remember that, from equation 4.58,

$$\left[T_1^{+-}\right]\left[T_1^{--}\right]^{-1}=\left[S_1^{+-}\right] \tag{5.10}$$

$$-\left[T_2^{--}\right]^{-1}\left[T_2^{-+}\right]=\left[S_2^{-+}\right] \tag{5.11}$$

Substituting these expressions into equation 5.9 gives

$$\left(\left[S_2^{-+}\right][P]\left[S_1^{+-}\right][P]\right)\underline{t}=[I]\underline{t} \tag{5.12}$$

This equation has a simple physical interpretation: since the scattering matrix $\left[S_2^{-+}\right]$ describes reflection at interface 2, whilst $\left[S_1^{+-}\right]$ describes reflection at interface 1, and

$[P]$ describes propagation between interfaces 1 and 2, equation 5.12 requires that the amplitudes of the field Fourier-components of a guided mode must remain invariant after a distributed 'round-trip' inside the TFPC 'cavity.' The matrix on the LHS of equation 5.12 will be called the 'round-trip operator.' The guided mode condition can now be stated in the following form: the set of field amplitudes in the substrate medium associated with a guided mode must be an eigenvector of the round-trip operator corresponding to an eigenvalue of unity, provided that we ensure that the in-plane wavevector, when constrained to be within the boundaries of the first Brillouin zone, does not fall within the substrate cutoff locus. The first part of this condition states that the mode must be resonant, and the second part states that the mode must not be able to radiate into either the substrate or the cover.

This round-trip-operator method was used by Silvestre *et al* [2] to produce the guided mode dispersion diagrams in Figure 5.1. These diagrams refer to TFPCs that have the following parameters in common: lattice pitch=400nm, substrate index=1.6, film index=3.46, film thickness=150nm (which may be fabricated using the same materials as for the structures discussed in Chapter 3). Diagrams (c) and (d) of this set show how the guided mode locus (which is centred on the J-point) evolves as the vacuum wavelength is increased from 972nm to 985nm, with the hole radius fixed at 100nm. In this wavelength interval, only one (approximately circular) guided mode locus exists at any particular wavelength, except in the range 977-979nm, where there is a 'resonance gap'. Resonance gaps (which are not the same as bandgaps) are discussed briefly in Chapter 6. The shading on these diagrams is intended to give an impression of the curvatures of the guided mode dispersion surfaces when plotted in $(\omega, \underline{k}_p)$ space, in which case there are two approximately conical surfaces having opposite signs of curvature, with a narrow gap between them. End-fire coupling to the TFPC, as shown schematically in diagram (a) (with the angle of incidence arbitrarily set to 0.5 degrees away from the normal to the end-face, for illustration purposes), would, for example, result in the excitation of guided modes that intersect the dashed construction line in diagram (b), because of momentum conservation parallel to the cleavage plane. Diagram (b) shows that the group velocity direction of the excited guided mode is very strongly dependent on the vacuum wavelength, with a change in vacuum wavelength of 5nm resulting in a 90-degree rotation of the group velocity vector (shown by the single-headed arrows). Guided modes such as this would be very useful in WDM and other wavelength-dependent beam-steering applications, although in practice the abrupt air/crystal transition should be replaced by a gentler, graded, transition to improve the coupling efficiency into the guided modes (see Chapter 6 for more on graded transitions). Diagrams (e) and (f) show the effect on the guided mode locus of varying the hole radius, with the vacuum wavelength fixed at 980nm. A similar trend to that in (c) and (d) is apparent, with two conical surfaces appearing in $(r, \underline{k}_p)$ space, with a gap existing between 98 and 100nm (approximately). Diagrams (e) and (f) demon-

strate that the guided mode loci are sensitively dependent on the internal structural parameters of the TFPC, confirming the necessity of tight fabrication tolerances and suggesting that the parameter grading with respect to in-plane position in an MLP-TFPC (see Chapters 1 and 6) may only need to be very subtle in order to produce very pronounced photonic potential wells.

The diagrams discussed above were generated by a very laborious and time-consuming process of plotting the real and imaginary parts of the members of the round-trip-operator eigenspectrum closest to $(1,0)$ in the complex plane, for many hundreds of points along particular line segments in in-plane-wavevector space. This method works, and it avoids the problems with random eigenvalue sign oscillation discussed in the previous section, but it takes a distressingly large amount of time and effort to produce a guided mode dispersion diagram in this way, so it is not good for quickly sweeping through sets of TFPC parameters in search of interesting guided mode dispersion properties.

5.5 The 'generalised eigenvalue problem' method

In an attempt to reduce the amount of time required for the calculation of the guided modes, another method was implemented. This involved the re-casting of the resonance condition described above in the form of a so-called 'generalised eigenvalue problem.' The archetype of a generalised eigenvalue problem is $\beta [A] \underline{x} = \alpha [B] \underline{x}$, where the complex numbers α and β are not necessarily finite. Note that β here has no connection at all with the Bloch-mode z-momentum, β_j. The generalised eigenvalue problem reduces to the same form as an ordinary eigenvalue problem when α is finite, β is nonzero, and $[B]$ is invertable, in which case the eigenvalue is α/β and the matrix is $[B]^{-1}[A]$. If we go back to equation 5.7 and assign the two terms on the LHS to the matrices $[A]$ and $[B]$ as follows:

$$[A] = \left[T_2^{-+}\right][P]\left[T_1^{+-}\right] \tag{5.13}$$

$$[B] = -\left[T_2^{--}\right][P]^*\left[T_1^{--}\right] \tag{5.14}$$

then the resultant generalised eigenvalue problem is found to be, numerically, much more resistant to random sign oscillations in the eigenspectrum (or rather eigenspectra, since in this case there are two sets of scalar quantities involved, α and β). It was therefore relatively easy to filter the eigenspectra (by choosing suitable upper and lower bounds) to leave only the guided-mode solutions. However, this method is, in practice, almost as slow and laborious as the previous method, because upper and lower bounds on the acceptable eigenvalues have to be chosen by visually inspecting a series

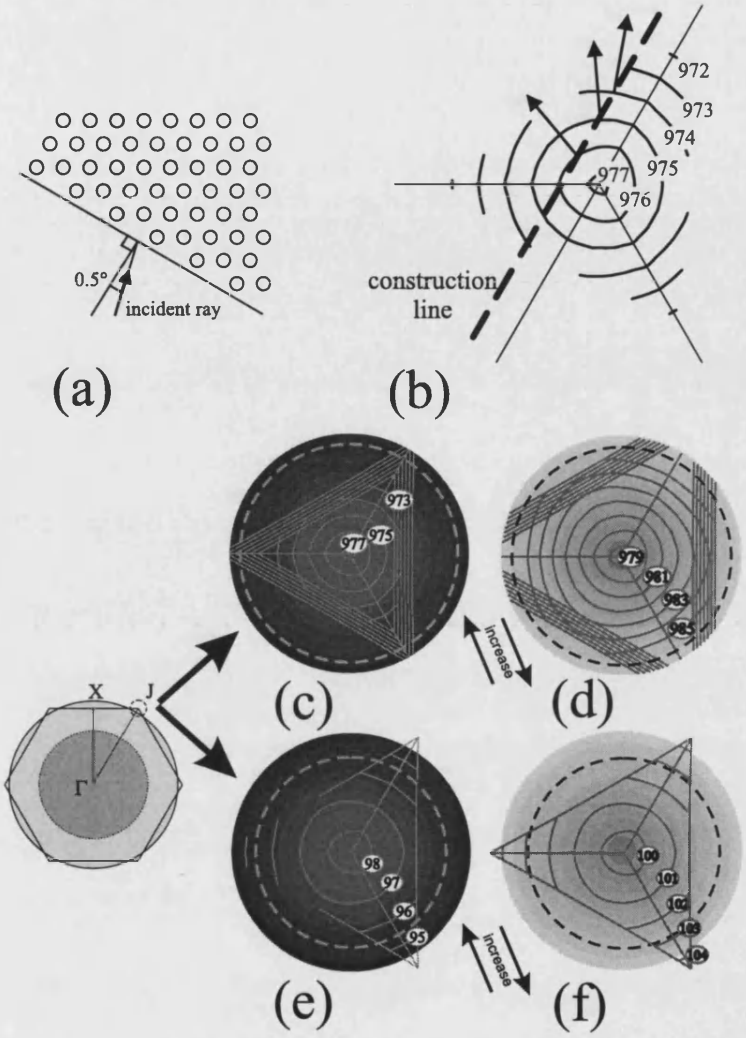

Figure 5.1: Guided mode dispersion diagrams produced by Silvestre *et al* [2] for a single-film TFPC. (a) is a schematic illustration of end-fire coupling to a cleaved TFPC, resulting in the excitation of guided modes that intersect the dashed construction line in (b), which shows the guided-mode loci in in-plane wavevector space for a range of vacuum wavelengths between 972nm and 977nm, at a fixed hole radius of 100nm. Varying the wavelength (labelled in nm beside each locus) between 977nm and 985nm at fixed hole radius (100nm) gives the dispersion-surface cross-sections (each at fixed wavelength) in (c) and (d), whilst varying the hole radius (value in nm shown adjacent to the curves) at a fixed wavelength of 980nm gives (e) and (f). The small inset shows the boundaries of the first Brillouin zone, together with the cover and substrate cutoff circles at a vacuum wavelength of 980nm (which are shaded dark and light respectively). The small dashed circle centred on the J-point in the inset occupies the same region of wavevector space as the large dashed circles in (c),(d), (e), and (f).

of graphs, as before, so it is difficult to automate.

5.6 The 'resonant tunnelling' calculation method

Having established that the problem of finding guided mode solutions for a TFPC is trickier than we expected, it would perhaps be helpful to re-examine our basic assumptions. Our most basic assumption was that the situation being modelled must not have any external light-input. However, this assumption is not necessary. All we require is that no light must propagate to or from the TFPC, which does not prohibit propagating waves that are not directly in contact with the TFPC. This naturally leads to the idea of transforming the problem from an inputless type to one in which there is external light-input, as in the previous chapters, by simulating a 'prism-coupling' experiment (see [80, 81]). In a prism-coupling apparatus, light is coupled into a guided mode of a planar waveguide by photon-tunnelling from a prism that is in a state of frustrated total internal reflection.

The photon-tunnelling occurs across an air-gap between the base of the prism and the upper surface of the waveguide, and this air-gap must be wide enough so that the waveguide modes are not significantly perturbed, and yet narrow enough so that a reasonable amount of power can be coupled into them. The optimal air-gap width, in practice, is typically between $\lambda_o/8$ and $\lambda_o/2$. In the prism-coupling regime, the light reflected from the base of the input-coupling prism dips sharply in intensity when the in-plane wavevector of the vertically evanescent light tunnelling across the air-gap matches that of a guided mode of the planar waveguide. Of course, the refractive index of the input-coupling prism must be higher than that of the substrate material to avoid the excitation of 'substrate modes' (i.e. modes that decay into the cover medium but nevertheless radiate light into the substrate).

It is also necessary that the substrate, which has a finite thickness in practice, be placed upon a material (which we will call the 'output-coupling medium') of refractive index equal to or greater than that of the input-coupling prism, so that indirect light transmission from the waveguide modes is possible. This light transmission is indirect in the sense that it is due to photon tunnelling from the waveguide to the material below the substrate, in which it has a real-valued momentum along the z-axis and can therefore propagate towards $z = -\infty$. Otherwise, the contrast of the reflection dips would be reduced to zero, rendering the experiment useless. The reason for this is simply that since the sum of the normalised reflectance and transmittance must be unity, the reflectance dip associated with the excitation of a guided mode must always be accompanied by an equal and opposite spike in the transmittance, but if

there is no possibility of indirect transmission (in the sense defined above) then the transmittance must necessarily be zero, and therefore the normalised reflectance must be unity, irrespective of any guided modes that may be present.

The idea, then, is to find the guided modes of a TFPC by numerically modelling a prism-coupling experiment. In this, the assumptions that will be made are reminiscent of those employed in supercell calculations of guided modes of optical fibres (except of course that the structure is not being tiled in this case) in that we suppose that the guided mode field intensity will exponentially decay away from the waveguide with sufficient rapidity such that it is negligible at the interfaces of the input and output coupling media. The model is shown schematically in Figure 5.2. Note that the cover and substrate media have been truncated in height to L_{TC} and L_{TS} respectively. Note also that in this configuration, photons can tunnel into the TFPC from above and then tunnel from the TFPC to the output coupling medium, using the TFPC as a sort of 'stepping-stone,' which only functions as such when a guided mode is excited (i.e. at resonance). Direct tunnelling through the intervening gap (in real-space, not frequency), without the assistance of a resonant state, would be unlikely due to the large exponential decay of the field over the distance $L_{TC} + L + L_{TS}$. Direct tunnelling merely contributes to the smoothly-varying background transmittance or reflectance.

For convenience, the refractive indices of the input and output coupling media, n_{IN} and n_{OUT} respectively, will both be set to a common value n_p such that at grazing incidence ($\theta = 90°$) one hits the J-point of the TFPC Brillouin zone if the in-plane wavevector is aligned along the $\Gamma - J$ direction. We do not need to access the region beyond, because the J-point is the furthest point from the origin in the irreducible Brillouin zone.

The advantage of this 'resonant tunnelling' calculation method is that the presence of a guided mode at a particular frequency and in-plane wavevector is shown by a dip or spike in a single real-valued positive-definite scalar variable that is an actual physical quantity that could in principle be measured. There is therefore no ambiguity when interpreting results obtained by this method. In addition to this, it is almost as fast as the radiative resonant mode calculation methods in the previous chapters, so parameter sets can be tried quickly and easily to find interesting cases.

We will set the values of L_{TC} and L_{TS} equal to L_T, which will be called the 'coupling gap.' By plotting the positions of the spikes in the calculated transmittance of a particular vertically-truncated TFPC as a function of in-plane wavevector along a certain crystallographic direction (beyond substrate cutoff) for various values of L_T, at a fixed optical frequency, one can determine the optimum coupling gap L_T^{opt}. Such a graph is to be found in Figure 5.3. As we said earlier, the choice of L_T must entail

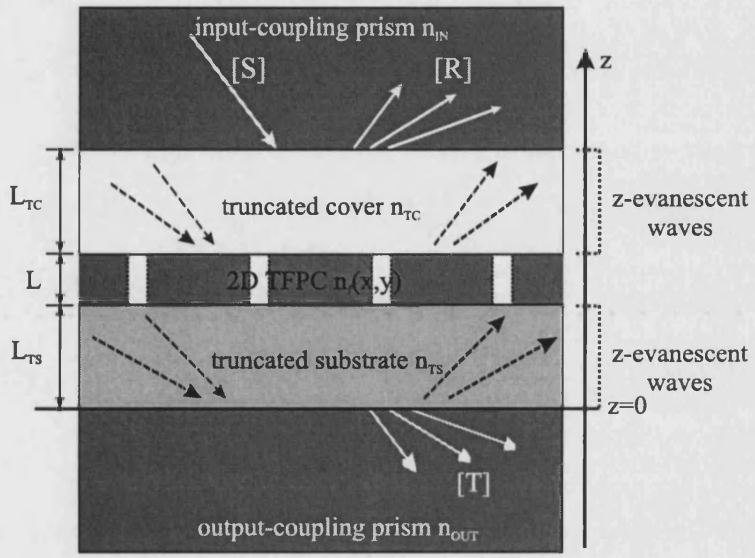

Figure 5.2: Schematic illustration of the situation modelled in our 'resonant tunnelling' calculation method for the guided modes of a TFPC. The cover and substrate media, which were assumed to be semi-infinite in Chapter 3, are truncated to heights L_{TC} and L_{TS} respectively, and semi-infinite high-index prisms are placed above and below. Transmission of light across the intervening space between the prisms would occur primarily via a resonant tunnelling process. Direct non-resonance-assisted transmission is unlikely, due to the relatively large gap $L_{TC} + L + L_{TS}$ between the input prism and the output prism. The appearance of pronounced peaks in the angular or spectral transmittance would reveal the presence of guided modes.

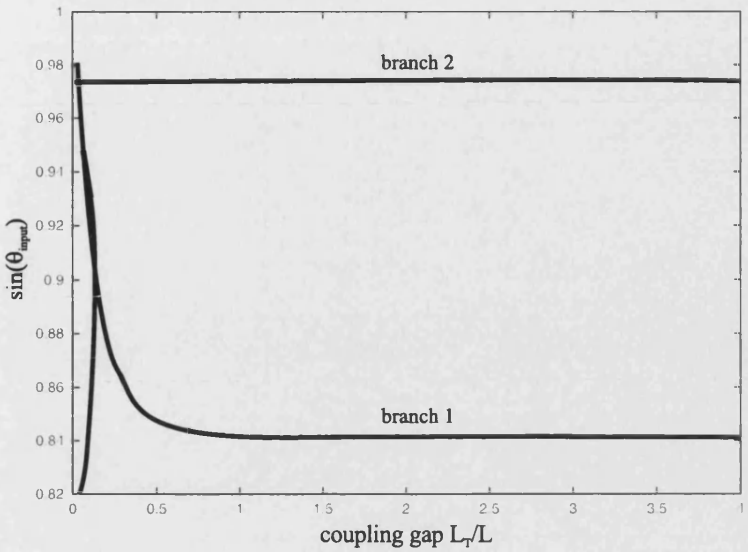

Figure 5.3: Positions of the transmittance peaks of a TFPC in terms of $\sin(\theta_{input})$, against normalised coupling gap L_T/L, where θ_{input} is the angle of incidence from the input prism, L_T is the coupling gap, and L is the thickness of the TFPC (which is fixed). The in-plane direction of the incident beam is aligned along $\Gamma - J$, and the other parameters are as follows: Λ=340nm, r=60nm, TFPC background index n_f=3.46, cover index n_{cov}=1.6, substrate index n_{sub} = 1.0, vacuum wavelength=1551.4nm, film thickness=330nm, value of prism index as explained in the text.

a compromise between coupling efficiency and mode perturbation. From this graph, one can see that a coupling gap L_T approximately equal to the film thickness L (i.e. $L_T/L \approx 1$) is optimal in the particular case to which these diagrams refer. Beyond this coupling-gap value, the positions of the two guided modes (which of course coincide with the transmittance spikes) can be seen to be very close to their respective asymptotes. However, it should be stressed that the choice of the coupling gap L_T is not particularly critical: it is sufficient for it to be merely of the right order of magnitude. Multiple-scattering series summation was used to combined the scattering matrices of the four interfaces in the model, and the transmittance and reflectance were computed from the 'total' scattering matrix thus obtained, as described in chapter 4.

5.7 Results obtained using the 'resonant tunnelling' calculation method

Now that we have a convenient method for the calculation of the guided eigenmodes, the evolution of the guided-mode dispersion surfaces in (ω, k_p) space with respect to variation in the various parameters will briefly be investigated, by plotting cross-sectional

slices at fixed frequency. By examining the field microstructure of two particular guided modes, we will then show that two basic types of guided mode are possible in a TFPC: 'bulk-guided' and 'surface-guided'. The parameters that will be varied are the frequency, the hole radius, and the film thickness (whilst keeping all other parameters fixed).

5.7.1 Varying the optical frequency

Figure 5.4(a) is a wavevector diagram calculated by the 'resonant tunnelling' method. It shows the loci of the guided eigenmodes of a TFPC microstructure having the following parameters: lattice pitch Λ=400nm, hole radius r=100nm, film index n_f=3.46, substrate index n_s=1.6, film thickness L=290nm, cover index n_c=1.0. The vacuum wavelength is fixed at 1551.4nm. Figures 5.4(a) and 5.4(b), taken together, demonstrate that increasing the frequency from that in 5.4(a) by approximately 2.5% in this case, so that guided-mode components from adjacent Brillouin zones interact, gives similar stop-gaps in wavevector space (in this case, $\underline{k}_p$) to those encountered in the discussion of simple wavevector diagrams for 1D-patterned low-contrast crystals in Chapter 1. Such stop-gaps, as we remarked in Chapter 1, are created by the mutual repulsion of modal loci at Brillouin zone boundaries. In Figure 5.4(a), there are two sets of guided-mode loci, whilst in Figure 5.4(b) there are three. This illustrates the general trend that increasing the frequency increases the number of dispersion surfaces, as expected. In diagrams such as these, some guided-mode loci are found to increase in size with increasing frequency, whilst others decrease in size (see, for example, Figure 5.1). Such behaviour indicates the presence of positive and negative refraction [31] respectively. Positive refraction occurs whenever one is above a resonance gap, giving outwards-directed group-velocity arrows. Negative refraction, on the other hand, happens below a resonance gap, yielding inwards-directed group velocities.

There is a simple criterion [74] for deciding whether or not a particular TFPC may or may not support guided modes, based solely on the value of the lattice pitch, the substrate index, and the vacuum wavelength. This criterion is that the J-point of the triangular lattice must not lie within the substrate cutoff circle at the working optical frequency, which can be expressed symbolically as $4\pi/(3\Lambda) \geq k_o n_{sub}$, where k_o is the vacuum wavevector magnitude, $2\pi/\lambda_o$. This criterion ensures that there will be areas of in-plane wavevector space in which none of the plane-wave components of the Bloch modes can radiate into the cover and substrate media. If this condition is not satisfied then there can be no guided modes, but if it is satisfied then there *may* be guided modes. A resonance condition must of course also be satisfied (see later), in addition to this, within a non-radiative portion of wavevector space.

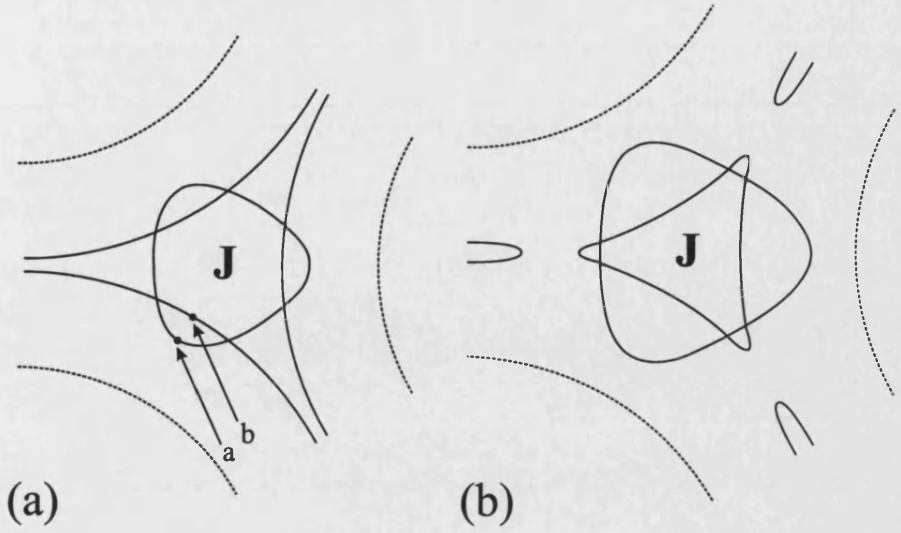

Figure 5.4: Calculated TFPC guided-mode loci in in-plane wavevector space at two slightly different frequencies, corresponding to vacuum wavelenths of (a)1551.4nm and (b)1514.0nm. The structural and electromagnetic parameters are given in the text. The dashed lines are portions of the tiled radiation cutoff loci of the substrate material. Each diagram is centred on the crystallographic J-point. Two points along the loci in (a) are labelled for subsequent reference.

5.7.2 Varying the hole radius

Figure 5.5 shows the effect, on the guided mode loci, of increasing the hole radius of a TFPC (i.e. increasing the air-filling fraction) whilst keeping all other parameters constant. Diagram (a) is for a hole radius of 45nm, and diagram (b) is for a hole radius of 80nm. The general trend that can be deduced from diagrams such as these is that the stop-gaps in $\underline{k}_p$-space between adjacent guided mode surfaces increase in width with increasing hole radius, thus tending to 'squeeze-out' the guided modes, leading to a reduction in the number of guided mode branches at fixed frequency. For much higher air-filling fractions than that in (b), in-plane bandgaps appear, resulting in the elimination of guided modes altogether.

5.7.3 Varying the film thickness

Thinking naively, the film thickness required in order that a TFPC may have a guided mode might be predicted by requiring that a whole number of half-wavelengths must be accommodated between its upper and lower boundaries. For this, it is necessary to know the value of the propagation constant along the z axis (β) of the guided mode. This simple resonance condition [44] can be expressed as $N\pi/L = \beta$, where

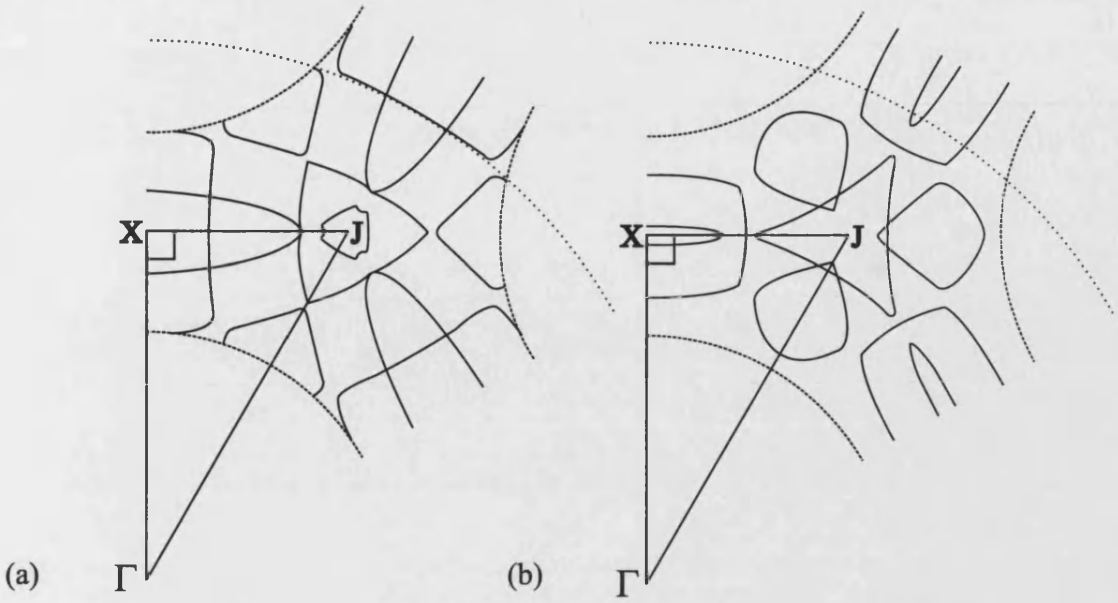

Figure 5.5: Calculated TFPC guided-mode wavevector diagrams for two different hole radius values: (a) 45nm and (b) 80nm (whilst keeping all other parameters constant). The other parameters are: L=290nm, Λ=400nm, film index=3.46, substrate index=1.6, cover index=1.0, vacuum wavelength=1551.4nm. The dashed lines are portions of the tiled radiation cutoff loci of the substrate material, and the dotted line is the cutoff locus of the background film material.

N is a positive nonzero integer and L is the thickness of the film. If this condition were applicable, then the guided-mode loci could be calculated simply by taking cross-sectional slices, at fixed out-of-plane propagation constant β, of the dispersion surfaces of the Bloch eigenmodes. However, there is a problem with this since in general a guided mode consists of more than one significant Bloch mode, which implies that the guided modes will not have well-defined β values. Therefore the trends associated with varying the film thickness are not as simple as may be expected. Nevertheless, the number of guided-mode branches on the wavevector diagrams does increase with increasing film thickness. This is illustrated in Figure 5.6: diagram (a), which is for a film thickness of 340nm, has four distinct 'branches', but increasing the film thickness by approximately 6% gives five distinct 'branches', as shown in (b).

5.7.4 Bulk-guided and surface-guided modes

We shall now look at the field microstructure of two guided modes residing at different points along the guided-mode loci in Figure 5.4(a). Cross-sectional electric field intensity ($|\underline{E}(x,y,z)|^2$ at fixed $y = 0$) plots of the guided modes at the points labelled 'a' and 'b' in this wavevector diagram reveal that there are two distinct types of guided

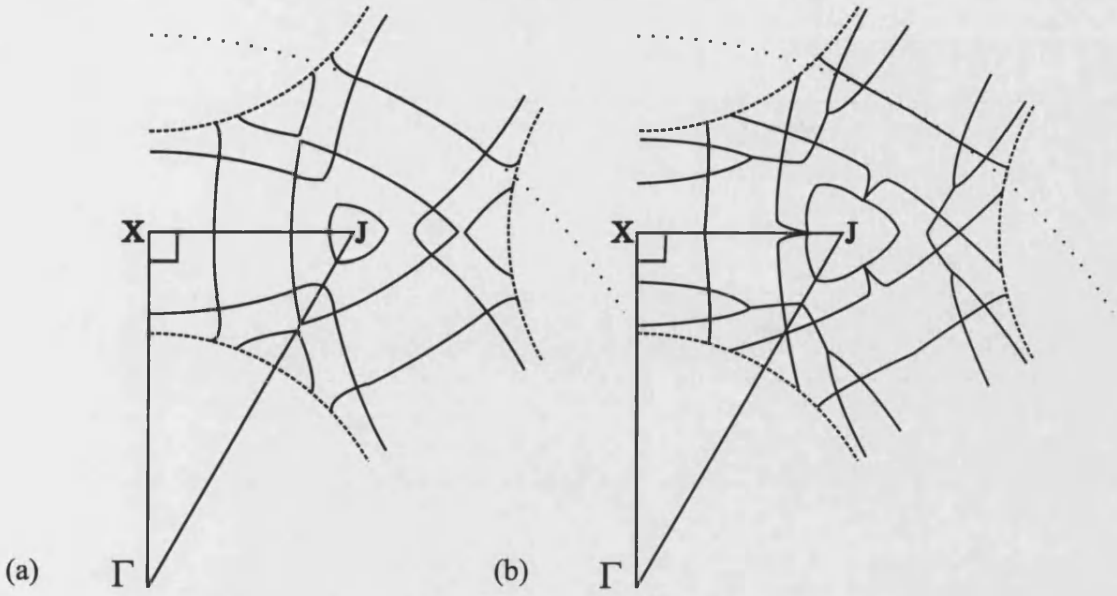

Figure 5.6: Calculated TFPC guided-mode wavevector diagrams for two different film thicknesses: (a) L=340nm and (b) L=360nm (whilst keeping all other parameters constant). The other parameters are: Λ=400nm, r=45nm, film index=3.46, substrate index=1.6, cover index=1.0, vacuum wavelength=1551.4nm. The dashed lines are portions of the tiled radiation cutoff loci of the substrate material, and the dotted line is the cutoff locus of the background film material.

mode in the case of a TFPC: 'bulk-guided' (see Figure 5.7(a)) and 'surface-guided' (see Figure 5.7(b)), the difference between them being that the field intensities are concentrated in the main bulk of the film in one case ('a'), and primarily concentrated in the neighbourhood of the film interfaces in the other case ('b'). The particular bulk-guided mode featured in diagram (a) has two field-intensity lobes concentrated almost entirely within the holes. The surface-guided mode in (b), however, is much less concentrated in the holes, and its field-intensity maxima are located at the upper and lower boundaries of the film. Electric field intensity plots of the same modes along planes parallel to the film interfaces confirm these findings: Figure 5.8 (which is for the plane $z = T/2$ where T is the film half-thickness) shows that the cross-sectional view of the bulk-guided mode chosen in Figure 5.7(a) is representative of the field profile along all possible cross-sectional slices, in that the double-lobed electric intensity surface does indeed rapidly decay away from the hole boundaries in the (x, y) plane, indicating that this may be called an 'air-mode'. Contour lines, projected onto the (x, y) plane are also shown, to make this clearer. Two plots of the electric intensity ($|\underline{E}(x, y, z)|^2$ at fixed z) along two different slices, parallel to the (x, y) plane, of the surface-guided mode are given in Figure 5.9: the plane of plot (a) is coincident with the upper surface of the film ($z = 2T$) and that in (b) passes along the central plane of the film ($z = T$). In both plots, the field intensity is seen to be approximately circularly symmetric about the

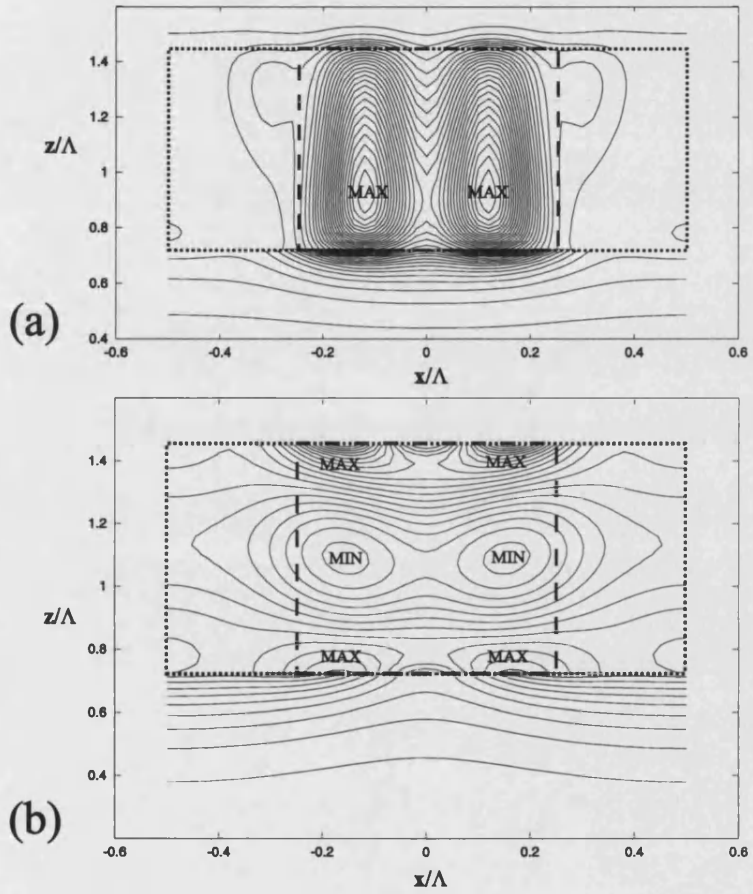

Figure 5.7: Field profiles of (a) bulk-guided and (b) surface-guided true waveguide modes. These plots respectively refer to the points 'a' and 'b' labelled in the guided-mode wavevector diagram shown in Figure 5.4(a), and they are contour maps of the electric field intensity along an (x, z) cross-sectional slice through the TFPC, cutting through the centres of a row of holes. The local intensity maxima and minima are indicated. The dashed lines mark the hole boundaries and the dotted lines coincide with the external interfaces of the patterned film.

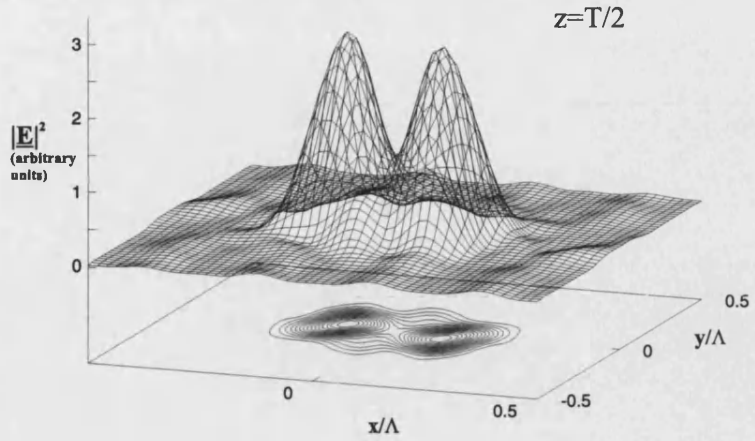

Figure 5.8: A surface plot, in the (x, y) plane, of the electric field intensity (in arbitrary units) of a double-lobed bulk-guided air-mode. The mode is the same as that featured in Figure 5.7(a). Contour plots projected onto a plane are also shown. The origin of the (x, y) plane coincides with the centre of a hole, and the z-coordinate, measured from the lower interface, is fixed at $T/2$ where T is the half-thickness of the film.

centre of each hole. This surface-guided mode cannot be called an 'air-mode' because Figure 5.9(b) shows that the electric intensity in the the central plane increases as one moves away from a hole. This mode is therefore of mixed character, being neither exclusively an air mode nor a dielectric mode.

5.8 Conclusions

In this chapter, we have developed a new fast and 'fool-proof' method for calculating the guided modes of a TFPC, based on the simulation of an imaginary 'prism-coupling' experiment. The advantage of this method is that, since the guided-mode problem is transformed from an inputless situation to one in which there is an external input of light, the guided modes can be reliably located in (ω, k_p) space simply by searching for sharp reflection-minima or transmission-maxima. This method circumvents the laborious semi-manual root-finding process that is necessary if there is a quasi-random sign oscillation in the determinant, as in the other methods that were tried.

This 'resonant tunnelling' calculation method was then used to generate several TFPC guided-mode dispersion diagrams, with the intention of illustrating the effect of altering the structural parameters of the photonic crystal on the guided-mode multiplicity at fixed frequency, the control of which can be accomplished simply by changing the hole radius, lattice pitch, and film thickness. This method is 'indirect' in the sense that it employs the scattering matrix method used in Chapter 4, in conjunction with the

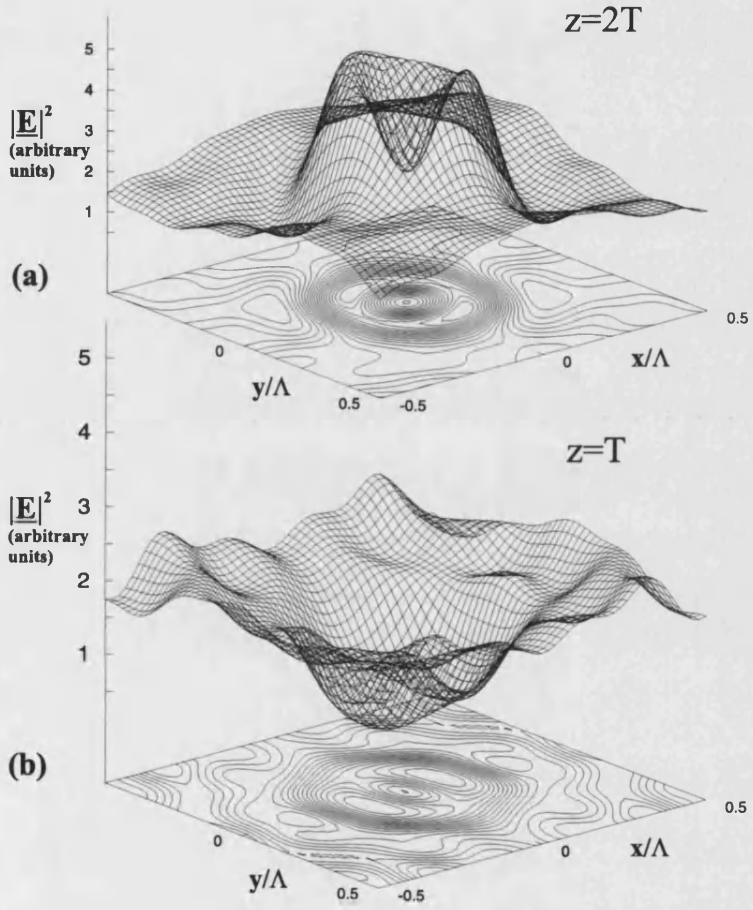

Figure 5.9: Electric intensity plots for (x, y) cross-sectional slices through a surface-guided mode at (a) the top surface of the film and (b) in the middle of the film. Contour plots projected onto a plane are also shown. The surface-guided mode is the same as that depicted in Figure 5.7(b). The origin of the (x, y) plane coincides with the centre of a hole and the origin of the z axis is at the lower interface.

multiple-scattering series-summation equations [17] to combine the partial scattering matrices of the individual interfaces to obtain the total scattering matrix of the imaginary prism-coupler set-up. These wavevector diagrams also demonstrate the extremely dispersive nature of the guided modes of a TFPC and the variety and complexity of the functional forms of their loci. During the ensuing discussion, the criteria [74] that must be satified in order for guided modes to exist were presented. We found, by examining the field-microstructure at various points along the guided-mode loci, that the bound modes of a TFPC may be classified according to whether they are 'bulk-guided' or 'surface-guided'. No such dichotomy exists in the case of the guided modes of an ordinary unpatterned planar dielectric waveguide, which serves to emphasise that the guided modes of a TFPC obey distinct rules of their own.

Fundamentally, there is no difference between a guided mode and a quasi-guided (i.e. high-Q radiative resonant) mode except that guided modes reside beyond the radiation cutoff locus whilst quasi-guided modes lie within. Both types of mode have Fourier amplitude vectors that are invariant (or nearly so) when acted on by the 'round-trip operator' (which is the LHS of Equation 5.12) so both types of mode may be described as 'resonant'. The physical similarity between the guided and quasi-guided modes implies that our explanations of the general properties of quasi-guided modes (see Chapter 3) also apply to guided modes, with the modification that there is no out-of-plane loss.

Chapter 6

A general method for designing TFPC integrated optical circuits

6.1 Introduction

Merely Locally Periodic (MLP) TFPCs were briefly introduced and discussed in Chapter 1. Only quasi-guided and guided resonant local modes can be employed in the operation of MLP-TFPC integrated optical devices, because all other modes have high out-of-plane losses. The essential idea behind this chapter is that by carefully surveying $(\omega, \underline{k}_p)$ space to locate and subsequenty examine these resonances, the operation of even very elaborate non-uniformly periodic TFPC structures may be simulated without the use of a super-computer (although a high-specification UNIX workstation will be required). This promising concept is now the subject of an EPSRC research project.

We begin with a discussion of resonance diagrams before explaining how they can be applied to the analysis of MLP-TFPCs.

6.2 Resonance diagrams

A 'conventional' wavevector diagram, examples of which are to be found in Chapters 1 and 2, indicates the locations of the eigenmodes in (k_x, k_y, k_z, ω) space. However, as we have shown in Chapter 3, a resonant mode of a structure having at least one axis of translational invariance typically consists of a linear combination of several eigenmodes, which generally have different values of β, both real and imaginary. Whilst β is a 'good

quantum number' for any particular eigenmode, a linear combination of eigenmodes has no particular β value. Therefore, a resonant mode of a photonic microstructure having at least one axis of translational invariance can be labelled only by $\underline{k}_p$ and ω. The loci of such resonant modes form a set of continuous surfaces in $(\underline{k}_p, \omega)$ space, and diagrams that show the locations of resonances in $(\underline{k}_p, \omega)$ space, or cross-sections thereof, are called 'resonance diagrams' in this thesis, of which Figure 3.5 is an example.

A very useful variation on the theme of the basic resonance diagram will now be described, in which a set of isocontour lines are plotted, in $(\underline{k}_p, \omega)$ space, of a scalar function that is capable of indicating the presence or absence of a resonant mode. A suitable function is the transmittance, T. An isocontour map of $T(\underline{k}_p, \omega)$ of a photonic microstructure contains much more information about its resonant modes than an ordinary resonance diagram, as we will see shortly. The high-Q resonances are to be found wherever the isocontour lines are noticeably bunched together, indicating a steep rate of change of transmittance with respect to angular frequency ω or $\underline{k}_p$, and because of the sigmoid shape of the spectral or angular transmittance in the immediate locality of a typical TFPC resonance (see Chapter 3), the contour line density will generally be a local maximum at the central angular frequency of a resonance, except, of course, in rare cases where the resonance involves only one significant eigenmode, in which case the line-shape will be Lorentzian and the central frequency will be at a local minimum of contour-line-density, between maxima encountered at both positive and negative detuning. From a 'resonance contour map,' such as this, one can directly and easily deduce the extent of temporal and spatial localisation of any particular resonant mode.

The extent of temporal delocalisation is indicated by the reciprocal of the HWHM of the contour line density, $(\Delta\omega)$, along the ω axis, at fixed $\underline{k}_p$. The corresponding Q-factor is given by $\omega_o/\Delta\omega$, where ω_o is the central frequency of the resonance. A very high-Q resonant mode is of course comparatively delocalised in time, with a correspondingly small contour-line-density HWHM along the ω axis, whilst a very low-Q resonance will be much more temporally localised and therefore much more transitory, with a higher contour-line-density HWHM along the ω axis.

Similarly, the extent of spatial delocalisation is indicated by $1/\|\Delta\underline{k}_p\|$, where $\|\Delta\underline{k}_p\|$ is the HWHM of the contour line density along the $\underline{k}_p$ axis. It is perhaps instructive to define here a 'spatial Q,' Q_s, in analogy with the temporal Q-factor, to be such that $Q_s = k_o/\|\Delta\underline{k}_p\|$. This 'spatial Q' can be interpreted physically in terms of the number of transverse (i.e. in-plane) spatial periods beyond which the resonance is effectively extinguished. With this definition, the angular half-width of the emergence or acceptance cone, of light emitted from the resonant mode or coupled to it, respectively, is given by $\arcsin(1/Q_s)$. Note that a resonant mode that is tightly confined to a small

patch of a TFPC film, will of course be highly localised in space and therefore light emitted from it would diffract into a wide beam containing a wide range of in-plane wavevectors, giving a large contour-line-density HWHM along the $\underline{k}_p$ axis. A high-Q resonant mode that is distributed over the entire film (such as any of the resonances featured in Chapter 3, 4, and 5) will be practically delocalised in (x, y) space (yet still localised along the z-axis), so its contour-line-density HWHM along the $\underline{k}_p$ axis will be very small.

Whilst our intra-passband TFPCs do not have bandgaps, they may nevertheless have resonance gaps, which are apparent only on resonance diagrams. In the field of intra-passband photonic crystal devices, resonance gaps take the place of band gaps. Analogously, the introduction of defects into intra-passband TFPCs produces resonant states within resonance gaps, just as introducing defects into intra-bandgap TFPCs produces resonant states within band gaps. Within a resonance gap, propagation 'vertically' through the film is still possible (i.e from above the film to below it), but nominally 'horizontal' propagation inside the film is very lossy because of the absence of resonant modes.

6.3 The application of 'resonance contour maps' to MLP-TFPC simulation

If we could design MLP-TFPCs so that efficient input/output coupling is achieved via locally quasi-guided modes whilst the main function of the device is performed by truly-guided local modes, then we could make use of the advantages of both types of resonant mode. In other words, by controlling the out-of-plane loss as a function of in-plane position, the main obstacles to the production of low-loss easily-interfaced integrated optical components could be overcome. Since any useful MLP-TFPC may be assumed to have input/output coupling pads, the global resonant modes can, in practice, always be assumed to be quasi-guided, even though the local modes may be either quasi-guided or guided. Therefore, the functionality of a practical MLP-TFPC device must entirely rely on its quasi-guided global modes. This implies that if a resonance contour map of a particular MLP-TFPC (modelled by tiling it to form a super-lattice) is computed, then field plots made at selected points along the high-Q global resonance loci will show the device in operation. Then, having found what the device does, one can iteratively refine its internal structural parameters by repeatedly altering them, generating a new series of field plots along the resonance loci each time, until it performs the desired optical function satisfactorily.

The out-of-plane loss will be defined to be the contribution to the z-component of the time-averaged power flux density vector due to waves propagating away from the patterned film (towards $+\infty$ or $-\infty$), expressed as a function of in-plane position:

$$J_z^{loss}(x,y) = (1/2)Re[E_x^*(x,y,z_o)H_y(x,y,z_o) - E_y^*(x,y,z_o)H_x(x,y,z_o)], \qquad (6.1)$$

where z_o is a fixed z-coordinate within either of the unpatterned media. The out-of-plane loss of a quasi-guided global mode, existing at a particular point in $(\omega, \underline{k}_p)$ space, can be computed directly from its field distributions above the upper interface and below the lower interface. In the required summation over all of the emergent rays, one must include only the rays that freely propagate away from the film. Note that the transmittance (T) and reflectance (R) are normalised time-averaged integrals over a unit-cell of the super-lattice rather than being position-dependent power flux densities, so the positional dependence of the out-of-plane loss is lost in plotting a 'resonance contour map', thus necessitating the reconstruction of the position-dependent field components once the resonances have been located.

This method will now be illustrated by a simple example. Since our present code was written to run on a relatively low-specification workstation that is not realistically capable of handling large 2D superlattices, we are, at the moment, restricted to cases that are less computationally intensive, but hopefully this example will be sufficient to convey the basic steps involved.

6.4 Illustration of the method

Figure 6.1 is a resonance contour map of a particular TFPC having two orthogonal axes of continuous translational invariance. The host crystal, of pitch Λ, consists of a regular array of deeply-etched parallel-sided grooves, but every seventh groove has been filled-in with solid material, creating a periodic array of defects tiled on a superlattice of pitch 7Λ. The in-plane directions of the input plane-waves, incident from the substrate, are aligned so that they are parallel to the grating axis in order to force the TE and TM polarisation states to decouple from each other, thus decreasing the required computation time because the scattering matrices then have only a quarter of the number of elements that they would otherwise have. The parameters for this graph are as follows: film index n_f=3.46, host lattice pitch Λ=400nm, groove width W=120nm, film thickness L=100nm, substrate index n_s=1.6, cover index n_c=1.0, polarisation state=TE. The interpretation of such graphs was discussed in the previous section. The way in which we have defined the normalised frequency Ω (see caption to Figure 6.1) ensures that its value is independent of the host-lattice and super-lattice pitch,

making comparisons between different resonance isocontour maps easier. Note the existence of a defect state located near the middle of a 'resonance gap', above which there are bands of 'conduction states', and below which are 'valence states'.

The 'resonance gap' in this figure, which is centred on a vacuum wavelength of 875nm, is not the same as a 'band gap', because even though there are no high-Q resonances in this gap, low-Q eigenmodes are nevertheless present. The repetition period (in terms of in-plane wavevector k_p rather than $\sin(\theta)$) of the conduction and valence band resonance loci (named, of course, by analogy with electronic bandstructure) corresponds to the Brillouin zone boundary spacing of the superlattice. Increasing the superlattice period, thus decreasing the extent of mutual inter-coupling between the tiled defects, reduces this repetition period and also results in asymptotic convergence of the conduction and valence bands towards the form depicted in Figure 6.3(b) (which is for the host lattice, without defects) whilst leaving the defect-state feature essentially unchanged. The HWHM of the defect-state feature in Figure 6.1 is approximately 0.15 in terms of $\sin(\theta)$, which corresponds to an angular FWHM of 17.3^o in the substrate, or 27.8^o in the cover (in which the refractive index is lower by a factor of 1.6). The angular widths of the beams emitted by the defects into the substrate and cover are therefore 17.3^o and 27.8^o respectively. From this resonance contour map, we can also directly deduce the cavity Q-factor of the defect state as follows: the HWHM of the defect-feature along the normalised frequency (Ω) axis is 0.175 and it is centred on a normalised frequency of 7.3, so its corresponding Q-factor is $\Omega_o/\Delta\Omega = 7.3/0.175 \approx 42$. The defect-feature is wide along the $\sin(\theta)$) axis yet relatively narrow along the Ω axis. This indicates that the defect-resonance is localised in space but comparatively delocalised in time (i.e. it has a relatively long lifetime), which is characteristic of a defect mode.

To get a feel for the underlying structure of this sort of resonance contour map, we can compare it with a resonance-locus diagram in $(\Omega, \sin(\theta))$ space. Figure 6.2 is such a diagram, and it was plotted by locating the eigenvalues of the matrix operator $I - PS_2^{-+}PS_1^{+-}$ (see Chapter 5) having the smallest imaginary parts: wherever the eigenvalue of smallest imaginary part was within a certain tolerance of zero, a small dot was printed, thus building-up the loci of the resonances point-by-point on a fixed sampling grid in the $(\Omega, \sin(\theta))$ plane. This graph therefore constitues the basic skeleton of the resonance contour map in Figure 6.1, separated from the additional information concerning spatial and temporal localisation and external coupling efficiency, that it provides. Examining the field profiles (see Figures 6.2(c,d,e)) of various resonant states along these loci confirms our interpretation of the resonance-map features: (c) is a low-modal-index host-lattice mode, (d) is a defect mode, and (e) is a high-modal-index host-lattice mode. The relative modal indices of these modes can be guessed by considering the overlap integral of the fields with the solid material.

Resonance contour maps for two-dimensionally patterned TFPCs take a long time to produce, especially for big supercells, due to the larger number of basis vectors that must be retained in the Fourier expansions and also because of the very fine sampling grid in (ω, k_p) that is required to resolve the much higher-Q resonances that they support. Examples of these will not be given because Figure 6.1 is quite sufficient for our present purpose.

6.5 Verification of our 'infinite patterned area' assumption

At this point, it will be instructive to include a verification of the assumption made throughout this thesis that the patterned area of a TFPC can be such that it is effectively infinite. This verification was made by comparing resonance diagrams for many different monoperiodic TFPCs with results generated by a Finite-Difference Time-Domain (FDTD) method [82]. This work [4] was funded by COST 268 and was done by R. Stoffer and I at the University of Twente in The Netherlands (see Acknowledgements). To distinguish our method from theirs, we will use the term 'Vector-Field Fourier-Decomposition' (VFFD). A 40-period truncated grating was shown to be, for all practical purposes, sufficiently similar in behaviour to an infinite grating for it to give close correspondence with our VFFD method. Figure 6.3(a) shows the normalised fractional out-of-plane diffraction loss and the 'horizontal reflectance' (for light-injection from the side rather than from above) of a 40-period 1D-patterned TFPC incorporated within an unpatterned slab waveguide, against vacuum wavelength. This was calculated by FDTD. Side-by-side with this graph is a resonance contour map (see Figure 6.3(b)), calculated by VFFD, using the same vertical axes as in (a). It can be seen that high horizontal reflectance and low diffraction loss is obtained within the cross-hatched resonance gaps. In the pass-bands, the horizontal reflectance is low because there are resonant waveguide modes that can absorb the energy of the input beam, and the high diffraction loss within the pass-bands are due to the large scattering losses incurred by the abrupt impedance mismatch between resonant grating modes and unpatterned waveguide modes at the boundaries of the truncated grating. These results suggest that we do not need enormous patterned areas in order to obtain the sorts of resonances that were discussed in Chapters 3, 4, and 5. It was not possible to use the FDTD method to look at 2D-patterned TFPCs because the computation time has a very high-order power-law dependence on the number of grating axes (i.e. $3-m$ where m is the number of axes of continuous translational invariance).

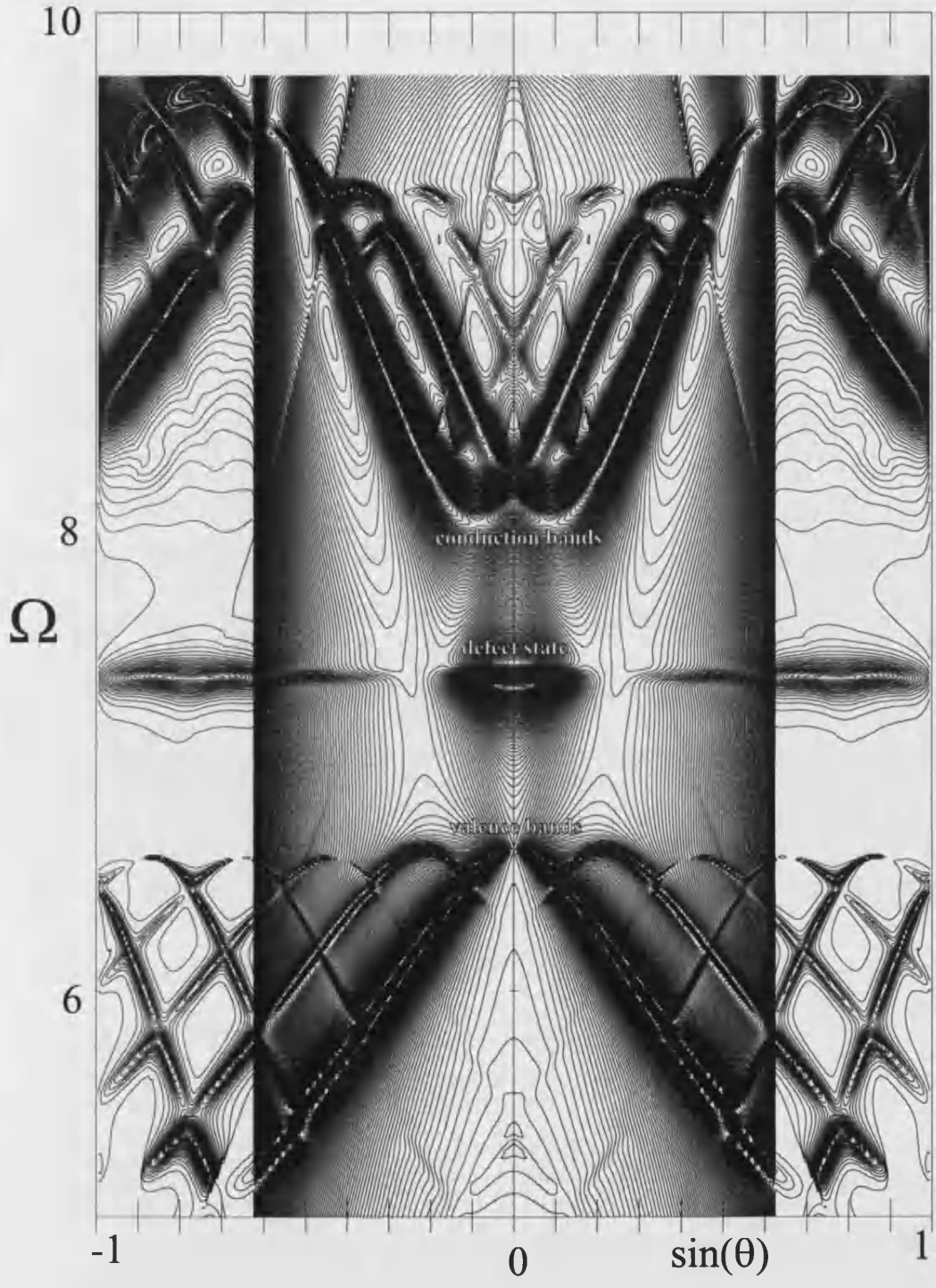

Figure 6.1: Resonance isocontour map of transmittance for a one-dimensionally periodic TFPC containing a regular array of defects tiled on a superlattice of pitch 7Λ, where Λ is the host-lattice pitch. The defects consist of missing air-channels. The horizontal axis is $\sin(\theta)$, where θ is the angle of incidence of plane waves from the substrate medium. This makes the graph rectangular rather than triangular. The vertical axis is a 'standardised' normalised frequency $\Omega = 2\pi\Lambda^{common}/\lambda_o$ where Λ^{common} is fixed at a value of $1000nm$, irrespective of the microstructure. Note the presence of a defect-state in the middle of the 'resonance gap'.

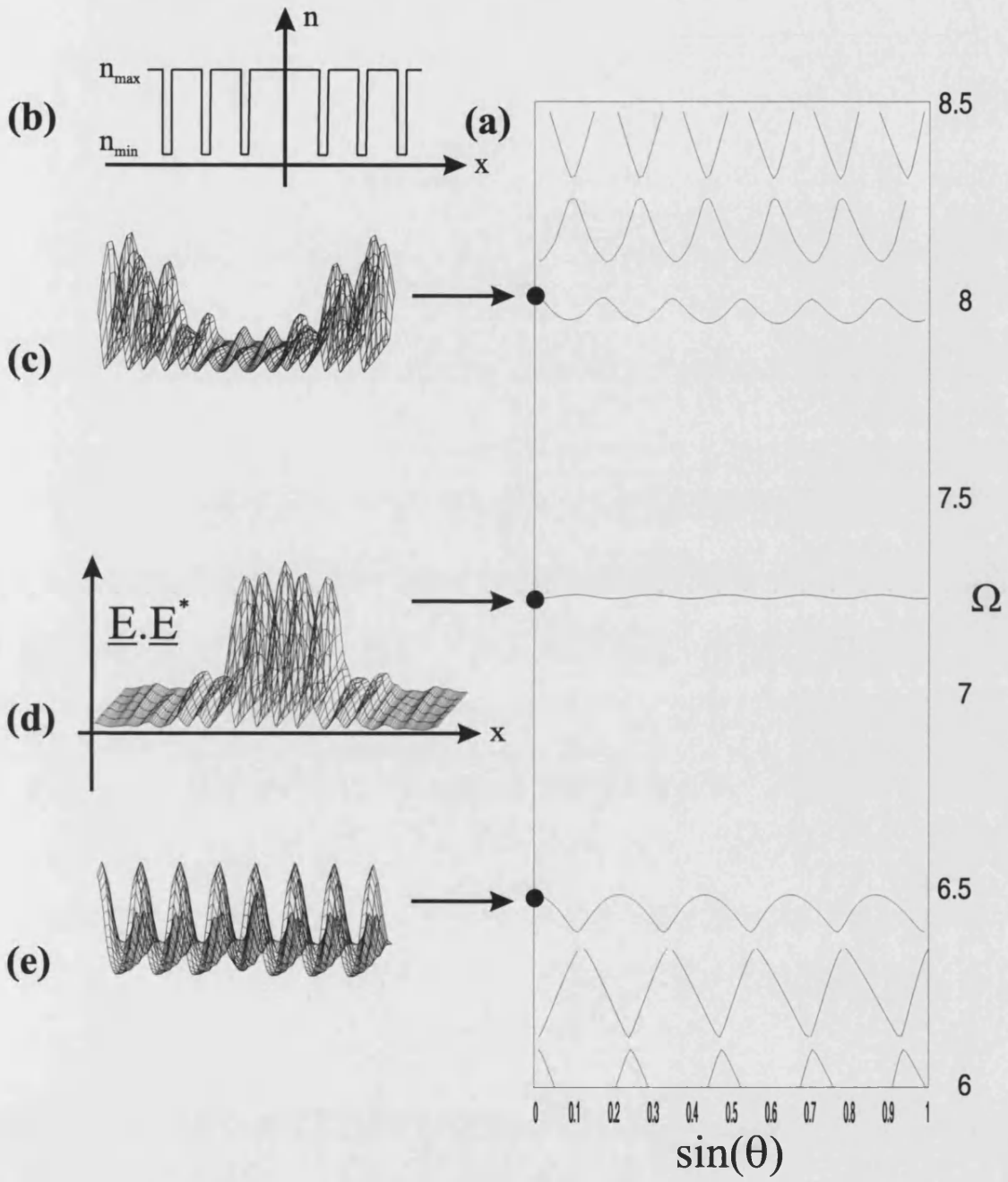

Figure 6.2: (a)The loci of the resonances appearing in Figure 6.1, plotted by evaluating $min(Im(Eigenvalue(I-PS_2^{-+}PS_1^{+-})))$. This shows the underlying structure of Figure 6.1, whilst Figure 6.1 gives information on the external coupling efficiency, Q-factor, and angular beam-width of these resonant states. (b) The refractive index profile within a single supercell of the tiled-defect structure. Field profiles (on the same axes as (b)) at various points along the resonance loci, plotted at $\sin(\theta)) = 0$, are shown in (c), (d), and (e).

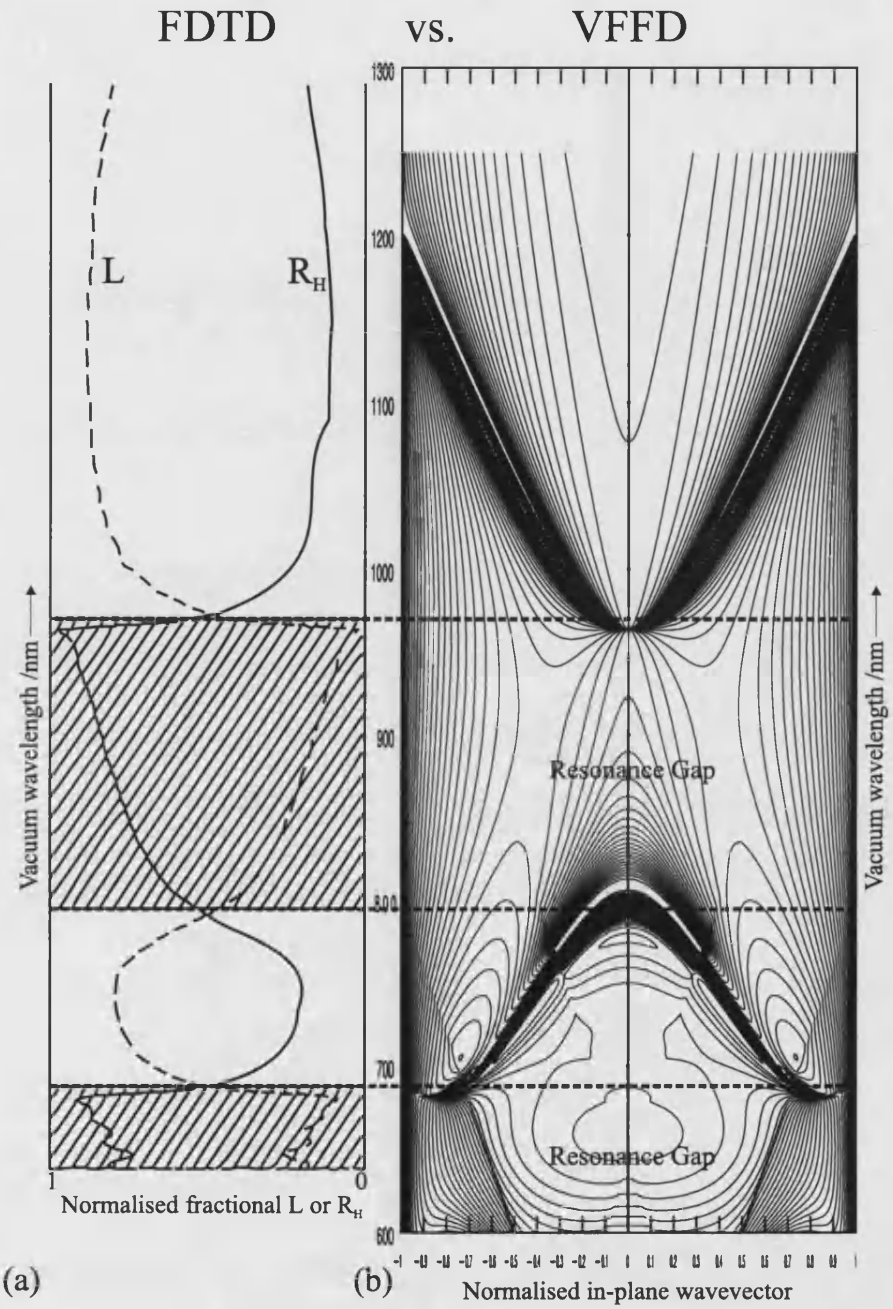

Figure 6.3: Comparison of FDTD (for finite patterned area) and VFFD (for infinite patterned area) results for structures having identical micro-patterning parameters. The host-lattice parameters are the same as for Figures 6.1 and 6.2, but in this case there are no defects. (a)FDTD results showing the diffraction loss (L) and the horizontal reflectance (R_H) against vacuum wavelength/nm, for a 40-period 1D-patterned TFPC. (b) VFFD results, expressed in the form of a 'resonance contour map' for an infinite version of the same TFPC (for light incident from the cover medium). The resonance gaps appearing in (b) are cross-hatched in (a).

6.6 Compact devices based on 2D MLP-TFPC microstructures

Perhaps the simplest application of an MLP-TFPC, which could be analysed in future by our 'resonance contour map' method is as a WDM de-multiplexer, as stated in Chapter 1. This could of course be operated in reverse as a multiplexer. Such a device would use quasi-guided modes for input-coupling and output-coupling, and guided modes for the signal processing (which is wavelength-dependent beam-steering in this case). Figure 6.4 is a schematic diagram (not to scale) of a plausible MLP-TFPC de-multiplexer, showing how the input and output fibres could be arranged to separate the input beam into three wavelength channels. It should be noted that a de-multiplexer based only on a single globally periodic TFPC, which would use the same quasi-guided modes for input/output coupling and signal processing, would perhaps be inconvenient to make, because the in-plane and out-of-plane angles of the fibre axes would have to be separately adjusted, to a fairly tight tolerance, in order to excite the quasi-guided modes and to collect the emergent light. In the case of the MLP-TFPC de-multiplexer, it would be possible to design the input/output coupling pads so that their quasi-guided mode loci are approximately circular and also practically independent of wavelength within the wavelength range spanned by the WDM channels, so that all of the output fibres could be set to the same out-of-plane angles with respect to the surface-normal. In the intervening region between the coupling pads, highly dispersive guided modes could then be employed for spatially separating the various channels. To avoid large out-of-plane scattering losses at the boundaries between the coupling pads and the 'processing' area, gently parameter-graded transition regions must be interposed.

6.7 Conclusions

In this chapter, we have presented a method by which complicated MLP-TFPC microstructures may be modelled. This method is based on the use of 'resonance contour maps', which provide a convenient way of representing the temporal and spatial dispersion functions of quasi-guided global eigenmodes together with information on their temporal localisation, spatial localisation, and external coupling efficiency. The relation between the features appearing on resonance contour maps and the field-microstructure of the eigenmodes to which they correspond was illustrated by applying the 'resonance contour map' method to a 1D-patterned TFPC containing a periodic array of weakly-coupled defects.

By comparing resonance contour maps with FDTD calculation results we have, to

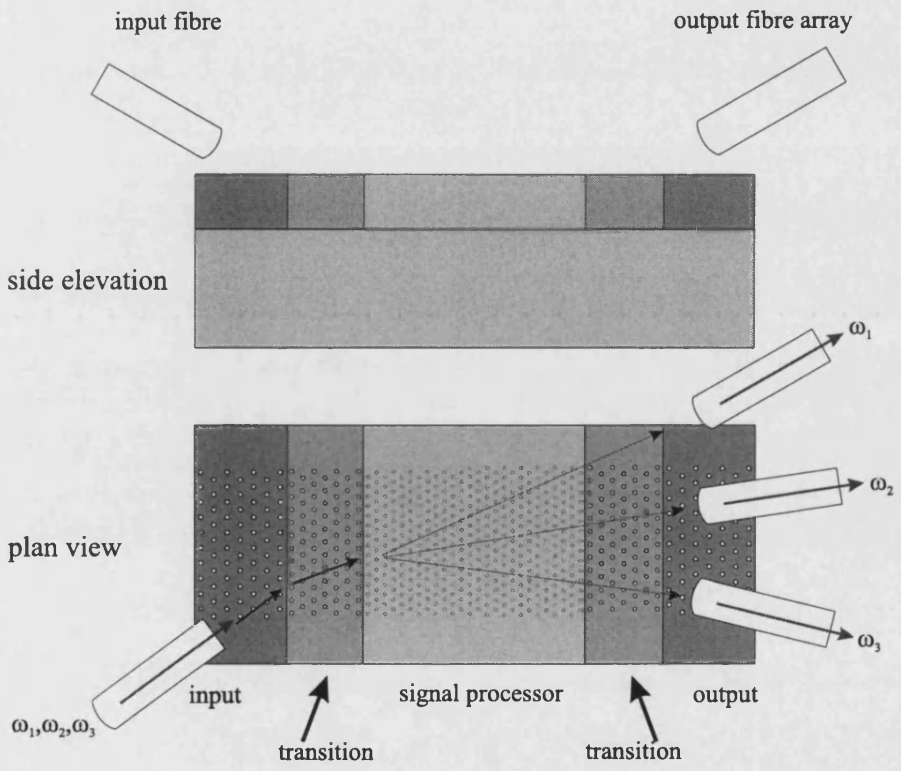

Figure 6.4: Schematic diagram of an MLP-TFPC de-multiplexer that uses quasi-guided modes for input/output coupling and guided modes for channelling incoming light into three separate output fibres according to wavelength.

some extent, verified that a TFPC of finite patterned area can nevertheless support similar resonant eigenmodes to those of a TFPC possessing an infinite patterned area. This would imply, if it is indeed true, that the assumptions that we have made so-far in our modelling are good. An example of the kind of structure to which our 'resonance contour map' method may be applied was then described: a miniature WDM demultiplexer, which would be a very useful TFPC-based integrable optical component. Such devices could, in principle, be modelled by 3D-FDTD computations, but the method that we suggest is much more elegant and potentially more efficient than such a 'brute force' approach, enabling the development of an intuitive understanding of the physics involved instead of degenerating into mindless 'number crunching'.

Chapter 7

Summary and Future Work

7.1 Summary

In conclusion, we have justified our statement in the introduction to Chapter 1 that one does not necessarily need to work within a bandgap in order for a photonic crystal to perform useful functions: none of the structures modelled in this thesis have bandgaps at their operational frequencies (although of course there will be bandgaps at other frequencies), yet many interesting phenomena were observed during simulation. Indeed, Bloch wave optics (i.e. the physics of propagating optical Bloch waves) in thin-film photonic crystals clearly has so many potential applications that could revolutionise everyday technology that it seems rather a shame to stifle the Bloch modes by the creation of bandgaps.

The various types of resonant eigenmodes that a TFPC can support were explored by a series of numerical simulations and their unusual and often unexpected properties were explained in terms of the basic Bloch modes of which they are composed. We then showed how entire fully-functional TFPC-based optical integrated circuits (such as WDM systems) could be designed to exploit the highly dispersive and extensively controllable propagation characteristics and tailorable out-of-plane leakage of these resonant eigenmodes. No-one has so-far been able to design these properly. Such TFPC optical circuits could be easily made merely by etching a carefully designed locally periodic lattice of holes, in a single fabrication step, into a pre-prepared thin dielectric film. These devices would also be easy to interface to optical fibres positioned above their input and output ports, which may be of relatively large surface area, thus improving the coupling efficiency. The high attainable Q-factors and optical confinement factors of quasi-guided TFPC modes, together with the small required film thickness, imply

that a TFPC would be a viable alternative to the bulky distributed Bragg reflectors (DBRs) currently used in semiconductor vertical-cavity surface-emitting lasers, as argued in Chapter 4. TFPC-VCSELs might also give higher maximum power-outputs without cooling than conventional DBR-VCSELs. Non-linear applications are also possible, because the combination of high cavity Q-factor and low in-plane group-velocity that one can obtain in a TFPC would greatly enhance nonlinear interactions, allowing the possibility of achieving frequency up/down conversion and broad-band quasi-continuous spectrum generation in TFPC microstructures. Furthermore, in Merely Locally Periodic TFPCs, photonic force-fields [49] of arbitrary geometries can be engineered, coercing light to follow any desired closed or open trajectory. For example, one could constrain the local Bloch-wave rays to move in a circle or a figure-of-eight. This is surely the ultimate in light-control.

7.2 Future Work

Further work could proceed in many different directions, both towards practical applications and along loftier conceptual branches that naturally spring from the main trunk of work presented in the first six chapters.

7.2.1 Fabrication and Characterisation

All of the work recounted in this thesis is based entirely on modelling, so it would be helpful to have experimental feedback to guide future work. Already, plans are in place to fabricate TFPCs in $Al_xGa_{1-x}As$ wafers, and the characterisation of fabricated TFPCs could employ Scanning Near-Field Optical Microscopy (SNOM) [83] to examine guided and quasi-guided field microstructures. Both amplitude [84] and phase [3] information can be obtained in SNOM, enabling exhaustive comparison between modelling results and experimental data. This would enable our modelling methods to be further refined and extended, and it may reveal interesting effects that we might have inadvertently overlooked.

7.2.2 Modelling of MLP-TFPC optical circuits by the 'resonance map' method

As we said in the introduction to Chapter 6, this is now the subject of an EPSRC-funded project entitled '3-D Control of Light in Fully-Functional Thin-Film Pho-

tonic Crystal Devices and Circuits'. The 'resonance map' method could enable complete fibre-terminated devices to be designed that are limited only by the imagination, and the most obvious component that should be modelled is the WDM multiplexer/demultiplexer described in Chapter 6, because this could make an immediate impact in the field of telecommunications. Modelling based on Hamiltonian optics [49] could supplement our understanding of local Bloch-wave propagation in these microstructures, and we could obtain the necessary Hamiltonian functions from local guided-mode dispersion surfaces $\omega_j(k_p)$ calculated by the 'resonant tunnelling method' proposed and illustrated in Chapter 5.

7.2.3 Charge-Carrier Transport Modelling in TFPC-VCSELs

To be certain about the feasibility of TFPC-based VCSELs, it is necessary to rigorously analyse their carrier transport properties, in conjunction with a more intensive investigation of optical confinement than that contained in Chapter 4.

7.2.4 Modelling of nonlinear interactions in TFPCs

All of our modelling has, thus far, been entirely concentrated on purely 'linear' effects in lossless media (i.e. assuming a real-valued field-intensity-independent refractive index). Of course, even in $Al_xGa_{1-x}As$, nonlinear effects would become significant at the high field intensities that can build-up inside a high-Q TFPC resonator. Our guided and quasi-guided resonances would, however, still be first-order approximations to the actual eigenmodes in the presence of nonlinearities and losses. Nonlinear effects in TFPCs are also within the scope of the above-mentioned EPSRC project. Some of the nonlinear devices that could result from work on this topic are very compact TFPC-based all-optical switches, parametric wavelength-convertors, and Semiconductor Saturable Absorber Mirrors (SESAMs) [85] for producing short laser pulses.

References

[1] J. M. Pottage, E. Silvestre, and P. St. J. Russell. Vertical-cavity surface-emitting resonances in photonic crystal films. *J. Opt. Soc. Am. A*, 18:442–447, 2001.

[2] E. Silvestre, J. M. Pottage, P. St. J. Russell, and P. J. Roberts. Design of thin-film photonic crystal waveguides. *Appl. Phys. Lett.*, 77:942–944, 2000.

[3] P. L. Phillips, J. C. Knight, J. M. Pottage, G. Kakarantzas, and P. St. J. Russell. Direct measurement of optical phase in the near field. *Appl. Phys. Lett.*, 76:541, 2000.

[4] J. M. Pottage, R. M. de Ridder, R. Stoffer, and H. J. W. M. Hoekstra. Simulation of thin-film photonic microstructures. In *Wavelength Scale Photonic Components for Telecommunications: COST 268 Meeting and International Workshop on Novel Gain Materials.* Wuerzburg, Germany, 2001.

[5] J. M. Pottage, E. Silvestre, and P. St. J. Russell. In *Proceedings of QELS 2000 San Francisco CA: OSA Technical Digest Series*, pages 121–122. Optical Society of America, Washington DC, 2000.

[6] E. Silvestre, J. M. Pottage, and P. St. J. Russell. In *Proceedings of QELS 2000 San Francisco CA: OSA Technical Digest Series*, pages 123–124. Optical Society of America, Washington DC, 2000.

[7] J. M. Pottage, E. Silvestre, P. St. J. Russell, and P. L. Phillips. In *Proceedings of* 14^{th} *UK National Quantum Electronics and Photonics Conference, Manchester: Technical Digest*, pages 207–208. Institute of Physics, London, 1999.

[8] P. St. J. Russell, J. M. Pottage, J. Broeng, D. S. Mogilevtsev, and P. L. Phillips. In *Proceedings of CLEO/QELS 1999 Baltimore MD: OSA Technical Digest Series*, pages 293–294. Optical Society of America, Washington DC, 1999.

[9] J. D. Joannopoulos, R. D. Meade, and J. N. Winn. *Photonic Crystals: Molding the flow of light.* Princeton University Press, Princeton NJ, 1995.

[10] P.St.J. Russell and T.A. Birks. Bloch wave optics in photonic crystals: Physics and applications. In C.M. Soukoulis, editor, *Photonic Band Gap Materials*, pages 71–91. Kluwer, The Netherlands, 1996.

[11] P.St.J. Russell. Interference of integrate Floquet-Bloch waves. *Phys. Rev. A*, 33:3232–3242, 1986.

[12] P.J. Herring. Reflective systems in aquatic animals. *Comp. Biochem. Physiol.*, 109A:513–546, 1994.

[13] C. Lawrence, P. Vukusic, and R. Sambles. Grazing-incidence iridescence from a butterfly wing. *Appl. Opt.*, 41:437–441, 2002.

[14] H. Tada, S.E. Mann, I. Miaoulis, and P.Y. Wong. Effects of butterfly scale microstructure on the iridescent color observed at different angles. *Appl. Opt.*, 37:1579–1584, 1998.

[15] R.C. Mc Phedran, N.A. Nicorovici, D.R. McKenzie, L.C. Botten, A.R. Parker, and G.W. Rouse. The Sea Mouse and the Photonic Crystal. *Aust. J. Chem.*, 54:241–244, 2001.

[16] P.St.J. Russell. Photonic band-gaps. *Physics World*, 5:37–42, 1992.

[17] J. B. Pendry. Photonic band structures. *J. Mod. Opt.*, 41:209–229, 1994.

[18] D.H. Choi and W.J.R. Hoefer. The finite-difference-time-domain method and its application to eigenvalue problems. *IEEE Trans. Microwave Theory and Techniques*, 34:1464, 1986.

[19] M.D. Feit and J.A. Fleck. Computation of mode properties in optical fiber waveguides by a propagating beam method. *Appl. Opt.*, 19:1154–1164, 1980.

[20] P.St.J. Russell, T.A. Birks, and F.D. Lloyd-Lucas. Photonic Bloch waves and photonic band gaps. In E. Burstein and C. Weisbuch, editors, *Confined Electrons and Photons*, page 585. Plenum, New York, 1995.

[21] E. Yablonovitch. Photonic band-gap crystals. *J. Phys.: Condens. Matter*, 5:2443–2460, 1993.

[22] T. A. Birks, J. C. Knight, B. J. Mangan, and P. St. J. Russell. Photonic crystal fibres: An endless variety. *IEICE Trans. Electron.*, E84-C:585–592, 2001.

[23] http://www.pbglink.com/bibliography.html.

[24] T. F. Krauss, R. M. De La Rue, and S. Brand. Two-dimensional photonic-bandgap structures operating at near-infrared wavelengths. *Nature*, 383:699–702, 1996.

[25] Y. Sugimoto, N. Ideka, N. Carlsson, and K. Asakawa. Fabrication and characterisation of different types of two-dimensional algaas photonic crystal slabs. *J. Appl. Phys.*, 91:922–929, 2002.

[26] N. Kawai, K. Inoue, N. Carlsson, N. Ikeda, Y. Sugimoto, K. Asakawa, and T. Takemori. Confined band gap in an air-bridge type of two-dimensional algaas photonic crystal. *Phys. Rev. Lett*, 86:2289–2292, 2001.

[27] E. Chow, S.Y. Lin, P.R. Villeneuve, J.D. Joannopoulos, J.R. Wendt, G.A. Vawter, W. Zubrzycki, H. Hou, and A. Alleman. Three-dimensional control of light in a two-dimensional photonic crystal slab. *Nature*, 407:983–986, 2000.

[28] K. Inoue, N. Kawai, Y. Sugimoto, N. Carlsson, N. Ikeda, and K. Asakawa. Observation of small group velocity in two-dimensional algaas-based photonic crystal slabs. *Phys. Rev. B, Rapid Communications.*, 65:121308, 2002.

[29] V.N. Astratov, R.M. Stevenson, I.S. Culshaw, D.M. Whittaker, M.S. Skolnick, T.F. Krauss, and R.M. De La Rue. Heavy photon dispersions in photonic crystal waveguides. *Appl. Phys. Lett.*, 77:178–180, 2000.

[30] H. Kosaka, T. Kawashima, A. Tomita, M. Notomi, T. Tamamura, T. Sato, and S. Kawakami. *IEEE J. Lightwave Technol.*, 17:2032–2038, 1999.

[31] M. Notomi. Negative refraction in photonic crystals. *Optical and Quant. Electron.*, 34:133–143, 2002.

[32] W. Park and C.J. Summers. Extraordinary refraction and dispersion in two-dimensional photonic-crystal slabs. *Opt. Lett.*, 27:1397–1399, 2002.

[33] B. Gralak, S. Enoch, and G. Tayeb. Anomalous refractive properties of photonic crystals. *J. Opt. Soc. Am. A*, 17:1012–1020, 2000.

[34] O. Painter, J. Vuckovic, and A. Scherer. Defect modes of a two-dimensional photonic crystal in an optically thin dielectric slab. *J. Opt. Soc. Am. B*, 16:275–284, 1999.

[35] J.-K. Hwang, S.-B. Hyun, H.-Y. Ryu, and Y.-H. Lee. Reosonant modes of two-dimensional photonic bandgap cavities determined by the finite-element method and by use of the anisotropic perfectly matched layer boundar condition. *J. Opt. Soc. Am. A*, 15:2316–2324, 1998.

[36] E. Miyai and K. Sakoda. Quality factor for localized defect modes in a photonic crystal slab upon a low-index substrate. *Opt. Lett.*, 26:740–742, 2001.

[37] J.-K. Hwang, H.-Y. Ryu, and Y.-H. Lee. Spontaneous emission rate of an electric dipole in a general microcavity. *Phys. Rev. B*, 60:4688–4695, 1999.

[38] R.K. Lee, O. Painter, B. Kitzke, A. Scherer, and A. Yariv. Emission properties of a defect cavity in a two-dimensional photonic bandgap crystal slab. *J. Opt. Soc. Am. B*, 17:629–633, 2000.

[39] M. Loncar, J. Vuckovic, and A. Scherer. Methods for controlling positions of guided modes in photonic-crystal waveguides. *J. Opt. Soc. Am. B*, 18:1362–1368, 2001.

[40] H. Benisty, C. Weisbuch, D. Labilloy, M. Rattier, C.J.M. Smith, T.F. Krauss, R.M. De La Rue, R. Houdre, U. Oesterle, C. Jouanin, and D. Cassagne. Optical and confinement properties of two-dimensional photonic crystals. *IEEE J. Lightwave Technol.*, 17:2063–2076, 1999.

[41] D.W. Prather, J. Murakowski, S. Shi, S. Venkataraman, A. Sharkawy, C. Chen, and D. Pustai. High-efficiency coupling structure for a single-line-defect photonic-crystal waveguide. *Opt. Lett.*, 27:1601–1603, 2002.

[42] S. Boscolo, M. Midrio, and T.F. Krauss. Y junctions in photonic crystal channel waveguides: high transmission and impedance matching. *Opt. Lett.*, 27:1001–1003, 2002.

[43] E. Centeno and D. Felbacq. Cross waveguides in biperiodic two-dimensional photonic crystals. *J. Opt. A: Pure Appl. Opt.*, 3:S154–S160, 2001.

[44] P.St.J. Russell, D.M. Atkin, T.A. Birks, and P.J. Roberts. Bound modes of two-dimensional photonic crystal waveguides. In J.G. Rarity and C. Weisbuch, editors, *Quantum optics in wavelength scale structures.* Kluwer, The Netherlands, 1996.

[45] D.M. Atkin, P.St.J. Russell, T.A. Birks, and P.J. Roberts. Photonic band structure of guided Bloch modes in high index films fully etched through with periodic microstructure. *J. Mod. Opt.*, 43:1035–1053, 1996.

[46] A.R. Cowan and J.F. Young. Mode matching for second-harmonic generation in photonic crystal waveguides. *Phys. Rev. B*, 65:085106, 2002.

[47] A.M. Malvezzi, F. Cattaneo, G. Vecchi, M. Falasconi, G. Guizetti, L.C. Andreani, F. Romanato, L. Businaro, E. Di Fabrizio, A. Passaseo, and M. De Vittorio. Second-harmonic generation in reflection and diffraction by a gaas photonic-crystal waveguide. *J. Opt. Soc. Am. B*, 19:2122–2128, 2002.

[48] S. Scholz, O. Hess, and R. Ruhle. Dynamic cross-waveguide optical switching with nonlinear photonic band-gap structure. *Optics Express*, 3:28–34, 1998.

[49] P. St. J. Russell and T. A. Birks. *IEEE J. Lightwave Technol.*, 17:1982, 1999.

[50] J.A. Arnaud. *Beam and fiber optics.* Academic Press, New York, 1976.

[51] C.J. Chang-Hasnain. Vertical-cavity surface-emitting lasers. In G.P Agrawal, editor, *Semiconductor Lasers Past, Present, and Future*, pages 145–180. AIP Press, New York, 1995.

[52] A. Ferrando, E. Silvestre, J. J. Miret, and P. Andres. Vector description of higher-order modes in photonic crystal fibres. *J. Opt. Soc. Am. A*, 17:1333–1339, 2000.

[53] D. Mogilevtsev, T. A. Birks, and P. St. J. Russell. Group-velocity dispersion in photonic crystal fibres. *Opt. Lett.*, 23:1662–1664, 1998.

[54] H. Kogelnik. Theory of optical waveguides. In T. Tamir, editor, *Guided-Wave Optoelectronics*, pages 7–87. Springer-Verlag, USA, 1988.

[55] C. Kittel. *Introduction to Solid-State Physics.* John Wiley, New York, 1996.

[56] B. H. Bransden and C. J. Joachain. *Introduction to Quantum Mechanics.* Longman, UK, 1989.

[57] M. D. B. Charlton, S. W. Roberts, and G. J. Parker. Guided mode analysis and fabrication of a 2-dimensional visible photonic band structure confined within a planar semiconductor waveguide. *Mater. Sci. Engin.*, B49:155, 1997.

[58] P.St.J. Russell. Novel thick-grating beam-squeezing device in Ta_2O_5 corrugated planar waveguide. *Electr. Lett.*, 20:72–73, 1984.

[59] R. Zengerle. Light propagation in single and doubly periodic planar waveguides. *J. Mod. Opt.*, 34:1589–1617, 1987.

[60] O. Painter, R.K. Lee, A. Scherer, A. Yariv, J.D. O'Brien, P.D. Dapkus, and I. Kim. Two-dimensional photonic band-gap defect mode laser. *Science*, 284:1819–1821, 1999.

[61] H. Kosaka, T. Kawashima, A. Tomita, M. Notomi, T. Tamamura, T. Sato, and S. Kawakami. Photonic crystals for micro lightwave circuits using wavelength-dependent angular beam steering. *Appl. Phys. Lett.*, 74:1370–1372, 1999.

[62] V.N. Astratov, I.S. Culshaw, R.M. Stevenson, D.M. Whittaker, M.S. Skolnick, T.F. Krauss, and R.M. De La Rue. Resonant coupling of near-infrared radiation in photonic band structure waveguides. *IEEE J. Lightwave Technol.*, 17:2050–2057, 1999.

[63] E. Hecht and A. Zajac. *Optics.* Addison-Wesley, 1974.

[64] H. Soda, K. Iga, C. Kitahara, and Y. Suematsu. *Jpn. J. Appl. Phys*, 18:2329, 1979.

[65] M. Orenstein, A. Von Lehman, C. J. Chang-Hasnain, N. G. Stoffel, L. T. Florez, J. P. Harbison, J. Wullert, and A. Scherer. *Electr. Lett.*, 27:437, 1991.

[66] C. J. Chang-Hasnain, J. R. Wullert, J. P. Harbison, L. T. Florez, N. G. Stoffel, and M. W. Meada. *Appl. Phys. Lett.*, 58:31, 1991.

[67] Chapters 1-7. In C. H. Gooch, editor, *Gallium Arsenide Lasers.* Wiley Interscience, Bristol, 1969.

[68] C. J. Chang-Hasnain, J. P. Harbison, C.-E. Zah, M. W. Maeda, L. T. Florez, N. G. Stoffel, and T.-P. Lee. *Appl. Phys. Lett.*, 27:1368, 1991.

[69] J.L. Jewell, A. Scherer, S.L. McCall, Y.H. Lee, S. Walker, J.P. Harbison, and L.T. Florez. *Electr. Lett.*, 25:1123, 1989.

[70] C.J. Chang-Hasnain, Y.W. Wu, G.S. Li, G. Hasnain, K.D. Choquete, C. Caneau, and L.T. Florez. Low threshold buried heterostructure vertical cavity surface-emitting laser. *Appl. Phys. Lett.*, 63:1307–1309, 1993.

[71] J.J. Coleman. Quantum-well heterostructure lasers. In G.P Agrawal, editor, *Semiconductor Lasers Past, Present, and Future*, pages 1–27. AIP Press, New York, 1995.

[72] In G.A. Evans and J.M. Hammaer, editors, *Surface Emitting Semiconductor Lasers and Arrays*, pages 76–80. Academic Press Inc., Boston, 1993.

[73] P. M. Bell, J. B. Pendry, L. Martin Moreno, and A. J. Ward. A program for calculating photonic band structures and transmission coefficients of complex structures. *Computer Physics Communications*, 85:306–322, 1995.

[74] P. St. J. Russell, J. M. Pottage, J. Broeng, D. S. Mogilevtsev, and P. L. Phillips. In *Proceedings of CLEO/QELS 1999 Baltimore MD: OSA Technical Digest Series*, pages 293–294. Optical Society of America, Washington DC, 1999.

[75] A. Mekis, J. C. Chen, I. Kurland, S. Fan, P. R. Villeneuve, and J. D. Joannopoulos. *Phys. Rev. Lett*, 77:3787, 1996.

[76] S. Y. Lin, E. Chow, V. Hietala, P. R. Villeneuve, and J. D. Joannopoulos. *Science*, 282:274, 1998.

[77] E. Silvestre, P. St. J. Russell, T. A. Birks, and J. C. Knight. *J. Opt. Soc. Am. A*, 15:3067, 1998.

[78] J. M. Lupton, B. J. Matterson, I. D. W. Samuel M. J. Jory, and W. L. Barnes. Bragg scattering from periodically microstructured light emitting diodes. *Appl. Phys. Lett.*, 77:3340–3342, 2000.

[79] A.-L. Fehrembach, S. Enoch, and A. Sentenac. Highly directive light sources using two-dimensional photonic crystal slabs. *Appl. Phys. Lett.*, 79:4280–4282, 2001.

[80] P. K. Tien, S. R. Sanseverino, and R. J. Martin. *Phys. Lett*, 14:503, 1974.

[81] R. Ulrich and R. Torge. *Appl. Opt.*, 12:2901, 1973.

[82] R. Stoffer, H.J.W.M. Hoekstra, R. M. De Ridder, E. Van Groesen, and F.P.H. Van Beckum. *Optical and Quantum Electron.*, 32:947–961, 2000.

[83] D.W. Pohl, W. Denk, and M. Lanz. *Appl. Phys. Lett.*, 44:651, 1984.

[84] P.L. Phillips, J. C. Knight, B.J. Mangan, M.D.B. Charlton, and G.J. Parker. *J. Appl. Phys*, 85:6337, 1999.

[85] U. Keller et al. SESAMs for femtosecond to nanosecond pulse generation in solid state lasers. *IEEE J. Sel. Top. Quant. Elec.*, 2:435, 1996.